NEUTRON ELASTIC SCATTERING CROSS SECTION OF ^{12}C WITH CoGANC AT LANSCE

By

Nicholas Mendez

A DISSERTATION

Submitted to
Michigan State University
in partial fulfillment of the requirements
for the degree of

Physics—Doctor of Philosophy

2025

ABSTRACT

Nuclear data that are well-characterized and accurate are pertinent not only in nuclear science, where experimental efforts exist to measure known quantities to higher degrees of accuracy and measure unknown properties of nuclear systems, but also for applications that rely upon such data for performance metrics, material interrogation, and more. Unfortunately, a wide variety of impactful nuclear reaction data, even for stable nuclei such as carbon, is scarce. One property of carbon that is lacking data is the neutron elastic scattering cross section in the fast neutron regime (starting at $\approx$ 1 MeV) which is a dominant contributor to neutron transport in carbon-rich materials.

An experimental measurement of the elastic scattering cross section of ^{12}C was accomplished using the CoGNAC (Correlated Gamma-Neutron Array for sCattering) detector system at the WNR (Weapons Neutron Research) Facility at LANSCE (Los Alamos Neutron Science Center). The white (continuous) neutron source available at LANSCE allows for a range of incident neutron energies to be simultaneously measured for incident energies above 1 MeV. The presented measurement utilizes the ^{252}Cf PFNS (Prompt Fission Neutron Spectrum) standard to allow for a data-driven analysis, independent of simulation, to be accomplished.

The ^{12}C(n, el) integrated cross section, differential angular cross section, and emitted neutron angular distributions were measured along with detailed uncertainty quantification and covariances in the incident neutron energy range of $E_n^{inc} = 0.85$ – 7 MeV.

Dedicated to my family

ACKNOWLEDGMENTS

This work is supported by the National Science Foundation (NSF) grants PHY-2012040 and PHY-2310078 for The MoNA Collaboration at the Facility for Rare Isotope Beams (FRIB) at Michigan State University (MSU). Additionally, support was provided by the FRIB Graduate Fellowship. This work is also in support of the National Nuclear Security Administration (NNSA) and U. S. Department of Energy (DOE) Office of Experimental Science (NA-113).

TABLE OF CONTENTS

CHAPTER 1

INTRODUCTION & BACKGROUND

The nuclear landscape spans a myriad of nuclei with varying decays, shapes, masses, and nucleon configurations. These nuclei are a fundamental "building-block" of the universe and understanding the nature of nuclear properties can yield valuable information about one of the smallest forms of matter. How these differing nuclei interact with each other through nuclear reactions can help inform complicated processes such as stellar formation, nuclear medicine, and national security applications. Nuclear reactions are a fundamental component to nuclear science studies that allow for properties of the nucleus to be transformed and probed through the interaction between nucleons: neutrons and protons. In particular, how neutrons interact with nuclei and with what probability, is the main underlying theme that is explored in this dissertation work. The measurement of a cross section, the probability of a given reaction to occur, can inform the scientific community that rely upon such data.

1.1 Scattering Theory

In a typical reaction experiment, one measures particles over a given amount of time, known as the reaction rate. This quantity is proportional to the flux, Φ, defined as the rate of the incident particles, the target density n (the number of target particles in a given volume), and the probability σ_α that a desired reaction α occurred (the cross section) [1, 2, 3]. The reaction rate N_α is given by

$$N_\alpha = \Phi n \sigma_\alpha \,, \tag{1.1}$$

and solving for the cross section produces

$$\sigma_\alpha = \frac{N_\alpha}{\Phi n} \,. \tag{1.2}$$

Measuring the number of events at a given angle using a detector with a solid angle $\Delta\Omega$, the differential angular cross section for reaction α is defined to be

$$\frac{d\sigma_\alpha}{d\Omega} = \frac{N_\alpha}{\Phi n} \frac{1}{\Delta\Omega} \,. \tag{1.3}$$

Integrating Equation 1.3 over all scattering angles results in the the integrated cross section

$$\sigma_\alpha = \int \frac{d\sigma_\alpha}{d\Omega} d\Omega \,, \tag{1.4}$$

with the differential solid angle $d\Omega$ being expressed as $\sin(\theta) d\theta d\varphi$ where θ is the scattering angle made with respect to the incident particle axis and the outgoing scattered particle, ranging from 0 – 180°, and φ is the azimuthal angle ranging from 0 – 360°. This formalism provides the framework for which one is able to measure a reaction of interest. For the present work, the reaction of interest is the neutron elastic reaction (n, el), also referred to as neutron elastic scattering. Cross section quantities pertaining to elastic scattering will be denoted as σ_{el}.

1.1.1 Schrödinger Formalism

Following a combined motivation from Refs. [1, 3], the cross section from a quantum perspective can be motivated by representing neutron elastic scattering as the scattering of a plane wave. The generalized wavefunction, $\psi(r)$, must satisfy the Schrödinger equation

$$\left[-\frac{\hbar^2}{2m} \nabla_r^2 + V(r) \right] \psi(r) = E\psi(r) \,, \tag{1.5}$$

where m is the mass of the particle, the Laplacian operator in spherical coordinates is given by ∇_r, the potential experienced by the particle is given by $V(r)$, and E is the energy of the system. For the case of scattering, the two particles in the system are the projectile neutron (n), and the scattering target, C (for this work, the scattering target is carbon). This modifies the Schrödinger equation to

$$\left[-\frac{\hbar^2}{2m_n} \nabla_{r_n}^2 - \frac{\hbar^2}{2m_C} \nabla_{r_C}^2 + V(r_n - r_C) \right] \Psi(r_n, r_C) = E_{tot} \Psi(r_n, r_C) \tag{1.6}$$

$$\rightarrow \quad \left[-\frac{\hbar^2}{2m_{tot}} \nabla_s^2 - \frac{\hbar^2}{2\mu} \nabla_r^2 + V(r) \right] \Psi(s, r) = E_{tot} \Psi(s, r) \,, \tag{1.7}$$

with Equation 1.7 being the center-of-mass representation of Equation 1.6. The modified wavefunction now becomes $\Psi(s, r) = \phi(s)\psi(r)$ with $\phi(s)$ describing the motion of the center-of-mass system as it moves with location s and $\psi(r)$ describes the motion of the scattering

system within the center-of-mass frame with r being the distance between the projectile and scattering target $(r_n - r_C)$. The total mass is given by $m_{tot} = m_n + m_C$, $\mu = \frac{m_n m_C}{m_{tot}}$ is the reduced mass, $V(r)$ is the scattering potential between the projectile and scattering target, and E_{tot} is the total energy of the system.

Separating the modified wavefunction into the two separate variables allows for two independent solutions for $\phi(s)$ and $\psi(r)$ to be found resulting in Equation 1.7 to become

$$\text{Center-of-Mass (s)}: \; -\frac{\hbar^2}{2m_{tot}}\nabla_s^2\phi(s) = (E_{tot} - E_{sc})\phi(s) \tag{1.8}$$

$$\text{Scattering (r)}: \; \left[-\frac{\hbar^2}{2\mu}\nabla_r^2 + V(r)\right]\psi(r) = E_{sc}\psi(r)\,, \tag{1.9}$$

with $E_{sc} = \frac{1}{2}\mu\dot{r}^2$ representing the kinetic energy of the scattering system, $\dot{r} = \frac{p^2}{2\mu}$ is the first time-derivative of r and is equal to the velocity v, and $p = \mu v = \hbar k$ is the momentum of the scattering system. Equation 1.8 has $\phi(s)$ take the solution of a plane wave of the form $\phi(s) = De^{-ik_s s}$ with amplitude D and with k_s satisfying the condition $E_{tot} - E_{sc} = \frac{\hbar^2 k_s^2}{2m_{tot}}$. As can be seen from Equation 1.9, the "physics" of the scattering system can be reduced down to the wavefunction, $\psi(r)$, describing the interaction of the projectile with the scattering target, simplifying the complexity of the problem to the relative position of the two particles, r. The (kinetic) scattering energy can be rewritten as $E_{sc} = \frac{\hbar^2 k_{sc}^2}{2\mu}$ knowing that $v = \frac{p}{\mu} = \frac{\hbar k_{sc}}{\mu}$ which defines $k_{sc} = \frac{\sqrt{2\mu E_{sc}}}{\hbar}$.

The cross section, conceptually, is a ratio of the fluxes (final scattered flux to initial flux) and is given by $j = v|\psi|^2$. Far away from the scattering target and before a scattering event, the wavefunction initially will have the form of a plane wave

$$\psi_i(r) = Ae^{ik_i r}\,, \tag{1.10}$$

with some amplitude, A. The flux of the initial wavefunction, with velocity $v_i = \frac{\hbar}{\mu}k_i$, is then

$$j_i = v_i|A|^2 = \frac{\hbar}{\mu}k_i|A|^2\,. \tag{1.11}$$

For the scattered spherical wave, the final amplitude will differ depending on the angle observed at $(\theta,\, \phi)$ and will decrease asymptotically with increasing r but will result in a

constant flux when integrated across all solid angles. As such, the scattered wave will take the form

$$\psi_f(r) = \frac{A}{r} f(\theta, \phi) e^{ik_f r} \,, \tag{1.12}$$

where $f(\theta, \phi)$ contains the variation of the scattered wave as a function of angles (θ, ϕ) and is referred to as the "scattering amplitude" and k_f is the final wave-number post-scatter. The flux of the scattered wave is then

$$j_f = v_f \left(\frac{|A|^2 |f(\theta, \phi)|^2}{r^2} \right) = \frac{\hbar}{\mu} k_f \left(\frac{|A|^2 |f(\theta, \phi)|^2}{r^2} \right) . \tag{1.13}$$

Integration of the scattered flux, j_f, over the surface of a sphere of radius R (the solid angle element becomes $R^2 d\Omega$) shows

$$\int j_f R^2 d\Omega = \int \frac{\hbar}{\mu} k_f \left(\frac{|A|^2 |f(\theta, \phi)|^2}{R^2} \right) R^2 d\Omega = \frac{\hbar}{\mu} k_f |A|^2 \int |f(\theta, \phi)|^2 d\Omega \,,$$

meaning the total flux is constant and independent of the separation distance r.

The scattering wavefunction is then represented as a combination of the initial (Equation 1.10) and final (Equation 1.12) wavefunctions

$$\psi(r) = \psi_i(r) + \psi_f(r) = A \left(e^{ik_i r} + f(\theta, \phi) \frac{e^{ik_f r}}{r} \right) . \tag{1.14}$$

which is valid in the regions far away from the effects of the potential $V(r)$.

The differential angular cross section, Equation 1.3, is found by taking a ratio of the angular flux j_f (multiplied by r^2 to account for the solid angle at r) to the initial flux resulting in

$$\frac{d\sigma}{d\Omega}(\theta, \phi) = \frac{j_f}{j_i} = \frac{\frac{\hbar}{\mu} k_f |A|^2 |f(\theta, \phi)|^2}{\frac{\hbar}{\mu} k_i |A|^2} = \frac{k_f}{k_i} |f(\theta, \phi)|^2 \,, \tag{1.15}$$

and shows the independence of the differential angular cross section of the wave amplitude, A. In the case of elastic scattering, the kinetic energy is constant meaning $k_f = k_i$, simplifying Equation 1.15 to

$$\frac{d\sigma_{el}}{d\Omega}(\theta, \phi) = |f(\theta, \phi)|^2 \,, \tag{1.16}$$

and using Equation 1.4 produces the elastic integrated cross section, given in Equation 1.17, as

$$\sigma_{el} = \int \frac{d\sigma_{el}}{d\Omega}(\theta, \phi) d\Omega = \int |f(\theta, \phi)|^2 d\Omega \,. \tag{1.17}$$

1.1.2 Spherical Potential Scattering

Equation 1.17 suggests that for elastic scattering all that needs to be accomplished is solving and describing the scattering amplitude. With simplification and motivation drawn from Refs. [1, 3], one can treat the scattering potential as a spherical potential that extends to some defined limit R. Given the spherical nature of the scattering potential, and the projectile particles traveling along a given axis, this reduces the scattering amplitude to be dependent only upon a single angle θ, the angle of the scattered particle with respect to the incident axis, $f(\theta, \phi) \rightarrow f(\theta)$. The wavefunction of the scattering system, given in Equation 1.14 can be expanded in terms of Legendre polynomials, $P_\ell(\cos\theta)$ with ℓ relating to the order of the Legendre polynomial and angular momentum of the "partial wave". Legendre polynomials are beneficial as they can be expanded to higher orders (meaning the wave can be expressed as a sum of partial-waves) to describe the wavefunction and are eigenfunctions of the angular momentum operators $\hat{L}^2$ and $\hat{L}_z$ with eigenvalues of $\ell(\ell+1)$.

Consequently, Equation 1.14 can be recast as

$$\psi(r, \theta) = \sum_{\ell=0}^{\infty} (2\ell + 1) i^\ell P_\ell(\cos\theta) \frac{1}{kr} \chi_\ell(r) \,, \tag{1.18}$$

with i being the imaginary number $i = \sqrt{-1}$, k the wavenumber defined previously, and $\chi_\ell(r)$ is the radial partial wavefunction that satisfies the radial partial-wave Schrödinger equation given by

$$\left[-\frac{\hbar^2}{2\mu} \left(\frac{d^2}{dr^2} - \frac{\ell(\ell+1)}{r^2} \right) + V(r) \right] \chi_\ell(r) = E \chi_\ell(r) \,, \tag{1.19}$$

where $V(r)$ is the spherical scattering potential and E is the energy of the partial-wave for $\chi_\ell(r)$. In order to solve Equation 1.19, it is beneficial to rewrite the equation into a solvable second-order differential equation as a variable of the form $Bu_\ell(r) = \chi_\ell(r)$ with B being a

complex constant

$$u_\ell''(r) = \left[\frac{\ell(\ell+1)}{r^2} + \frac{2\mu}{\hbar^2}(V(r) - E)\right] u_\ell(r)\,. \tag{1.20}$$

It is possible to match the internal wavefunction to the external wavefunction at the boundary of the scattering potential R. This results in a linear combination of an interior (in) and exterior (out) wave that is given by

$$Bu_\ell(r) = \chi_\ell(r) \xrightarrow{r>R} \chi_\ell^{out}(r) = A_\ell \left[H_\ell^{in}(kr) - S_\ell H_\ell^{out}(kr)\right]\,, \tag{1.21}$$

with $H_\ell^{in}(kr)$ and $H_\ell^{out}(kr)$ being incoming and outgoing radial waves, and S_ℓ is the "partial-wave S-matrix element", and A_ℓ a complex constant. S_ℓ can be found by matching the first and last terms of Equation 1.21 and derivatives of $u_\ell(r)$ at a given radius a outside of the effective range of the potential ($a > R$).

Finally, one can arrive at an expression for the scattering amplitude given in Equation 1.22. Solving for $u_\ell(r)$, and therefore $\chi_\ell(r)$, using Equation 1.21, plugging back into Equation 1.18, and matching the wavefunction at the scattering potential boundary eventually produces

$$f(\theta) = \frac{1}{2ik}\sum_{\ell=0}^{\infty}(2\ell+1)P_\ell(\cos\theta)(S_\ell - 1)\,. \tag{1.22}$$

Equation 1.22 nicely shows the relationship between the angular momentum of a wave and the relation to a scattering amplitude, and therefore the differential angular cross section and integrated cross section. This derivation is valid for potentials such that an asymptotic wavefunction at infinite radius (r=∞) is described by Equation 1.21. Reality is, unfortunately, not as simple as there are a combination of forces that have long range interactions such as the Coulomb force. Additionally, quantum properties, such as spin, will vary across different nuclei and are important to include in the development of more refined theories to describe the physics of scattering with nuclei.

1.1.3 R-matrix Formalism

One modern theory attempting to describe measured scattering data is the R-Matrix theory with the early concept of the theory given by Kapur & Peierls [4] and further refined

by Wigner & Eisenbud [5]. A detailed explanation of the theory is provided by Lane & Thomas [6]. Within a cross section, there can be dramatic changes/structures that are commonly referred to as "resonances." The R-matrix theory attempts to explain and describe resonances across all angles given the fact resonances can vary strongly across angles and energies. The success of the R-matrix theory comes from the use of physical observable quantities such as spin, parity, and state energy (to name a few) to describe resonances while being a phenomenological approach to observed data [6, 7]. Additionally, R-matrix theory can not only describe resonances but also does well in regions far away from resonances where there can be a steady variation in the cross section.

The R-matrix theory tries to explain the cross section by separating the scattering problem into two regions: the internal and external regions [8]. For a given reaction channel α, the boundary of the two regions is known as the "channel radius", a_α and is chosen to be large such that in the external region the scattering potential V, dictated by the nuclear force, effects on the external wavefunction, ψ_α^{out}, are negligible and are only impacted by known long-range forces. A schematic of the two regions and related properties are shown in Figure 1.1.

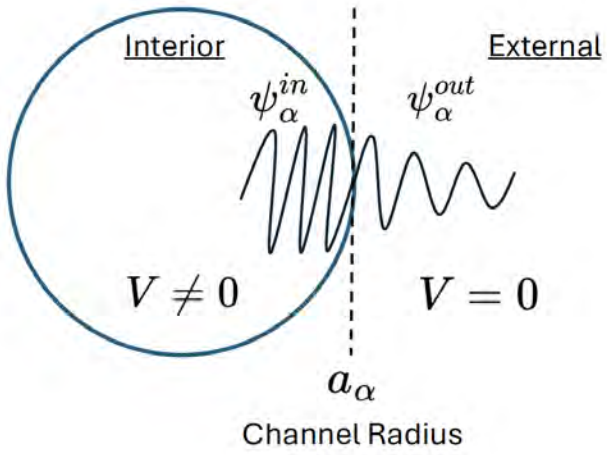

Figure 1.1 The two regions of the scattering problem as characterized by the R-matrix theory. The interior wavefunction ψ_α^{in} experiences a non-zero potential, V, at values of r less than the channel radius a_α. In the external region, the wavefunction, ψ_α^{out} experiences no potential from the scattering system. The wavelike structure is the representation of the two differing wavefunctions. Figure inspired by Ref. [8].

Within the interior region the wavefunction, ψ_α^{in}, is considered confined, through the existence of a non-zero potential V, and thus can reproduce known energy states. Solving the Schrödinger equation then becomes

$$\text{Interior}: \ (H_o + V)\psi_\alpha^{in} = E\psi_\alpha^{in} \tag{1.23}$$

$$\text{Exterior}: \qquad H_o\psi_\alpha^{ext} = E\psi_\alpha^{ext}\,, \tag{1.24}$$

with nuclear force given by V and a nuclear Hamiltonian given by H_o. The corresponding external wavefunction has a general solution [8] satisfying Equation 1.24 of the form

$$\psi_\alpha^{ext} = \left[\delta_{\alpha\alpha'} I_{\alpha'}(r) - S_{\alpha\alpha'} O_{\alpha'}(r)\right] \phi_{\alpha'}\,, \tag{1.25}$$

with incoming ($I_{\alpha'}$) and outgoing ($O_{\alpha'}$) waves modulated by $\delta_{\alpha\alpha'}$ (Kronecker-delta) and the "S-matrix" ($S_{\alpha\alpha'}$) respectively, with $\phi_{\alpha'}$ being the channel wavefunction on the surface of a sphere with $r = a_\alpha$ and includes the spin and parity of the channel. The observables from data are calculated in the S-matrix that is defined at the surface of the channel radius boundary.

Solving the Schrödinger equation becomes more difficult for the interior region but the R-matrix, defined in Equation 1.26, can be used to match to the observed resonances and features seen in the data. The benefits of this treatment allows for a calculation of a reaction channel to be made without assuming any nuclear potential and has an easier application to nuclear data evaluation. The R-matrix is defined as

$$R_{\alpha\alpha'} = \sum_\lambda \frac{\gamma_{\lambda\alpha}\gamma_{\lambda\alpha'}}{E_\lambda - E}\,, \tag{1.26}$$

for a level λ, with $\gamma_{\lambda\alpha}$ and $\gamma_{\lambda\alpha'}$ being "reduced-width amplitudes" (containing the information of a given level λ for a channel α such as spin, parity, etc.) with a proportionality $\gamma_{\lambda\alpha} \propto \int_{r=a_\alpha} \phi_\alpha^* X_\lambda dS$, at the surface S of the channel radius for a channel wavefunction ϕ_α^* and wave X_λ, and the "energy-pole" E_λ (energy location of a resonance) [1, 3, 6, 8]. The $\gamma_{\lambda\alpha}$, $\gamma_{\lambda\alpha'}$, and E_λ are all fit parameters based on the observable data (cross sections) and therefore makes the R-matrix theory a phenomenological approach.

A critique of the R-matrix theory is the apparent choice of the channel radius which directly impacts the reduced-width amplitudes and energy poles [9]. Even though the R-matrix theory is phenomenological, the inputs are grounded in physical observables and can successfully describe resonances and regions distant from resonances as is the case for inelastic and elastic data of ^{12}C neutron scattering [8]. For further theoretical developments data pertaining to nuclear reactions are needed.

1.2 Nuclear Data & Applications

Neutron reactions have been studied since the early days of nuclear physics [10] and have had numerous experimental results regarding cross sections, fission fragment distributions, prompt fission neutron spectra, and much more. Nuclear data serve as a valuable reference for categorizing and characterizing different nuclei and their interactions. Such data can be used in simulations, such as GEANT4 (**GE**ometry **AN**d **T**racking 4) [11]. Simulations rely upon nuclear databases to simulate multi-particle reactions that can undergo a plethora of possible reaction pathways. If the information/data pertaining to the reaction is lacking, poorly understood, and/or missing uncertainty quantification, there can be negative impacts on the results that depend on the knowledge of well characterized nuclear data. The value of nuclear data is also stressed in the most recent "Nuclear Long Range Plan" [12] (an executive summary describing the important areas of research pertaining to the United States nuclear science community) through the applications in scientific and technological developments, national security missions, teaching environments, and implementation in simulation codes.

Nuclear data evaluations serve as a reference for nuclear data quantities representing the best results of the nuclear physics community given the experimental literature datasets. Nuclear data evaluations are comprised of multi-institutional organizations that work together to compile the vast amounts of nuclear data available throughout varying literature sources. Some common nuclear data evaluation organizations include the Evaluated Nuclear Data File (ENDF - USA) [13], the Joint Evaluated Fission and Fusion (JEFF - Europe) [14], the Japanese Evaluated Nuclear Data Library (JENDL - Japan) [15], and the Chinese Evaluated

Nuclear Data Library (CENDL - China)[16]. For the work presented, ENDF will be used as the primary nuclear data evaluation for comparisons, in particular ENDF/B-VIII.0 (8th major release), unless otherwise stated.

Within the United States, the primary program handling nuclear data related activities is the **US** **N**uclear **D**ata **P**rogram (USNDP) [17] which is the main custodian of nuclear data (within the U.S.) with the goal to provide accurate and up-to-date nuclear data available for public use. Nuclear data quantities can be obtained from the **N**ational **N**uclear **D**ata **C**enter (NNDC) [18] where nuclear data quantities such as the half-lives, cross sections, and energy levels pertaining to different nuclei are available. Nuclear data needs between academic, government, and industry are addressed through a variety of conferences, meetings, and workshops such as the **W**orkshop for **A**pplied **N**uclear **Da**ta (WANDA) which aid in the compilation, evaluation, and data handling activities undertaken by the USNDP.

Despite all of the data already available via published literature and evaluations, information for many reactions can be lacking or missing altogether such as neutron scattering on common, stable nuclei. Studies dependent on neutron scattering data, such as neutron transport simulations, can suffer from inaccuracies and large uncertainties due to lack of existing information. One such example where detailed knowledge of neutron transport is needed is in active interrogation-the use of ionizing radiation to determine and identify materials through knowledge of nuclear reactions [19]. This process typically involves using 14 MeV neutrons to irradiate objects of interest and involve measuring the subsequent radiation [20, 21]. Inelastic scattering frequently results in the emission of gamma rays which can be measured for material identification. Measuring the neutron intensity after object irradiation can provide object construction and density information, similar to that of an x-ray image. The neutron intensity will be dependent upon scattered (elastic and inelastic) neutrons.

There are also experimental setups that rely on the detection of neutrons for fundamental science studies, such as The MoNA Collaboration [22] that is actively conducting an

experimental program centrally located at the Facility for Rare Isotope Beams (FRIB) of Michigan State University (MSU) with the goal of experimentally probing nuclei that lie near the neutron dripline. This is accomplished through invariant mass spectroscopy to measure neutron unbound resonances with charged particle detectors and plastic scintillators to detect neutrons, MoNA/LISA [23, 24]. The use of plastic scintillators (hydrocarbon material) make MoNA and LISA prone to "dark scattering" (no measurable light from neutrons elastically scattering off carbon inside the detector) and can introduce compounding errors [25]. Knowledge of neutron elastic scattering for simulation efforts are thus needed to correct for this effect [26], and rely upon accurate neutron scattering cross section measurements.

1.3 Neutron Data Standards

Neutron Data Standards, neutron reaction data with measured values and shape that are well known, serve as a valuable reference for nuclear reaction experiments. Some neutron cross section standards include: C(n,n), H(n,n), ^{6}L(n,t), ^{10}B(n,α), and ^{238}U(n,f) over designated neutron energy ranges [13, 27]. An additional neutron standard includes the prompt fission neutron spectrum (PFNS) of ^{252}Cf [13, 27] as used in this work. Many neutron cross section measurements are classified as "reference" measurements with respect to a standard quantity, given the reduced uncertainty in the evaluated standard and desirable shape (linear, exponential, logarithmic, etc.) [28], along with the desire/added uncertainty that comes with measuring a non-standard neutron flux.

The current neutron data standards, last produced in 2017, are evaluated and reported by the Cross Section Evaluation Working Group (CSEWG) and the International Atomic Energy Agency (IAEA) [27] with the evaluated data easily accessible on the IAEA's website using Ref. [29].

A neutron data standard quantity can therefore serve as a "check" on the neutrons/reactions that are measured experimentally. For example, the PFNS of ^{252}Cf can be used to understand how well a detector measures known neutrons energies. The PFNS of ^{252}Cf is a standard from 10 μeV to 30 MeV and therefore allows one to understand the efficiency of a detec-

tor across this range. Similarly, the elastic scattering cross section off natural carbon is a neutron standard on the range of 10 eV to 1.8 MeV. For cross section measurements pertaining to carbon, as done in this work, this energy range should match with the accepted neutron cross section in order to have confidence regarding any reported values outside of the standard range. Additionally, the ^{235}U(n,f) cross section is a neutron data standard within an incident neutron energy range of 0.15 – 200 MeV with ^{235}U being used in neutron flux measuring devices. The ^{252}Cf PFNS, ^{nat}C (n, el) cross section, and the ^{235}U(n,f) cross section are neutron data standards used in this work.

1.4 Carbon - Neutron Scattering

Carbon is highly prevalent in nearly every aspect of life given its use in structural materials, nuclear reactors, shielding, and more. Given the prevalence of carbon and the fact that it is considered a neutron data standard (see Section 1.3), used in reference measurements, a detailed understanding of the neutron elastic cross section and the neutron angular distribution is valuable. Additionally, neutrons with energies in the fast region (1-100's MeV in order of magnitude and range) primarily scatter via both elastic and inelastic reactions.

Nuclear data in the fast region for neutron scattering off carbon is limited. Measurements of the neutron elastic scattering cross section for ^{12}C that are published and available on EXFOR (**Ex**change **For**mat, experimental nuclear database with associated Web interface) [30], within the energy range discussed in this work, are shown in Figure 1.2. In this work, the neutron elastic scattering cross section of ^{12}C is used so that a direct comparison with the associated evaluation in ENDF can be made along with the fact that ^{12}C comprises 98.84 - 99.04 % [31] of naturally occurring carbon.

Published measurements come from Refs. [32, 33, 34, 35, 36, 37, 38, 39] with the ^{12}C neutron elastic scattering evaluation coming from reference [40]. In Figure 1.2, one can clearly see that there is a need to measure the neutron elastic scattering cross section across a wider range of energies than is currently available in the EXFOR database. Additionally, given the fact that carbon is a neutron standard up to 1.8 MeV, as discussed in Section

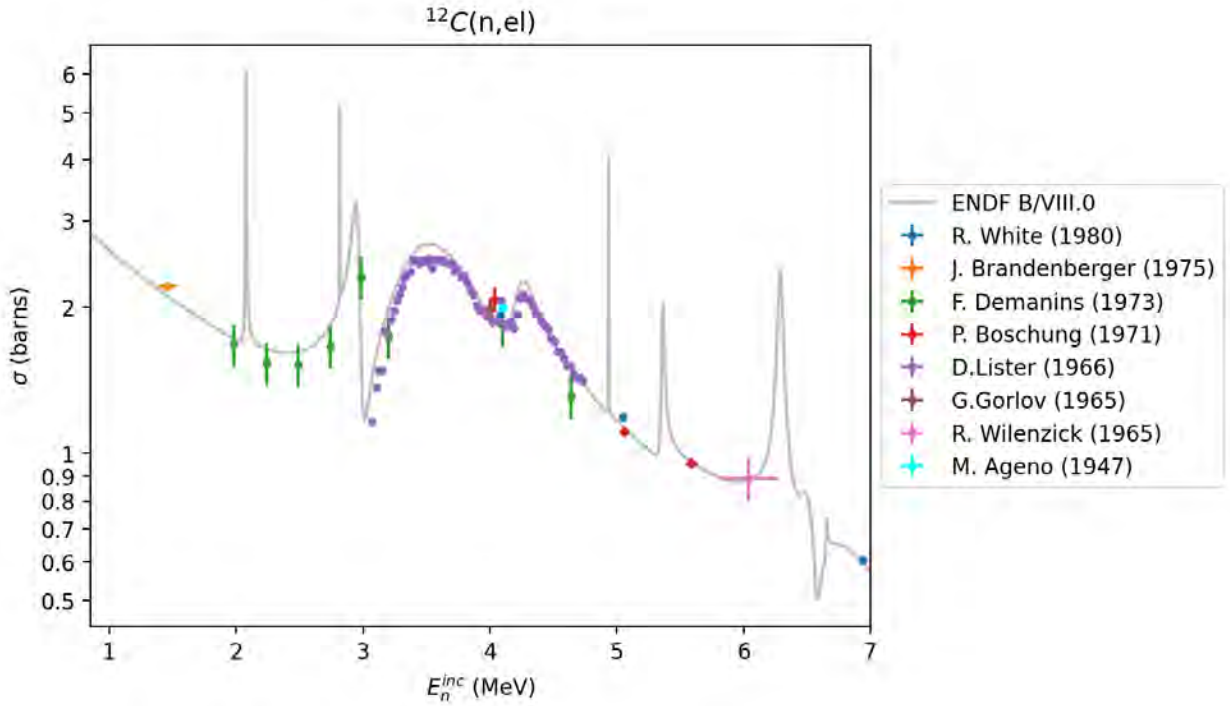

Figure 1.2 Reported and available neutron elastic scattering cross section data obtained from EXFOR as a function of incident neutron energy E_n^{inc}. Only the first author from the respective publications are listed for brevity.

1.3, this "standard region" serves as an "anchor point" and check against experimentally measured results that are presented in this work and given in Chapter 5. The total cross section of carbon is equal to the elastic scattering cross section until the threshold for inelastic scattering is possible from the first excited state at 4.4398 MeV. Therefore, based on prior measurements of the ^{12}C total cross section, the structures below $E_n^{inc} = 4.4398$ MeV are well known and there should be shape agreement between the evaluation and the presented work.

1.5 Relativistic Scattering Kinematics

The kinematics of a scattering event should be described relativistically for fast neutron interactions. The neutron kinetic energy E_n is given by

$$E_n = m_n c^2 (\gamma - 1) \ , \tag{1.27}$$

where m_n is the mass of the neutron, 939.56542194(48) MeV/c^2, γ is the Lorentz factor (gamma factor) defined as $\frac{1}{\sqrt{1-v^2/c^2}} = \frac{1}{\sqrt{1-\beta^2}}$, c is the speed of light, and β is equal to $\frac{v}{c}$. Determination of the neutron kinetic energy can be accomplished via the time-of-flight (ToF) technique. Knowledge of the distance and time that the neutron traverses can allow for the calculation of the neutron kinetic energy. Experimentally, the distance of the flight-path of the neutron is known. Equation 1.27 can be modified to be a function of time and distance

$$E_n = m_n c^2 \left(\frac{1}{\sqrt{1-\frac{v^2}{c^2}}} - 1 \right) = m_n c^2 \left(\frac{1}{\sqrt{1-\left(\frac{d}{ct}\right)^2}} - 1 \right) , \tag{1.28}$$

where d is the distance of the neutron flight-path and t is the time the neutron takes to travel the flight-path distance.

A scattering reaction will typically consist of differing flight-paths: the distance from the neutron source to the scattering target and the distance from the scattering target to the detector. For the remainder of this work, the following notion will be used: quantities pertaining to the center-of-mass (CM) will have a tilde over the quantity $\tilde{x}$ whereas quantities in the Lab frame (L) will be presented as x.

The use of 4-vectors, P_x, allows for the description of a system to be described by establishing a relationship between related quantities: space & time ($\vec{r}$, t), and energy & momentum (E, $\vec{p}$). The complete 4-vectors are constructed as

$$\text{Space-Time} : \; P_x = \langle ct, \vec{r} \rangle = \langle ct, \vec{x}, \vec{y}, \vec{z} \rangle \tag{1.29}$$

$$\text{Energy-Momentum} : \; P_x = \left\langle \frac{E}{c}, \vec{p} \right\rangle = \left\langle \frac{E}{c}, \vec{p_x}, \vec{p_y}, \vec{p_z} \right\rangle . \tag{1.30}$$

It is also useful to use invariant quantities, a quantity that is reference (frame) independent, to establish links between the L and CM frames. An extremely useful and well-known invariant quantity is the invariant mass, m_o , and is used to establish the energy-momentum relation

$$E^2 = (pc)^2 + \left(m_o c^2\right)^2 . \tag{1.31}$$

Similarly, the magnitude of the energy-momentum 4-vector, P_1P_2, is defined as

$$P_1P_2 = \left\langle \frac{E_1}{c}, \vec{p_1} \right\rangle \cdot \left\langle \frac{E_2}{c}, \vec{p_2} \right\rangle = \frac{E_1E_2}{c^2} - \vec{p_{1_x}} \cdot \vec{p_{2_x}} - \vec{p_{1_y}} \cdot \vec{p_{2_y}} - \vec{p_{1_z}} \cdot \vec{p_{2_z}} = \frac{E_1E_2}{c^2} - \vec{p_1} \cdot \vec{p_2}\,, \tag{1.32}$$

which is an invariant quantity. For the case of finding the magnitude of the same 4-vector, the magnitude is simply $P_1P_1 = m_oc^2$. The same can be done for obtaining the CM total energy through the use of 4-vectors and invariant quantities by

$$\tilde{E}^2 = (P_1 + P_2)^2 = P_1^2 + P_2^2 + 2P_1P_2 = \left(m_1c^2\right)^2 + \left(m_2c^2\right)^2 + 2\left(\frac{E_1E_2}{c^2} - \vec{p_1} \cdot \vec{p_2}\right). \tag{1.33}$$

Note the usage of the L frame quantities which is allowable given the fact that the total CM energy $\tilde{E}^2$ is an invariant quantity and the same can be derived using CM quantities ($\tilde{E}$ and $\tilde{\vec{p}}$). This is useful given the fact that experimental quantities are measured in the L frame and a relationship, in addition to Lorentz transformations, can be established between the CM and L frame.

A transformation from the CM to L frame can be accomplished utilizing Lorentz transformations with the 4-vectors. For the energy-momentum 4-vector boosted in the $\vec{v}$ (velocity vector between CM and L frame) direction, the relation proceeds as

$$\text{Energy}: \; E = \gamma\left(\tilde{E} + \vec{\beta} \cdot \tilde{\vec{p}}c\right) \tag{1.34}$$

$$\text{Momentum}: \; \vec{p}c = \tilde{\vec{p}}c + (\gamma - 1)\left(\tilde{\vec{p}}c \cdot \vec{v}/v\right)\vec{v}/v + \gamma E\vec{\beta}\,. \tag{1.35}$$

A unique property of the CM frame is that the total momentum in the CM frame is equal to 0. This fact can be useful to exploit in solving for a variety of different kinematic quantities with respect to scattering.

It is desirable to know the energy of the neutron n after a scattering event with the scattering target (^{12}C) has occurred as measured in the L frame E_n^{emit}. This can be accomplished by modifying Equation 1.34 by utilizing the following definitions : $\vec{a} \cdot \vec{b} = ab\cos(\theta)$ and $\vec{\beta} = \frac{\vec{v}}{c}$. Additionally, natural units will be utilized from this point forward (unless stated

otherwise), $c = 1$, to help make the relations between kinematic quantities more clear. This results in

$$E_n^{emit} = \gamma \left(\tilde{E}_n^{emit} + \beta \tilde{p}_n^{emit} \cos \tilde{\theta}_n^{emit} \right) , \tag{I}$$

with $\tilde{E}_n^{emit}$ being the energy of the emitted neutron in the CM frame, $\tilde{p}_n^{emit}$ is the momentum of the neutron in the CM frame and $\tilde{\theta}_n^{emit}$ is the angle at which the neutron scattered from beam axis in the CM frame. Note that equations of significance pertinent to the analysis for neutron elastic scattering, as discussed in this work, will utilize roman numerals for labels. It is useful to express the Lorentz factor γ as a function of the energy and momenta of the particles participating in a scattering event. This is done by using Equation 1.34 by solving for γ. In the CM frame, the total momentum is 0 (by definition) making $\tilde{\vec{p}} = \vec{0}$. The 4-vectors for the particles in the L frame before scattering will be $P_n = \langle E_n, \vec{p_n} \rangle = \langle E_n^{inc} + m_n, \vec{p_n} \rangle$ and $P_C = \left\langle E_C, \vec{0} \right\rangle = \left\langle m_C, \vec{0} \right\rangle$. This results, with the help of Equation 1.33, in the following

$$\gamma = \frac{E}{\tilde{E}} = \frac{E_n + m_C}{\sqrt{m_n^2 + m_C^2 + 2E_n m_C}} . \tag{II}$$

Note that the numerator in Equation II is the total energy of the system in the L frame, this can be simplified to

$$E_{tot} = E_n + E_C = E_n^{inc} + m_n + m_C , \tag{III}$$

and utilizing Equation II the CM total energy follows as

$$\tilde{E}_{tot} = \frac{E_{tot}}{\gamma} . \tag{IV}$$

To solve for the energy of the emitted neutron in the CM frame $\tilde{E}_n^{emit}$, the total energy of the system $\tilde{E}_{tot}$ is the same before and after a scattering event has occured. Therefore, the total energy of the system can be written as $\tilde{E}_{tot} = \tilde{E}_n^{emit} + \tilde{E_C}$. Rearranging the terms for the total energy of the system in the CM frame and solving for $\tilde{E}_n^{emit}$ produces

$$\begin{aligned} \tilde{E}_C^2 &= (\tilde{E}_{tot} - \tilde{E}_n^{emit})^2 \\ m_C^2 + \tilde{p}_C^2 &= \tilde{E}_{tot}^2 + [\tilde{E}_n^{emit}]^2 - 2\tilde{E}_{tot}\tilde{E}_n^{emit} \\ m_C^2 + \tilde{p}_C^2 &= \tilde{E}_{tot}^2 + m_n^2 + \tilde{p_n^i}^2 - 2\tilde{E}_{tot}\tilde{E}_n^{emit} , \end{aligned}$$

while knowing that in the CM frame the magnitude of the momenta for carbon and the neutron are equal $|p_n^i| = |p_C|$, the energy of the emitted neutron can be presented as

$$\tilde{E}_n^{emit} = \frac{1}{2\tilde{E}_{tot}} \left(\tilde{E}_{tot}^2 + m_n^2 - m_C^2 \right) , \tag{V}$$

and the emitted neutron momentum can be obtained using Equation 1.31 and V to yield

$$\tilde{p}_n^{emit} = \sqrt{[\tilde{E}_n^{emit}]^2 - m_n^2} \, . \tag{VI}$$

Progressing along with the variables in Equation I, the frame velocity β can be found by rearranging the definition of the Lorentz factor to be:

$$\beta = \sqrt{1 - \frac{1}{\gamma^2}} \, . \tag{VII}$$

In order to solve for the CM scattering angle $\tilde{\theta}_n^{emit}$, the angle between the scattered neutron and carbon, one can leverage Equation 1.35 along with algebraic manipulations to arrive at a relation between the CM scattering angle $\tilde{\theta}_n^{emit}$ and the measured L frame angle of the scattered neutron θ_n^{emit}. Equation 1.35 can be expanded to more clearly show the relationship of the different quantities as:

$$\begin{aligned}
\vec{p}_n^{\,emit} &= \tilde{\vec{p}}_n^{\,emit} + (\gamma - 1) \left(\tilde{\vec{p}}_n^{\,emit} \cos\tilde{\theta}_n^{emit} \right) + \gamma \tilde{E}_n^{emit} \vec{\beta} \\
&= \tilde{\vec{p}}_n^{\,emit} + \gamma \tilde{\vec{p}}_n^{\,emit} \cos\tilde{\theta}_n^{emit} - \tilde{\vec{p}}_n^{\,emit} \cos\tilde{\theta}_n^{emit} + \gamma \tilde{E}_n^{emit} \vec{\beta} \\
&= \tilde{\vec{p}}_n^{\,emit} - \tilde{\vec{p}}_n^{\,emit} \cos\tilde{\theta}_n^{emit} + \gamma \left(\tilde{\vec{p}}_n^{\,emit} \cos\tilde{\theta}_n^{emit} + \tilde{E}_n^{emit} \vec{\beta} \right) \\
\vec{p}_{n_\perp}^{\,emit} + \vec{p}_{n_\parallel}^{\,emit} &= \tilde{\vec{p}}_{n_\perp}^{\,emit} + \tilde{\vec{p}}_{n_\parallel}^{\,emit} \, .
\end{aligned}$$

If the corresponding L frame parallel and perpendicular components of the emitted neutron momentum are matched with the respective CM parallel and perpendicular components and knowing that through the addition of vectors that $\tilde{p}_n^{\,emit} \sin\tilde{\theta}_n^{emit} = \tilde{\vec{p}}_n^{\,emit} - \tilde{\vec{p}}_n^{\,emit} \cos\tilde{\theta}_n^{emit}$

$$\begin{aligned}
\text{Parrallel Components} : \; & p_{n_\parallel}^{emit} \cos\theta_n^{emit} = \gamma \left(\tilde{p}_n^{\,emit} \cos\tilde{\theta}_n^{emit} + \tilde{E}_n^{emit} \beta \right) \\
\text{Perpendicular Components} : \; & p_{n_\perp}^{emit} \sin\theta_n^{emit} = \tilde{p}_n^{\,emit} \sin\tilde{\theta}_n^{emit} \, ,
\end{aligned}$$

and dividing the two equations against each other results in

$$\cot\theta_n^{emit} = \gamma\frac{\cos\tilde{\theta}_n^{emit} + \rho_n^{emit}}{\sin\tilde{\theta}_n^{emit}}\,, \tag{1.36}$$

where ρ_n^{emit} is introduced to simply the equations and is defined as

$$\rho_n^{emit} = \frac{\tilde{E}_n^{emit}\beta}{\tilde{p}_n^{\,emit}}\,. \tag{VIII}$$

In an effort to isolate $\tilde{\theta}_n^{emit}$, squaring both sides of Equation 1.36 leads to

$$\cot^2\theta_n^{emit} = \gamma^2\frac{\cos^2\tilde{\theta}_n^{emit} + \rho_n^{emit^2} + 2\rho_n^{emit}\cos\tilde{\theta}_n^{emit}}{1-\cos^2\tilde{\theta}_n^{emit}}$$

$$\cot^2\theta_n^{emit} - \cot^2\theta_n^{emit}\cos^2\tilde{\theta}_n^{emit} = \gamma^2\cos^2\tilde{\theta}_n^{emit} + \gamma^2\rho_n^{emit^2} + 2\gamma^2\rho_n^{emit}\cos\tilde{\theta}_n^{emit}\,,$$

and with some rearranging

$$0 = \left(\gamma^2 + \cot^2\theta_n^{emit}\right)\cos^2\tilde{\theta}_n^{emit} + \left(2\gamma^2\rho_n^{emit}\right)\cos\tilde{\theta}_n^{emit} + \left(\gamma^2\rho_n^{emit^2} - \cot^2\theta_n^{emit}\right)\,.$$

Note that this is in the form of a quadratic equation. Applying the quadratic formula results in

$$\begin{aligned}
\cos\tilde{\theta}_n^{emit} &= \frac{-2\gamma^2\rho_n^{emit} \pm \sqrt{4\gamma^4\rho_n^{emit^2} - 4\left(\gamma^2 + \cot^2\theta_n^{emit}\right)\left(\gamma^2\rho_n^{emit^2} - \cot^2\theta_n^{emit}\right)}}{2\left(\gamma^2 + \cot^2\theta_n^{emit}\right)} \\
&= \frac{-\gamma^2\rho_n^{i} \pm \sqrt{\gamma^4\rho_n^{emit^2} - \gamma^4\rho_n^{emit^2} + \gamma^2\cot^2\theta_n^{emit} - \gamma^2\rho_n^{emit^2}\cot^2\theta_n^{emit} - \cot^4\theta_n^{emit}}}{\gamma^2 + \cot^2\theta_n^{emit}} \\
&= \frac{-\gamma^2\rho_n^{emit} \pm \cot\theta_n^{emit}\sqrt{\gamma^2\left(1-\rho_n^{emit^2}\right) + \cot^2\theta_n^{emit}}}{\gamma^2 + \cot^2\theta_n^{emit}}\,.
\end{aligned}$$

It is important to know that $\rho_n^{emit} > 1$ and therefore results in the use of a "+" to keep the numerator a positive quantity. Therefore, the CM neutron emitted scattering angle is related to its respective L angle by

$$\tilde{\theta}_n^{emit} = \arccos\left(\frac{-\gamma^2\rho_n^{emit} + \cot\theta_n^{emit}\sqrt{\gamma^2\left(1-[\rho_n^{emit}]^2\right) + \cot^2\theta_n^{emit}}}{\gamma^2 + \cot^2\theta_n^{emit}}\right)\,. \tag{IX}$$

In the CM frame, the emitted neutron angle will be the same as the detected angle in the CM frame and the same reasoning is true for the L frame angles, as these are already known

by the experimenter. Additionally, a particle emitted into a solid angle in the CM frame will be emitted into a corresponding but different solid angle in the L frame such that integrating across a range of angles, either in the CM or L frame, results in the integrated cross section being the same in both the CM and L frame. Mathematically, this is represented as

$$\frac{d\sigma}{d\tilde{\Omega}}\left(\tilde{\theta}_n^{emit},\tilde{\phi}_n^{emit}\right)\sin\tilde{\theta}_n^{emit}d\tilde{\theta}_n^{emit}d\tilde{\phi}_n^{emit}=\frac{d\sigma}{d\Omega}\left(\theta_n^{emit},\phi_n^{emit}\right)\sin\theta_n^{emit}d\theta_n^{emit}d\phi_n^{emit}. \tag{1.37}$$

Note that the ϕ axis is the same in both the L and CM frame so $d\tilde{\phi}_n^{emit}=d\phi_n^{emit}$. In order to turn Equation 1.37 into factors of experimental parameters, one needs to know how $d\tilde{\theta}_n^{emit}$ and $d\theta_n^{emit}$ can be represented as known quantities. This is accomplished by utilizing Equation 1.36 and differentiating both sides with respect to θ', the differential angle in either the CM ($d\tilde{\theta}_n^{emit}$) or L frame ($d\theta_n^{emit}$), results in the following

$$\begin{aligned}
\frac{d}{d\theta'}\left[\cot\theta_n^{emit}\right]&=\frac{d}{d\theta'}\left[\gamma\frac{\cos\tilde{\theta}_n^{emit}+\rho_n^{emit}}{\sin\tilde{\theta}_n^{emit}}\right]\\
\frac{-1}{\sin^2\theta_n^{emit}}d\theta_n^{emit}&=\frac{\left(-\gamma\sin\tilde{\theta}_n^{emit}d\tilde{\theta}_n^{emit}\right)\left(\sin\tilde{\theta}_n^{emit}\right)-\left(\cos\tilde{\theta}_n^{emit}d\tilde{\theta}_n^{emit}\right)\left(\gamma\cos\tilde{\theta}_n^{emit}+\gamma\rho_n^{emit}\right)}{\sin^2\tilde{\theta}_n^{emit}}\\
\frac{d\theta_n^{emit}}{d\tilde{\theta}_n^{emit}}&=\gamma\left(1+\rho_n^{emit}\cos\tilde{\theta}_n^{emit}\right)\frac{\sin^2\theta_n^{emit}}{\sin^2\tilde{\theta}_n^{emit}},
\end{aligned} \tag{1.38}$$

If the CM differential angular cross section is isolated in Equation 1.37 and plugging in Equation 1.38 produces

$$\begin{aligned}
\frac{d\sigma}{d\tilde{\Omega}}\left(\tilde{\theta}_n^{emit}\right)&=\frac{d\sigma}{d\Omega}\left(\theta_n^{emit}\right)\frac{\sin\theta_n^{emit}}{\sin\tilde{\theta}_n^{emit}}\frac{d\theta_n^{emit}}{d\tilde{\theta}_n^{emit}}\\
\frac{d\sigma}{d\tilde{\Omega}}\left(\tilde{\theta}_n^{emit}\right)&=\frac{d\sigma}{d\Omega}\left(\theta_n^{emit}\right)\frac{\sin\theta_n^{emit}}{\sin\tilde{\theta}_n^{emit}}\left(\gamma\left(1+\rho_n^{emit}\cos\tilde{\theta}_n^{emit}\right)\frac{\sin^2\theta_n^{emit}}{\sin^2\tilde{\theta}_n^{emit}}\right),
\end{aligned}$$

with simplification finally yields

$$\frac{d\sigma}{d\tilde{\Omega}}\left(\tilde{\theta}_n^{emit}\right)=\frac{d\sigma}{d\Omega}\left(\theta_n^{emit}\right)\gamma\left(1+\rho_n^{emit}\cos\tilde{\theta}_n^{emit}\right)\frac{\sin^3\theta_n^{emit}}{\sin^3\tilde{\theta}_n^{emit}}, \tag{X}$$

showing that the distributions measured in the L frame require a scale factor to correct into the CM frame.

1.6 Uncertainties & Covariance

While obtaining a new cross section measurement over a range of incident neutron energies is valuable, understanding and quantifying the correlation between data points of a result is equally valuable for nuclear data evaluators and for users of nuclear data. Reporting covariance matrices for nuclear data quantifies the relationship between the recorded data (e.g. scattering cross section) over the range of the measured quantity (e.g, neutron incident energy E_n^{inc}).

The covariance, **Cov**, is a linear measure of how data points are related and in which direction the relationship is [41]. Values can range from $-\infty$ to ∞ where positive values indicate that the data change in the same direction, negative values indicate the data change in opposite direction, and 0 meaning there is no correlated relationship between the two quantities. Similarly, the correlation is the measure of the strength and direction of the relationship on a normalized range (-1 to 1) with uncertainty magnitude removed. Like the covariance, the value of the correlation, **Corr**, indicates if the data have positive relationship (positive correlation value and change in the same direction), negative correlation (opposite direction of change), or no correlation at all (correlation value of 0).

A more efficient process for presenting the relationship of the data is in the form of a matrix. The covariance matrix (and correlation matrix) then visually presents the relationship of quantities (such as the elastic scattering cross section) over the measured quantity. Each element (points i and j) in the matrix then provides the covariance value at the respective points. When two points are equal ($i = j$), the value of the covariance simplifies to the variance, **Var**, which is equal to the square of the standard deviation, where the standard deviation is the Gaussian uncertainty in the measured values [41, 42, 43].

For a given function $f(x)$, the covariance matrix is calculated utilizing matrix notation, as described in references [43, 44], and is shown in Equation 1.39

$$\mathbf{K}_f = \mathbf{AVA}^T\,, \tag{1.39}$$

where $\mathbf{K}_f$ is the covariance matrix of $f(x)$, $\mathbf{A}$ is the "sensitivity" matrix, and $\mathbf{V}$ is the

covariance matrix of quantities used in $f(x)$ (such as counts, flux, detector efficiency, etc.).

The sensitivity matrix $\mathbf{A}$ is conceptually a measure of how $f(x)$ varies with variable(s) x at different data points (i and j) [43, 44]. This amounts to taking the partial derivative of $f(x)$ at points i and j with respect to x. The sensitivity matrix is calculated, as presented in Ref. [44], as

$$\mathbf{A} = \begin{bmatrix} \frac{\partial f_i}{\partial x_1} & \cdots & \frac{\partial f_i}{\partial x_M} & \cdots & \frac{\partial f_i}{\partial x_N} \\ \frac{\partial f_j}{\partial x_1} & \cdots & \frac{\partial f_j}{\partial x_M} & \cdots & \frac{\partial f_j}{\partial x_N} \end{bmatrix}, \tag{1.40}$$

where x_M is a variable (counts, flux, detector efficiency, etc.) used in the calculation of $f(x)$, to the the total number of variables N, as shown in Equation 1.40.

The covariance matrix $\mathbf{V}$ is comprised of variances and covariances of x_M along the diagonal. The covariance matrix is constructed from previously understood quantities as

$$\mathbf{V} = \begin{bmatrix} \mathbf{Var}[x_{1_i}] & \mathbf{Cov}[x_{1_{ij}}] & 0 & 0 & 0 & 0 & 0 & 0 \\ \mathbf{Cov}[x_{1_{ji}}] & \mathbf{Var}[x_{1_j}] & 0 & 0 & 0 & 0 & 0 & 0 \\ 0 & 0 & \ddots & 0 & 0 & 0 & 0 & 0 \\ 0 & 0 & 0 & \mathbf{Var}[x_{M_i}] & \mathbf{Cov}[x_{M_{ij}}] & 0 & 0 & 0 \\ 0 & 0 & 0 & \mathbf{Cov}[x_{M_{ji}}] & \mathbf{Var}[x_{M_j}] & 0 & 0 & 0 \\ 0 & 0 & 0 & 0 & 0 & \ddots & 0 & 0 \\ 0 & 0 & 0 & 0 & 0 & 0 & \mathbf{Var}[x_{N_i}] & \mathbf{Cov}[x_{N_{ij}}] \\ 0 & 0 & 0 & 0 & 0 & 0 & \mathbf{Cov}[x_{N_{ji}}] & \mathbf{Var}[x_{N_j}] \end{bmatrix}, \tag{1.41}$$

where $\mathbf{Var}[x_{M_i}]$ is the variance (square of the Gaussian 1σ uncertainty) of x_M at data point i, $\mathbf{Var}[x_{M_j}]$ is the variance of x_M at data point j, and $\mathbf{Cov}[x_{M_{ij}}] = \mathbf{Cov}[x_{M_{ji}}]$ is the covariance of x_M at data points i and j if a covariance exists for such variable.

It is important to note, and is suggested that, when evaluating functions $f(x)$ they should be expressed in the "most fundamental" components, such as measured counts, referenced literature values, etc. as these are quantities that are best understood and formulate more complicated quantities such as cross sections. This allows for a methodical and detailed

propogation of uncertainties to be quantified and has the added advantage of having zeros in the majority of the off diagonals in Equation 1.41.

Carrying out the matrix multiplication in Equation 1.39 produces a covariance matrix $\mathbf{K}_f$ of function $f(x)$. The calculated covariance $\mathbf{K}_f$ contains the variance (square of the uncertainties) along the diagonal and the covariance on the off diagonals and should be symmetric about the diagonal. For plotted quantities, the uncertainties on presented data are obtained by taking the square root of the variance at each given data point.

CHAPTER 2

EXPERIMENTAL SETUP

The experiment for measuring the carbon neutron elastic scattering reaction was conducted during the 2023 run-cycle at the **W**eapons **N**eutron **R**esearch (WNR) Facility at the **L**os **A**lamos **N**eutron **Sc**ience C**e**nter (LANSCE) and used the neutron white source produced by the LANSCE accelerator. The experiment utilized the **Co**rrelated **G**amma **N**eutron **A**rray for s**C**attering (CoGNAC) setup for the cross section measurement. Each of the resources are described in the sections below.

2.1 Los Alamos Neutron Science Center (LANSCE)

The LANSCE facility [45], located at Los Alamos National Laboratory [46], was originally constructed during the late 1960's into the early 1970's. The highlighting feature of the facility is the linear accelerator (LINAC) that accerlates both positive H^+ (protons) and negative H^- hydrogen ions up to 800 MeV to make a proton beam [47]. A collection of similar ions are bunched together to make a pulsed beam that is sent through the LANSCE LINAC.

The first stage of the LANSCE LINAC involves sending the proton beam through the Drift Tube Linear Accelerator which increases the beam energy up to 100 MeV [48]. The H^+ beams are diverted from the original beam line to the Isotope Production Facility (IPF) to make a variety of isotopes for medical and societal needs. The H^- beam continues to the second stage Side-Coupled-Cavity Linear Accelerator which accelerates the beam to 800 MeV before being sent to any of the 6 experimental areas at LANSCE: Proton Radiography (pRad), Ultracold Neutrons (UCN), "Area A" (future experimental possibilities), Proton Storage Ring (PSR), Lujan Center, and WNR. The H^- beam gets charge-exchanged to be H^+ before reaching the "decision point" of being sent to Lujan, Blue Room (facility just before WNR), or WNR. A schematic of the LANSCE Facility and the WNR Facility are shown in Figure 2.1. The WNR facility is the location of the discussed experiment and detector array of this work.

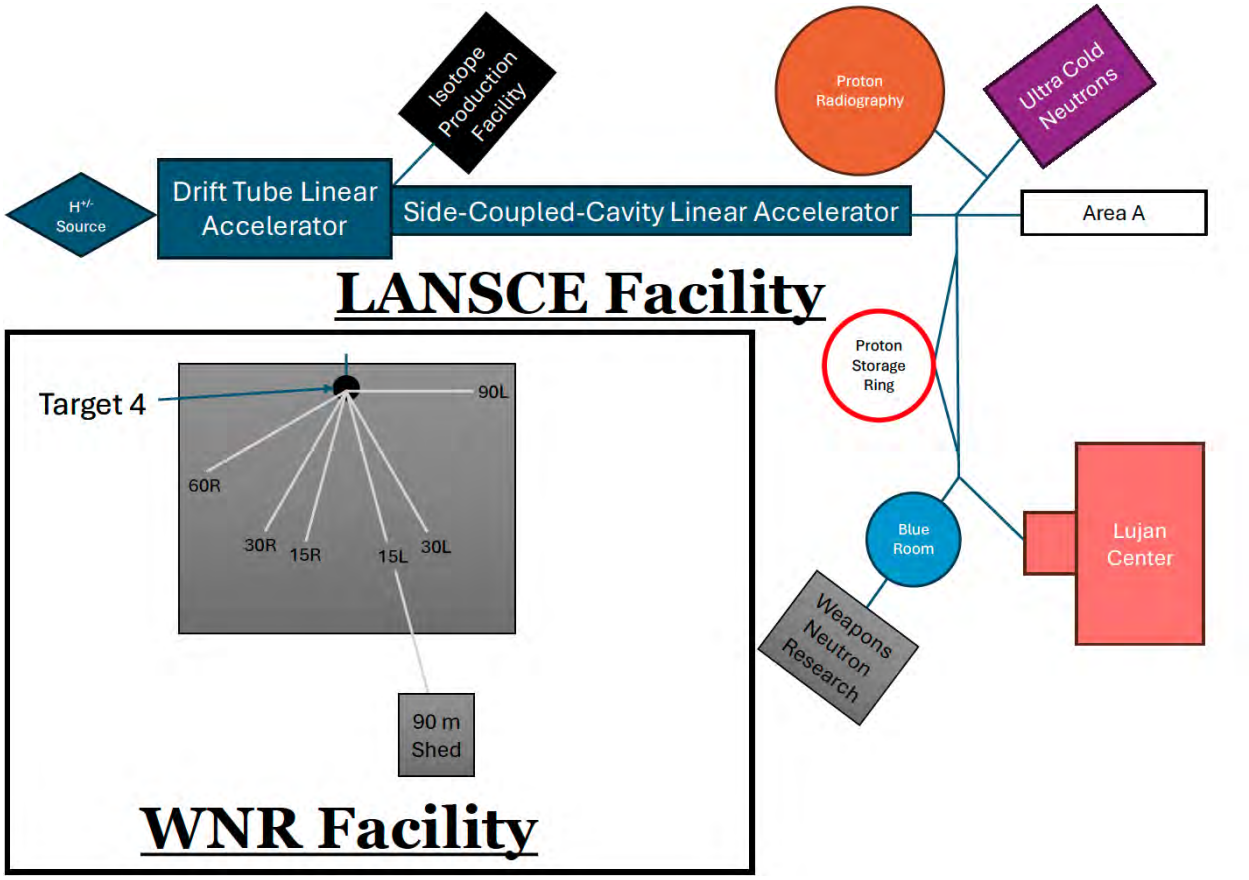

Figure 2.1 A generalized overview of the LANSCE Facility and WNR Facility (rectangular inset). Blue lines are H^- /H^+ beamlines. The beam starts with the hydrogen ion source (blue rhombus) and proceeds through the Drift Tube Linear Accelerator (thicker blue rectangle) and can proceed to IPF. The H^- beam is accelerated down the Side-Coupled-Cavity linear Accelerator (thiner blue rectangle) before proceeding to pRad (orange circle), UCN (violet rectangle), or Area A (white rectangle). The H^- beam can also proceed south towards PSR (red ring), Lujan Center (salmon rectangles), Blue Room, and WNR. The WNR Facility receives the H^+ beam before impinging on Target 4. The 6 flight paths along the neutron beam (gray lines) are labeled with their angular and directional classification. The 90 m shed, located on flight path 15L is also shown and labeled. Buildings/areas, flight paths, and locations are not to scale.

2.2 Weapons Neutron Research (WNR)

The time structure of the WNR proton beam consists of "micropulses" and "macropulses" [47, 48, 49]. A micropulse (collection of protons) of beam is ≈150 ps long. Micropulses are separated by ≈1.8 μs while ≈347 micropulses are grouped together to make a single macropulse. Macropulses are ≈625 μs long with ≈8.3 ms of separation. A diagram of the time structure of the WNR beam is shown in Figure 2.2.

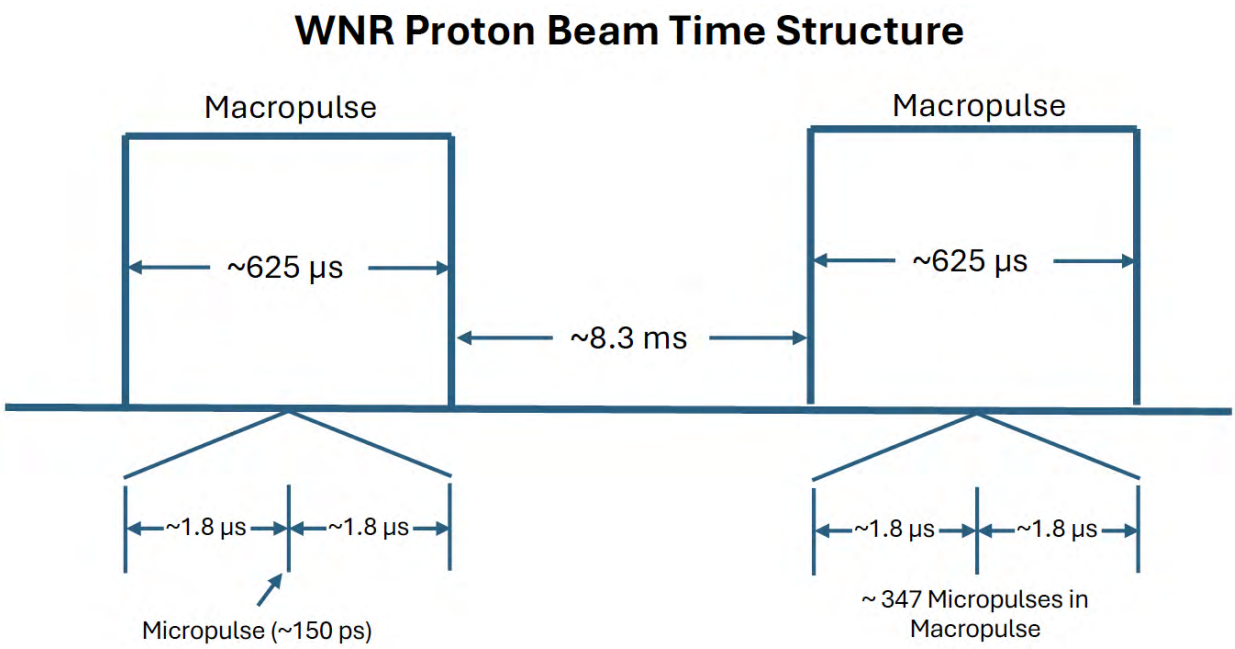

Figure 2.2 The time structure of the proton beam for WNR. Macropulses (the two larger box structures) are composed of approximately 347 micropulses (short ticks in the bottom of the figure). The length of a macropulse is approximately 625 μs while micropulses are approximately 150 ps long. Macropulses are separated by approximately 8.3 ms while micropulses are separated by approximately 1.8 μs from each other.

The WNR Facility produces a neutron white source at Target 4, a tungsten target. The proton beam impinges upon the tungsten target to produce a neutron spectrum, referred to as a "white" source, via spallation. The tungsten target is cylindrical, measuring 3 cm in diameter and 7.5 cm in length and is suspended in a vacuum chamber that is shielded with ports to the flight paths at the WNR Facility [50]. Charged particle fragments that may emerge from the target are magnetically removed.

The energy spectrum of the WNR neutron source changes with flight path angle allowing for experimenters to chose from different neutron flux profiles based on the location of the flight path [51]. The differing flux profiles are shown in Figure 2.3. Neutrons are produced from the WNR tungsten target, also referred to as the "spallation target" or "neutron source". Gamma rays are also emitted as a reaction product and are collectively known as a "gamma flash" and can be used to indicate the start of a micropulse.

The flight paths at WNR are named based on their angle from the incident proton beam

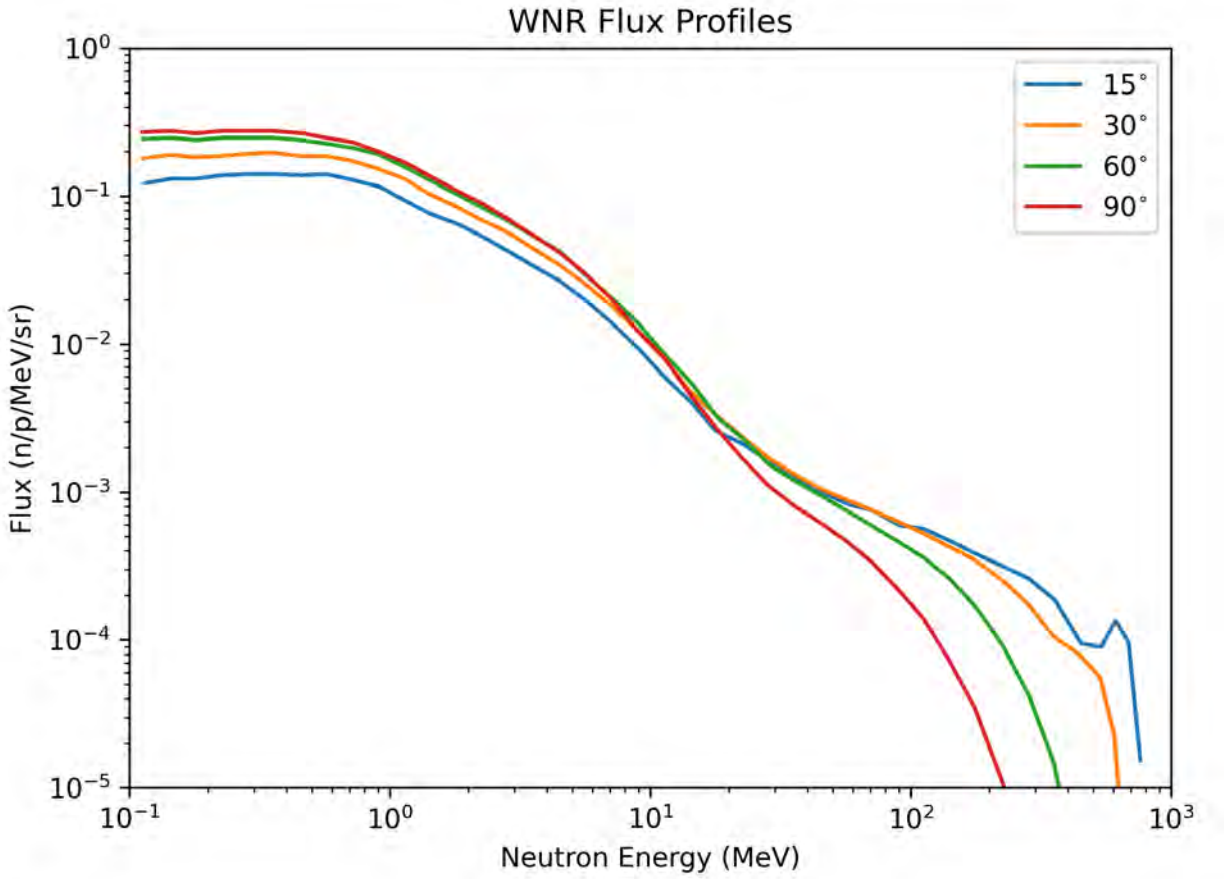

Figure 2.3 A calculation of the different neutron flux profiles from the WNR facility based on the angle of the flight path from the incident proton beam axis. Figure inspired by flux information from Ref. [51].

axis and the spatial direction: left or right of the proton beam axis. For example, 15L refers to 15 degrees, left of the incident proton beam axis. The WNR Facilty consists of 6 flight paths: 60R, 30R, 15R, 15L, 30L, and 90L with the CoGNAC experiment residing on flight path 15L. For more forward focused flight paths, such as flight paths located at 15 degrees, the overall flux profile yields more neutrons at higher energies (200 - 800 MeV range) whereas there are lower neutron yields at lower energies (0.1 - 10 MeV) in comparison to flight paths located at wider angles such as 60 and 90 degrees.

2.3 The Correlated Gamma Neutron Array for sCattering (CoGNAC)

As indicated in the previous section, the CoGNAC setup resides along flight path 15L with the center of the detector array located 21.5 meters from the tungsten spallation target.

The array is made of 54 EJ-309 liquid scintillators [52] in the upper hemisphere and 72 lithium-6 enriched Cs_2LiYCl_6 (CLYC) detectors in the lower hemisphere [53]. The CLYC detectors have vastly superior gamma-ray energy resolution in comparison to the liquid scintillators. The benefit of these liquid scintillators and CLYC detectors is in their ability to discriminate between neutrons and gamma rays, eliminating the need for more specialized detector systems to identify these particles. The neutron elastic cross section presented and discussed in this work comes from the data recorded by the liquid scintillators.

Pulse-shape-discrimination (PSD) is commonly utilized to distinguish between neutron and gamma ray detected events. Figure 2.4 illustrates an examples of such neutron-gamma PSD which is determined by the ratio of the signal tail integral to the total signal integral.

The liquid scintillators are located 1 m from the center of the detector, where the reaction target resides, with an active volume of ≈7 in. in diameter and 2 in. thick. The combined distance from the center of the array to the center of the scintillating material results in a total flight path length of 1.02 m (including the distance of the average interaction depth in

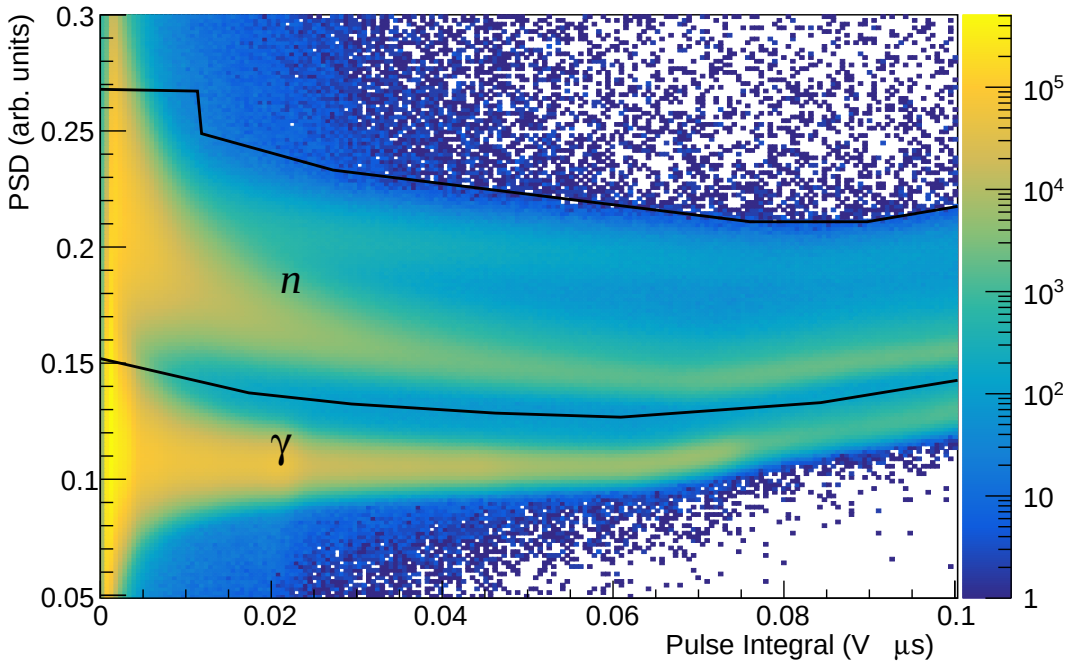

Figure 2.4 An example PSD gate (black) selecting neutron (n) events. The second excluded peak, centered near a PSD value of 0.1, are gamma (γ) detected events.

the liquid scintillator). This results in each detector spanning $\approx \pm 5^{\circ}$ of angular coverage in the lab. Each liquid scintillator is attached to a R4144 Hamamastu PMT (photo-multiplier tube) [54] to amplify the produced scintillation light into a readable signal. The individual detector voltages are set using a CAEN SY4527 High Voltage supply [55]. Signals are then processed by a series of CAEN 1730B waveform digitizers [56] and are then recorded using the MIDAS data acquisition system [57] for analysis.

The liquid scintillators are centered at 9 evenly spaced angles (θ) of 30, 45, 60, 75, 90, 105, 120, 135, and 150 degrees relative to the incident neutron beam direction. This arrangement forms a "rack" of detectors, with a simplified schematic shown in Figure 2.5. Six racks make up the upper hemisphere of the CoGNAC setup located along the azimuthal (φ) angle of $\pm$ 24, $\pm$ 57, and $\pm$ 90 degrees to complete the 54 detector array. The full detector array setup is shown in Figure 2.6.

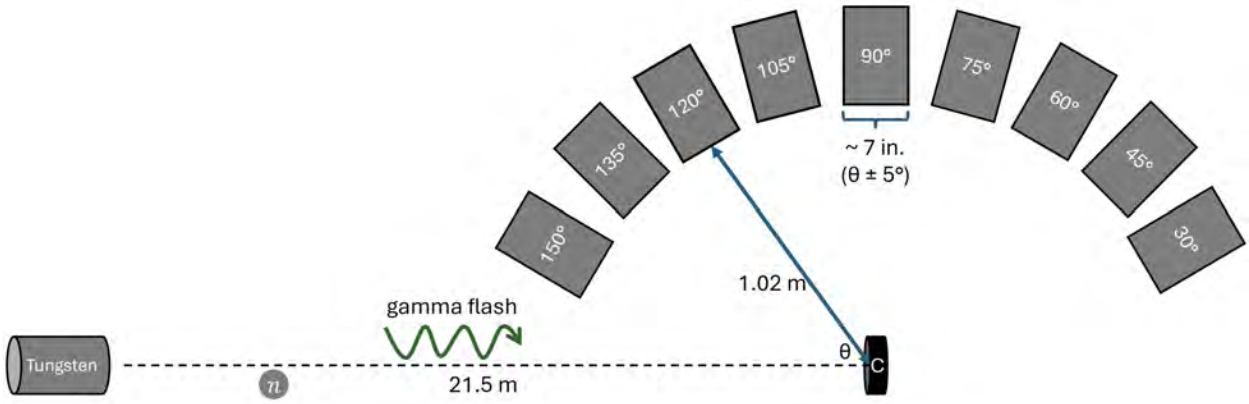

Figure 2.5 A simplified schematic of the CoGNAC setup at the WNR facility along flight path 15L. Going from left to right, spallation neutrons (gray circle labeled n) and the gamma flash (green wavy arrow) are produced and travel 21.5 m to the carbon target (black disk labeled "C"). The carbon target sits in the center of the detector array 1.02 m away from the front face of the liquid scintillator (gray rectangles), each located at one of the 9 different angles θ with respect to the incoming neutron beam axis. Objects are not to scale.

The cylindrical carbon target (reaction/scattering target), made of natural isotopic composition with dimensions 4 cm in diameter and 1 cm thick, is located in the center of the CoGNAC setup and sits at the end of a 4-armed sample changer, resembling that of a pinwheel. The neutron beam, post-collimation specific to the CoGNAC flight path, has a

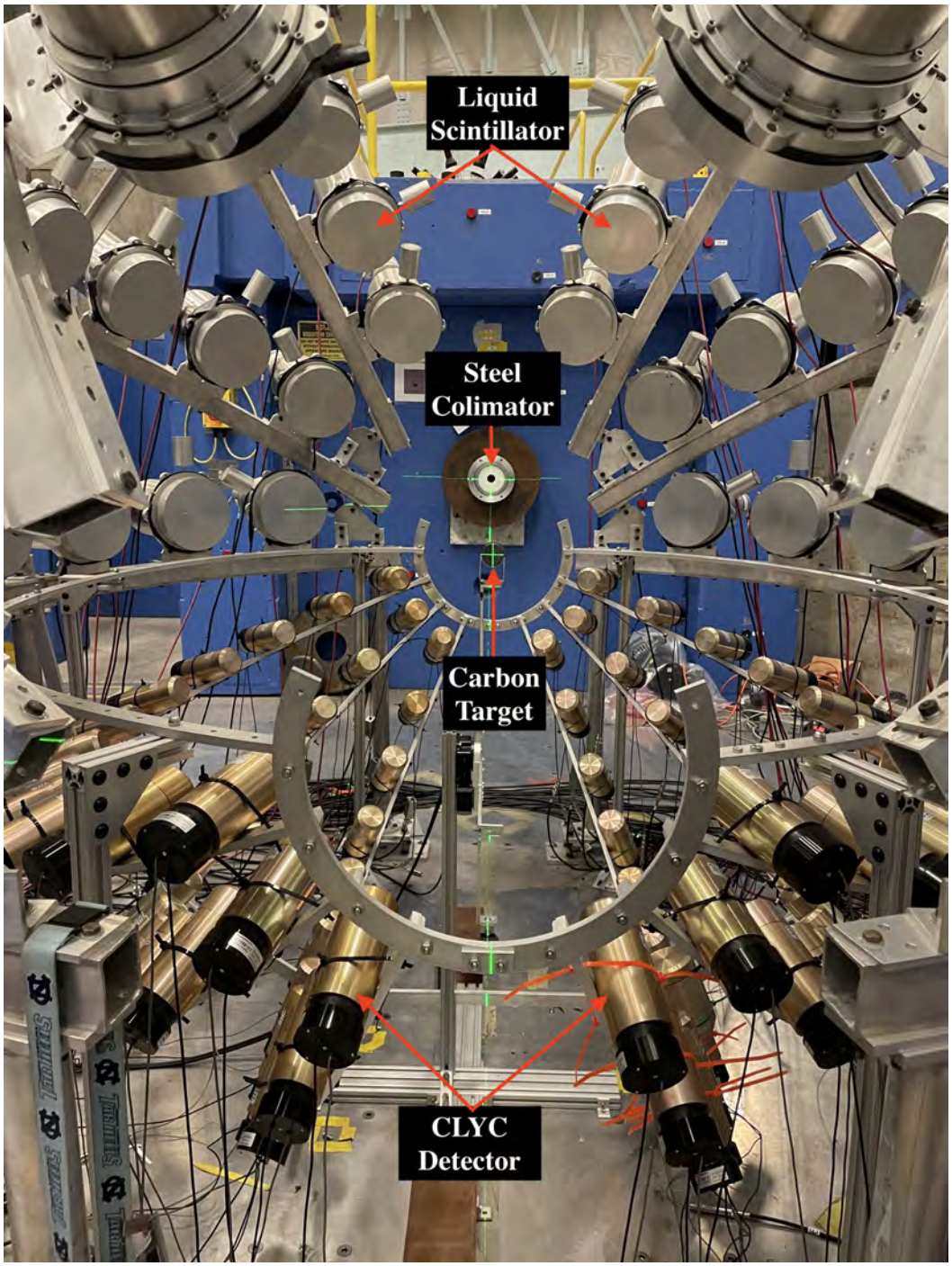

Figure 2.6 The CoNAC setup on flight path 15L at the WNR facility with a carbon target in the center of the detector array. In this image, the beam comes out of the steel collimator (gray circular disk in the center of the image) and reacts with the carbon (small black disk in the center of the array) before neutrons and gamma rays are detected in the liquid scintillators (upper hemisphere) and CLYC detectors (bottom hemisphere). An alignment laser (green) is used to ensure that the reaction target is centrally located along the incoming neutron beam. Figure reused with permission from Keegan Kelly.

measured diameter of 1.65 cm and was therefore within the physical size of the carbon target. The sample changer rotates in 90 degrees increments approximately every 10 minutes. Therefore, each data acquisition "run" lasts ≈10 minutes and allows for natural variation in the neutron beam to be matched when targets are in and out of the beam. The fourth "blank" arm allows for a background measurement to be taken with the CoGNAC setup while allowing the neutron beam to enter a ^{235}U fission chamber to monitor the beam rate and provide a flux for the experiment. The fission chamber is located downstream of the CoGNAC setup, past the detector array.

In an effort to minimize environmental backgrounds and scattered neutrons, the nearest shielding walls surrounding the CoGNAC setup are just over 2 m away from the detector setup. The CoGNAC setup also sits above a 2 m "get-lost" pit (resembling a basement) with the whole detector array supported by a thin floor just above the basement.

As mentioned in Section 2.2, both neutrons and gamma rays arrive at the CoGNAC setup from the spallation target. While the gamma-induced reactions are not measured in the reaction target, the scattering of the gamma flash produced during the spallation reaction will scatter off the reaction target and into the detector array. Given the fact that the gamma rays travel at the speed of light, while the neutrons will have varying energies corresponding to varying velocities and therefore will travel slower than the speed of light, the detection of the scattered gamma flash serves as a reference for the start of each micropulse and are given a time difference value of 0 ns. All neutron energies are then calculated from time-of-flight relative to the gamma flash transit time. The time-difference is calculated as

$$\text{Time-Difference} = t_n - t_\gamma \,, \tag{2.1}$$

where t_n is the neutron time-of-flight as calculated in Equation 1.28 (solving for t) and t_γ is the gamma ray produced from spallation time-of-flight. The total flight path length from the spallation target to a liquid scintillator is the sum of the distance of the flight path length to the center of the CoGNAC array d_{fp} (21.5 m) and the distance from the center of the array, where the scattering target is located, to a liquid scintillator d_d (1.02 m). This total

distance of 22.52 m, along with the measured time difference of the neutrons, allow for the calculation of the incident neutron energy (E_n^{inc}) and emitted neutron energy (E_n^{emit}). The ability to calculate E_n^{inc} and E_n^{emit} from the recorded data is further explained in Chapter 3. Figure 2.7 shows the measured neutrons recorded by a liquid scintillator.

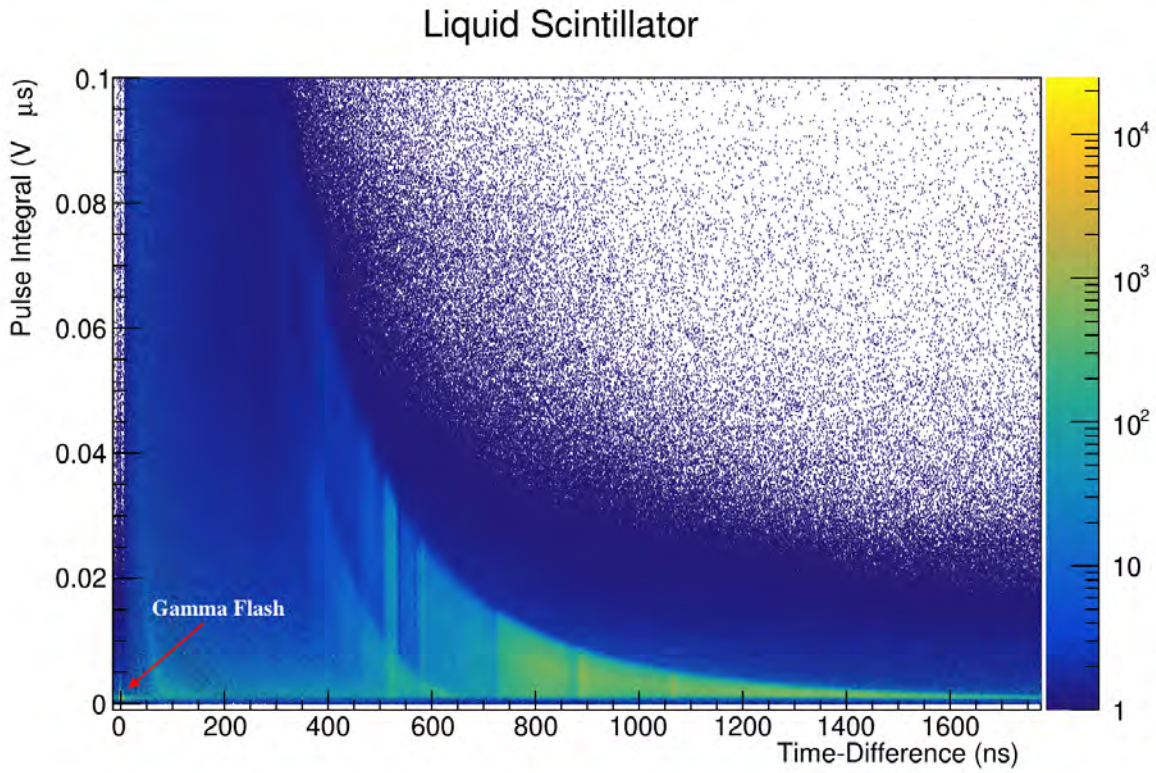

Figure 2.7 A 2D histogram of measured data, from a liquid scintillator, from neutron scattering with a carbon target. Time-difference, as described in Equation 2.1, is on the x-axis and the detector pulse-integral on the y-axis. The gamma flash is located at a time difference value of 0 ns.

The gamma flash (spallation produced gamma rays), as recorded by the detector, are located at the 0 ns mark. The triangular structure that slopes away with increasing time difference are neutron recorded events as seen by a liquid scintillator. The term "pulse-integral" is the total area under the recorded pulse created from a gamma or neutron event. The pulse integral is correlated with the measured energy of a detected particle (gamma-ray or neutron) and a relation between the emitted neutron energy and pulse-integral is developed in Chapter 3.

CHAPTER 3

DATA ANALYSIS

In order to calculate the neutron elastic scattering cross section off carbon, we start with selecting elastically scattered neutron events, converting the elastic events into an energy spectrum, correcting the spectrum for detector efficiency, calculating the differential angular cross section, and lastly, calculating the integrated cross section. Equally important is the uncertainty quantification of each quantity analyzed as well as the respective covariance and correlation matrix for the integrated cross section. The uncertainty quantification, covariance, and correlation matrix of the integrated cross section will be discussed in Chapter 4. Each step will focus on one detector in the whole array with the implication that the same analysis process is applied to the whole detector array unless explicitly stated. Each of these steps will be explained in detail and how the results are used to produce a final integrated cross section, angular differential cross section, and neutron angular distributions. Analysis was done utilizing the CERN ROOT software, version 6.32.06 [58].

3.1 Background Subtraction

One of the first steps in the analysis is removing background events from the carbon foreground data. This is accomplished by taking "blank" data (data where no target is in the neutron beam as explained in Chapter 2, Section 2.3) and subtracting from the data with the carbon target in the neutron beam. An example of measured "blank" data is shown in Figure 3.1 and another of measured carbon data (without background subtraction) is shown in Figure 3.2.

One can already see in the "blank" data that there is structure to the background data that can lead to inaccurate results when analyzing the carbon data if the background is not subtracted out. A scale factor between the carbon data and "blank" data is needed to ensure that the number of events are as close to being equal between the two datasets. A ratio of "t_o" signals, the number of micropulses arriving at the spallation target, between the carbon to"blank" is calculated to be 2.00387 and is used to scale the background before subtraction.

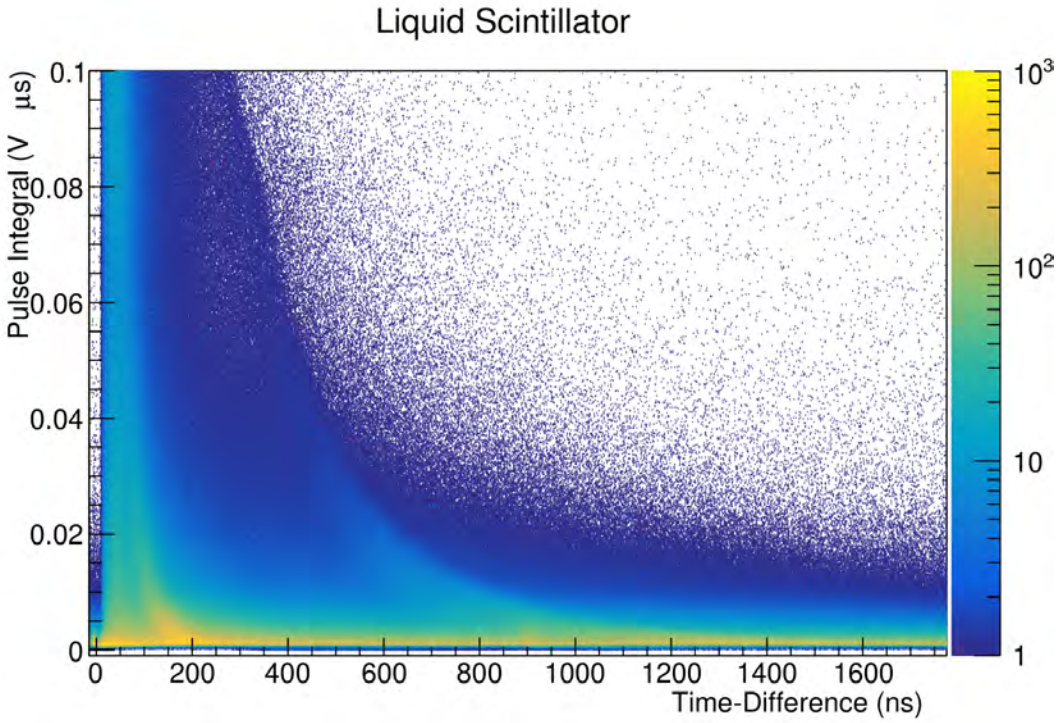

Figure 3.1 A liquid scintillator histogram where no target is in the neutron beam. This functions as a background and gets subtracted from the recorded carbon data.

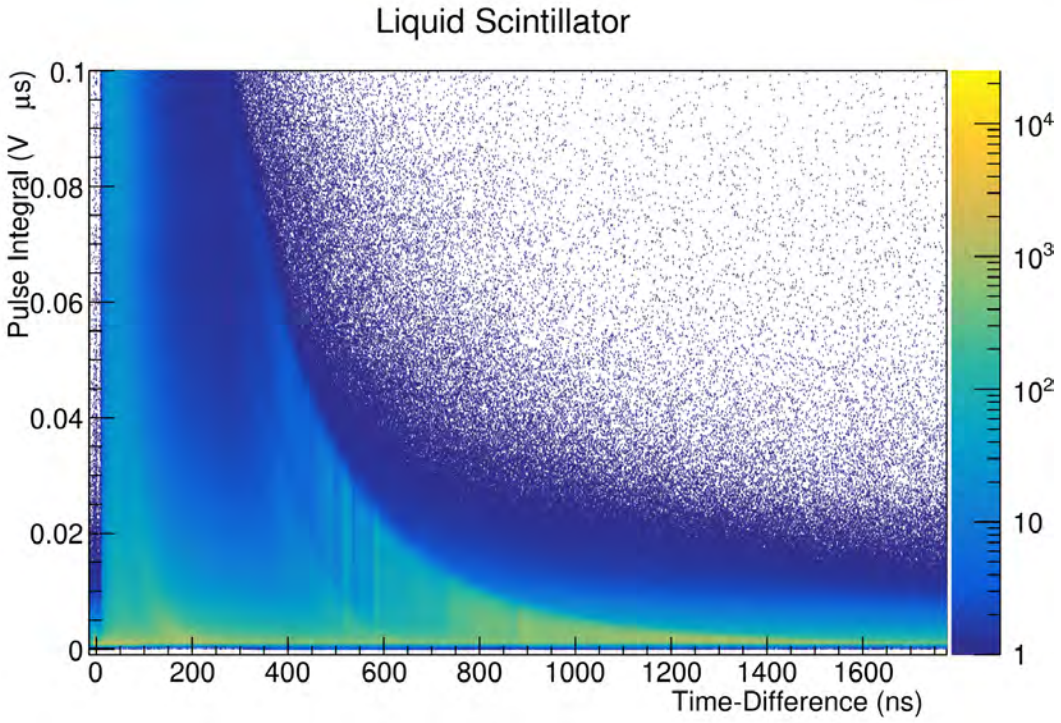

Figure 3.2 A liquid scintillator histogram with a carbon target in the neutron beam that has not been background subtracted.

Figure 3.1 is subtracted from Figure 3.2 to produce a background subtracted histogram that is used in analysis (Figure 3.5).

3.1.1 Gamma Flash Correction

Additionally, the location of the gamma flash as recorded by the detector histograms needs to be corrected. While the definition in Equation 2.1 will equal 0 for a $t_n = t_\gamma$, the gamma flash is not always centrally located at 0 ns for each liquid scintillator histogram as shown in Figure 3.3. Finding the, still small, offset ensures consistency with the definition of using the gamma flash at a time difference value of 0 ns.

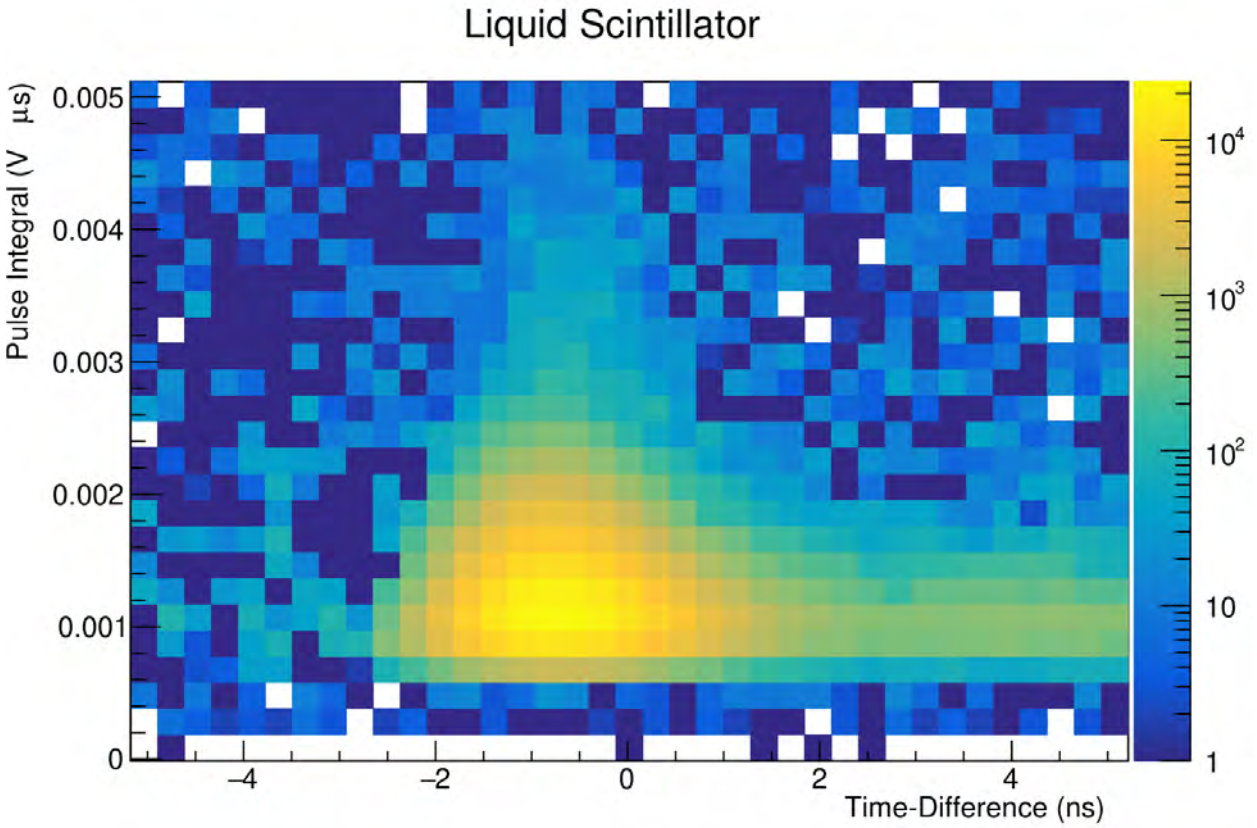

Figure 3.3 The gamma flash (yellow structure) for a liquid scintillator detector where the central location is not centered at 0 ns.

Looking at Figure 3.3, it is noticeable that the gamma flash (the yellow structure) is not centered at 0 ns but rather closer to -1 ns. The time offset is corrected by selecting the gamma flash structure by placing a cut from -1.5 – 0 ns and fitting the resulting x-axis

projection (projecting the counts on to the time axis) and fitting the resulting gamma flash to a Gaussian to obtain the central value from the mean. An example of the gamma flash projection and fit are shown in Figure 3.4.

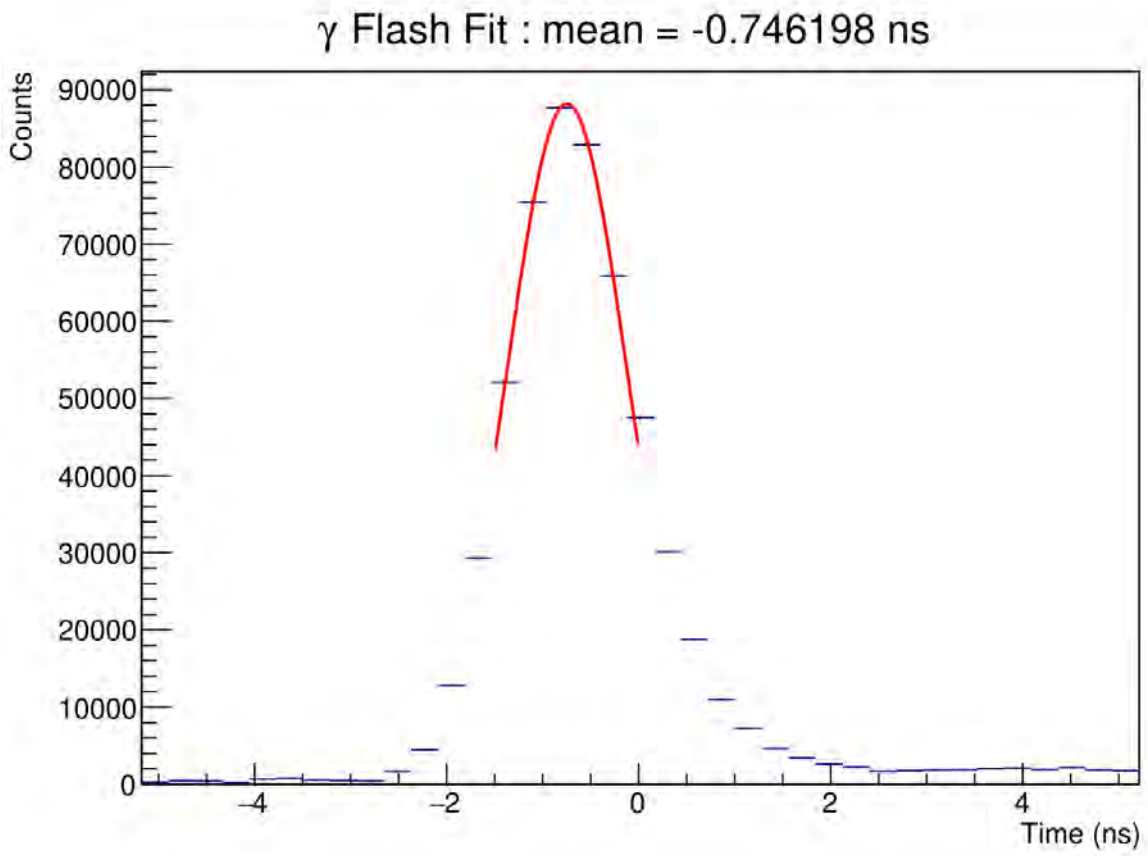

Figure 3.4 The gamma flash data fit with a Gaussian (red) to obtain the mean location for kinematic corrections.

This time offset, while not large, is still noticeable enough to produce incorrect results utilizing the relativistic kinematics discussed in Chapter 1, Section 1.5. For example, normally a 2 MeV incident neutron would have a time difference of ≈1085.0253 ns for a detector at 120°. With the gamma flash being off ≈0.7481 ns, This corresponds to a E_n^{inc} energy value of 2.00258 MeV (2.58 keV increase) which is within the resolution of the liquid scintillators. This offset only gets amplified at higher incident neutron energies. For example, at E_n^{inc} = 6.5 MeV at 120° corresponds to a time difference of ≈570.6996 ns normally, but with ≈ 0.7461 ns offset the E_n^{inc} = 6.5152 MeV (15.2 keV increase).

The time offset obtained from the fit is subtracted from the theoretical time difference calculated by Equation 2.1. This is done because a negative time offset, as is the case for all the liquid scintillators in the carbon data set, will correct the gamma flash to be centered at 0 ns. Similarly, if the time offset is positive, subtraction by a positive time offset will relocate the gamma flash to be centered at 0 ns.

3.2 Elastic Event Selection

In order to extract a neutron elastic scattering cross section, identification of elastically scattered neutrons is required. The starting point for analyzing the detector data is identifying the major features in the data corresponding to each state in ^{12}C. The choice to use ^{12}C is motivated by the fact that the natural composition of carbon is 98.84 – 99.04 % [31] ^{12}C. The major features in the recorded data are identified visually with explicit markings and is shown in Figure 3.5.

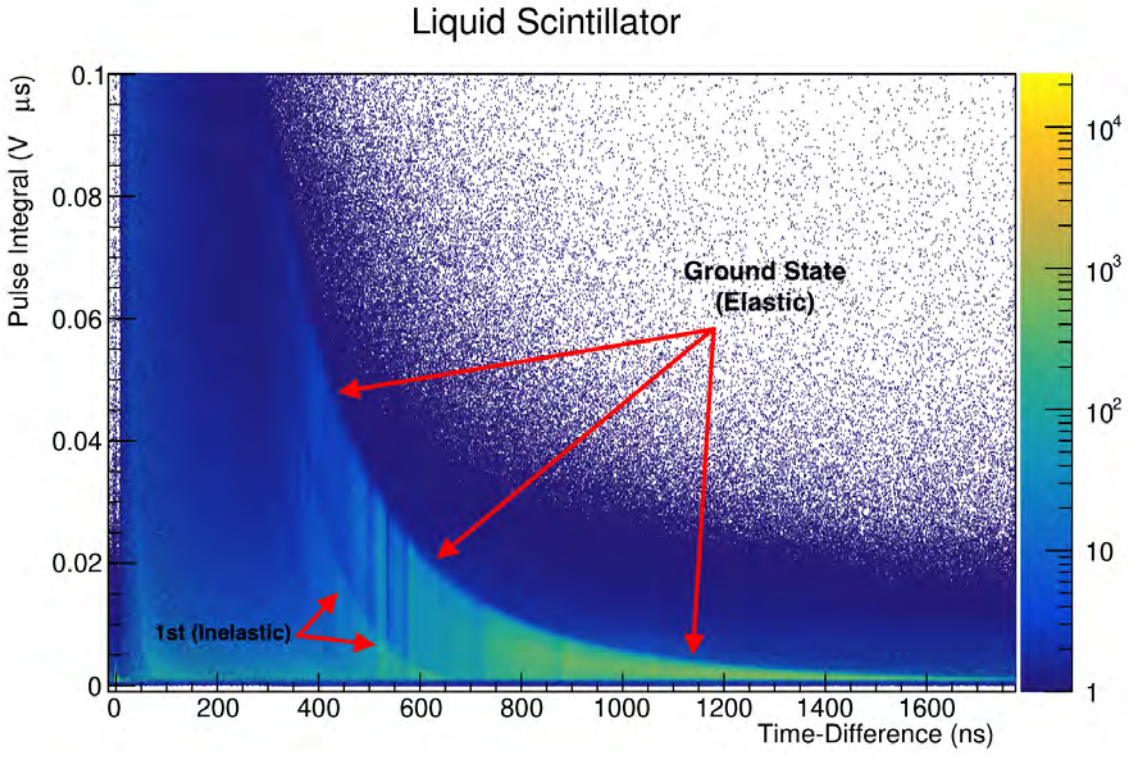

Figure 3.5 The 2D histogram data from a carbon target (same a Figure 2.7). The two clearly visible states of ^{12}C are labeled: "Ground State" which are elastically scattered events and "1st" which corresponds to the first excited state of ^{12}C and are inelastically scattered neutrons.

Looking from right to left in Figure 3.5, the major features are neutrons scattering from the ground state, which are the elastically scattered neutrons from reactions with ^{12}C, and the band labeled "1st (Inelastic)" is the ^{12}C(n,n') reaction populating the first excited state. The task is to isolate the elastically scattered neutrons and ideally, only those that reside at higher pulse-integrals as they correspond to detected neutrons that satisfy the kinematic conditions, as previously derived, for elastic scattering and have not scattered from the environment prior to detection. This also minimizes selection of events from cross talk between detectors. This suggests that a thin cut centered on the "ledge" of elastic events (the region where, moving from high pulse integrals to low pulse integrals, for a given time difference the counts dramatically increase) ensures selection of "purely" elastically scattered events and minimizes any further possible environmentally scattered neutrons.

It is important to remember that while the time that is recorded on the x axis of Figure 3.5 is the time difference (containing time information of both E_n^{inc} and E_n^{emit}), the detector measures the emitted neutron energy E_n^{emit}. It is therefore necessary to build a relationship between neutron time difference to E_n^{inc}, then E_n^{inc} to E_n^{emit}, E_n^{emit} to pulse integral, and lastly E_n^{emit} to time difference. This process allows for a graphical cut to be applied on the the detector (data) histogram and select only elastically scattered neutrons. For developing each of the aforementioned relationships, E_n^{inc} values from 0.5 – 20 MeV were sampled in 1 keV (0.001 MeV) intervals.

Establishing a relationship between the E_n^{inc} and E_n^{emit} is done utilizing the kinematic equations in Chapter 1, Section 1.5 and is shown in Figure 3.6. Note that for each detector angle, more forward focused detectors, such as 30 (gray) and 45 (purple) degrees, have neutron emitted energies closer to the incident beam energy in comparison to more backward scattered angles such as 150 (black) and 135 (red) degrees.

For converting the neutron emitted energy E_n^{emit} to a pulse integral, this is accomplished phenomenologically by applying scale factors to the emitted neutron values and the measured

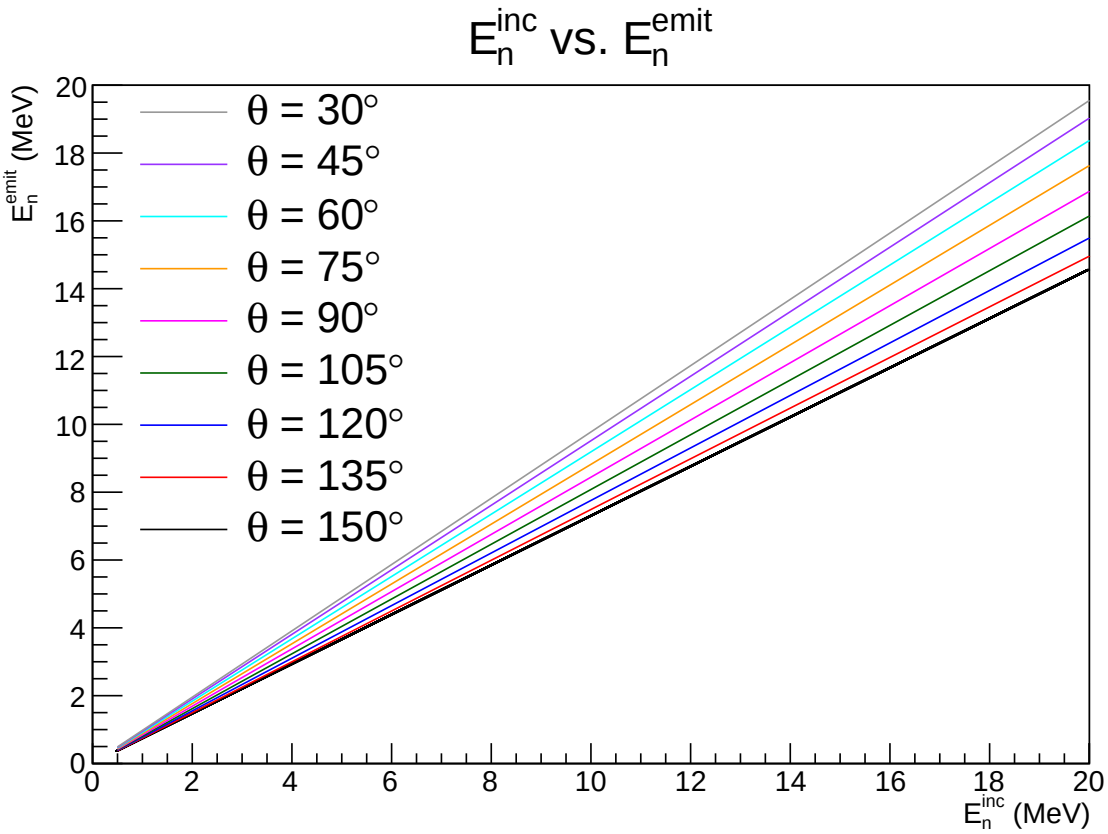

Figure 3.6 The relationship between neutron incident energy E_n^{inc} and neutron emitted energy E_n^{emit} at different emitted angles. Angles are the central angle of each detector.

time difference. The equation used to convert E_n^{emit} into a pulse integral is

$$\text{Pulse Integral (PI)} = 0.95 * \left[\frac{E_n^{emit}}{275} + 0.375e^{-(\text{time-difference})*0.13} - 0.001\right] . \qquad (3.1)$$

The form of Equation 3.1 is motivated by the fact that the elastic events in Figure 3.5 are in the form of a decaying exponential and the division of E_n^{emit} by a scale factor is done to reduce the calculated values onto the range of pulse integral values of the liquid scintillator (0 – 0.1). All other scale factors were found through an iterative process with the intent of making Equation 3.1 best resemble the trend of the elastically scattered neutrons. The relation between E_n^{emit} and pulse integral is shown in Figure 3.7.

This conversion gets applied to every detector as each detector is a liquid scintillator operating in the same manner. A relationship between neutron time difference can be established based on the incident neutron energy. Equation 3.1 is used for each detector allowing

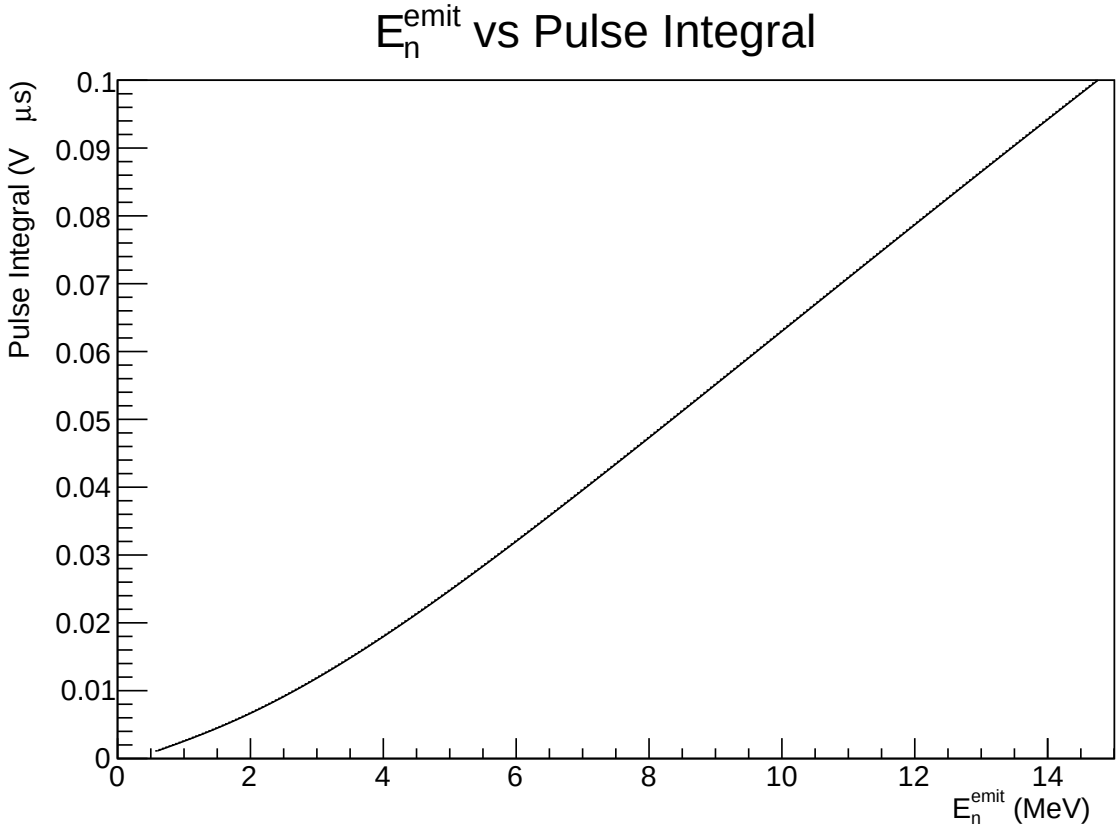

Figure 3.7 The conversion of neutron emitted energy E_n^{emit} to pulse integral utilizing Equation 3.1.

for each detector to get an individualized "kinematic curve" based on the underlying scattering kinematics covered in Chapter 1, Section 1.5. An example of a kinematic curve placed onto a detector is shown in Figure 3.8.

The purpose of the kinematic curve is to visually show on the detector histogram where the "true" elastically scatter neutrons should reside and is motivated by the natural curve as represented by the data. The next step is defining the boundaries around the kinematic curve with the intention of a having a thin selection to ensure selection of "pure" elastic scattered neutrons. In order to describe an appropriate thickness that is needed for selecting the desired neutron elastically scattered events, a resolution function shown in Equation 3.2 and described in Ref. [59] as used for an EJ-309 liquid scintillator [60] and EJ-315 scintillator [61], is used to provide the 1σ value of the liquid scintillator as a function of the detected

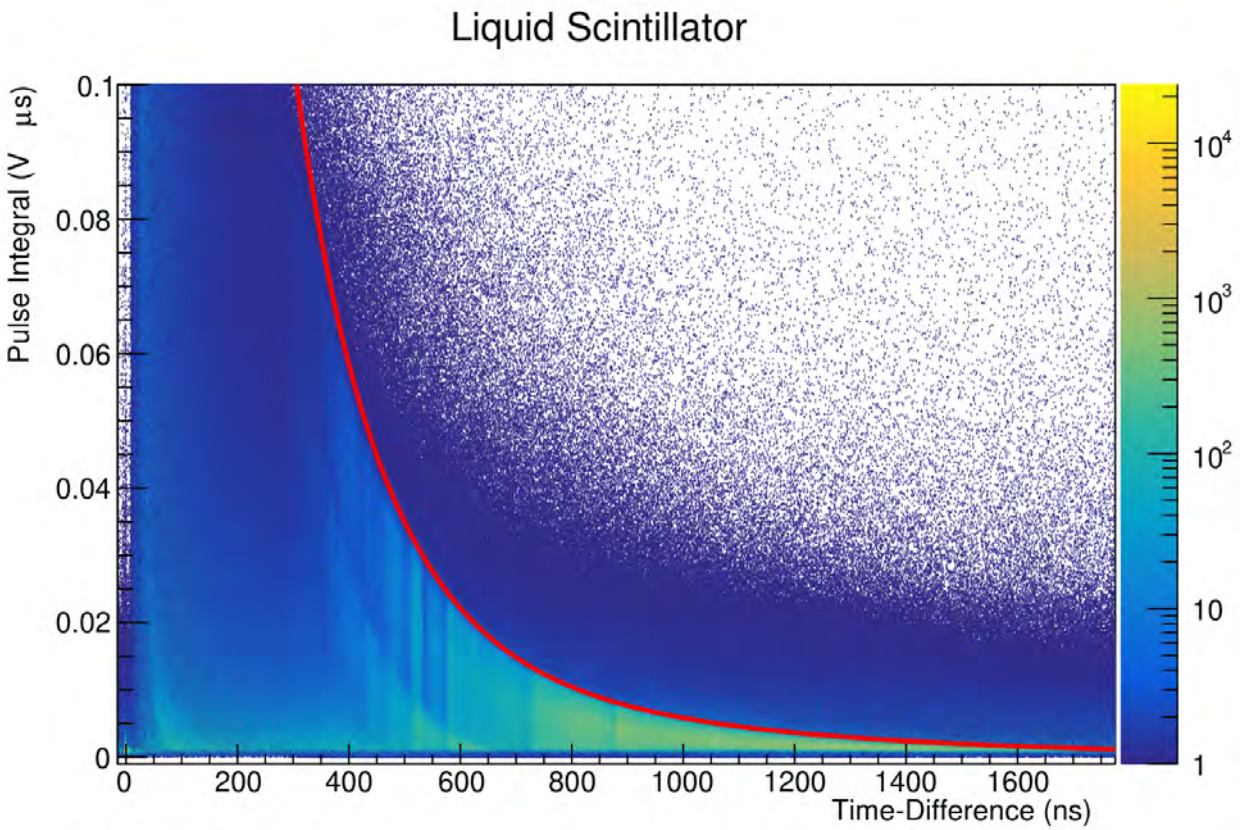

Figure 3.8 The kinematic curve (red) shown on the liquid scintillator histogram using Equation 3.1 to describe how elastically scattered neutrons are detected in a liquid scintillator.

neutron energy (E_n^{emit})

$$\sigma = \frac{\sqrt{a^2x^2 + \beta^2 x + \gamma^2}}{2\sqrt{2\ln 2}}, \tag{3.2}$$

where α, β, and γ are user defined constants that are adjusted to change the thickness of the cut across varying energies (pulse-integrals), x. The values used in this work are summarized in Table 3.1

Parameter	Value
α	0.10
β	0.03
γ	0.00

Table 3.1 The resolution equation (Equation 3.2) parameters that are used to generate the cut to select neutron elastically scattered events as seen in Figure 3.8.

The values in Table 3.1 were found through an interactive process to ensure that elastically scattered neutrons were selected while avoiding inelastically scattered neutrons (labeled

1st excited state in Figure 3.5). Additionally, the value of the parameters were further refined to the reported values based on ensuring the calculated integrated cross section (see Chapter 5) agreed with the "standard region" (refer to Chapter 1, Section 1.3) trend [27].

The resulting 1σ values provided the upper and lower bounds to the cut. The bounds are found by taking the results of Equation 3.1 and Equation 3.2 and are calculated as

$$\text{Upper \& Lower Bounds} = PI \pm \sigma\,. \tag{3.3}$$

Finally, a cut can be generated on the liquid scintillator histogram data that selects on elastically scattered neutrons. The cut on the desired data is shown in Figure 3.9.

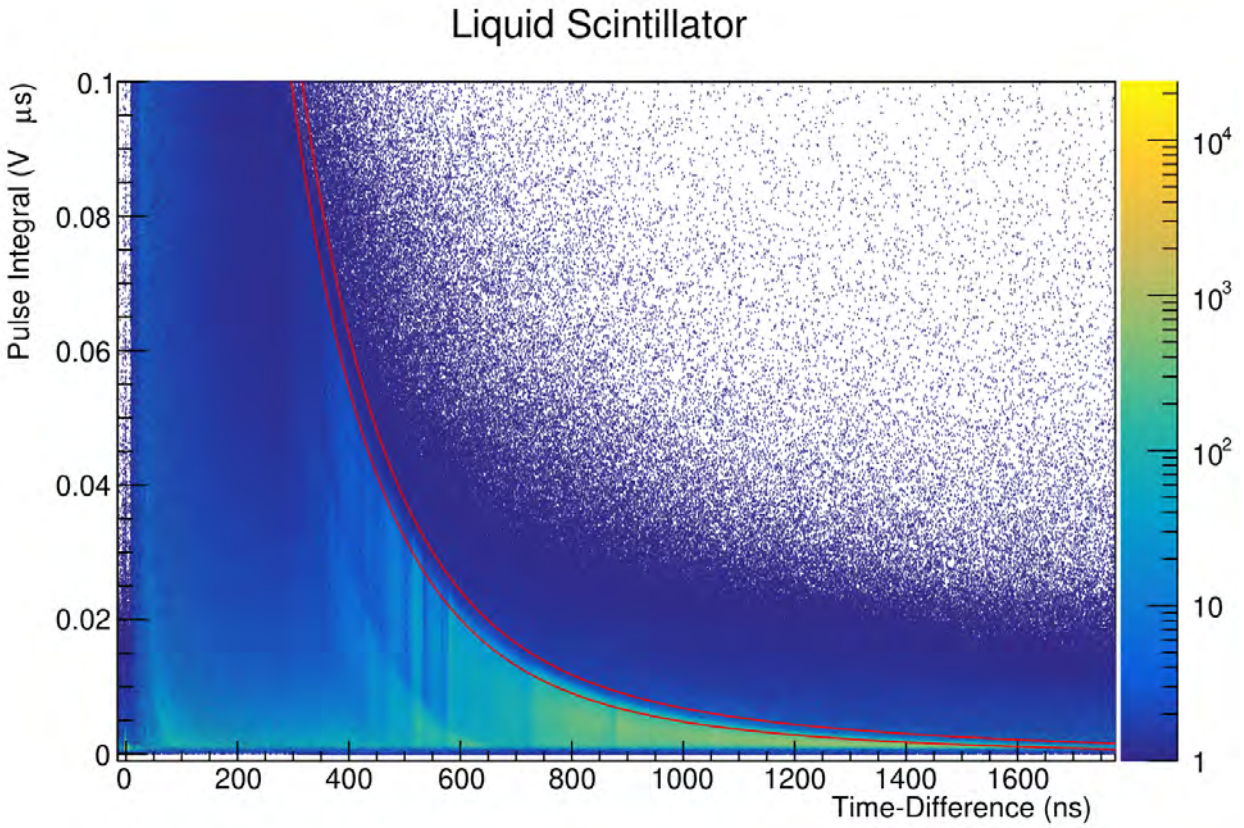

Figure 3.9 The liquid scintillator histogram with the desired cut (red) applied to the data that selects elastically scattered neutrons.

This cut is then applied to the detector histogram to produce a time spectrum that is converted into an energy spectrum using the relativistic scattering kinematics equations discussed in Chapter 1, Section 1.5.

3.2.1 Cut Algorithm

The boundaries of the cut described in Section 3.2 are physically motivated based on the nature of the detector, how elastically scattered neutrons behave due to relativistic kinematics, and utilize an established definition to produce the boundaries of the cut given by Equation 3.2. The default method in ROOT locates the bin center of each bin and checks if a bin, via the location of the bin center, is within the boundaries of the defined cut. If the bin center is within the boundaries of the cut, the entire bin contents (counts) are included, and if the bin center is outside of the boundaries of the cut then the entirety of the bin is excluded from the selection [62]. The portion of a bin the cut intersects is a valid region and does not necessitate "throwing away" entire bins if the bin center is not within the confines of the cut and similarly, portions of the bin that is excluded from the cut. The default algorithm in ROOT, if utilized as it currently exists, produces unphysical results.

In order to recover bins of counts that are intersecting with the cut boundaries, a more ideal scenario is to find the percentage of the bin that is included in the cut and multiply this factor by the number of counts in a bin. The 10 different scenarios that one has to account for are demonstrated in Figure 3.10. In order to determine which scenario a given bin is classified as, each of the 4 corners of the bins are compared to the location of cut. In particular, the lower and upper bin edges are obtained on the x and y axis. The cut is then evaluated at the x lower and upper x-axis bin edges to obtain the cut y coordinates and are compared to the y lower and upper y-axis bin edges.

The two trivial cases are when the cut excludes the entirety of the bin and includes the entire bin. In this case, no special handling is required and the default ROOT cut process is allowed to proceed. For bins that are intersected by the cut, the shaded region (see Figure 3.10) is broken into two sections: a rectangular region and triangle/trapezoid, depending on the cut type scenario type. The rectangular section excludes the cut boundary is calculated using the area of a rectangle ($l * w$) and the triangular/trapezoid region, which contains the cut boundary, approximates the cut as a linear function given the small size of the bins when

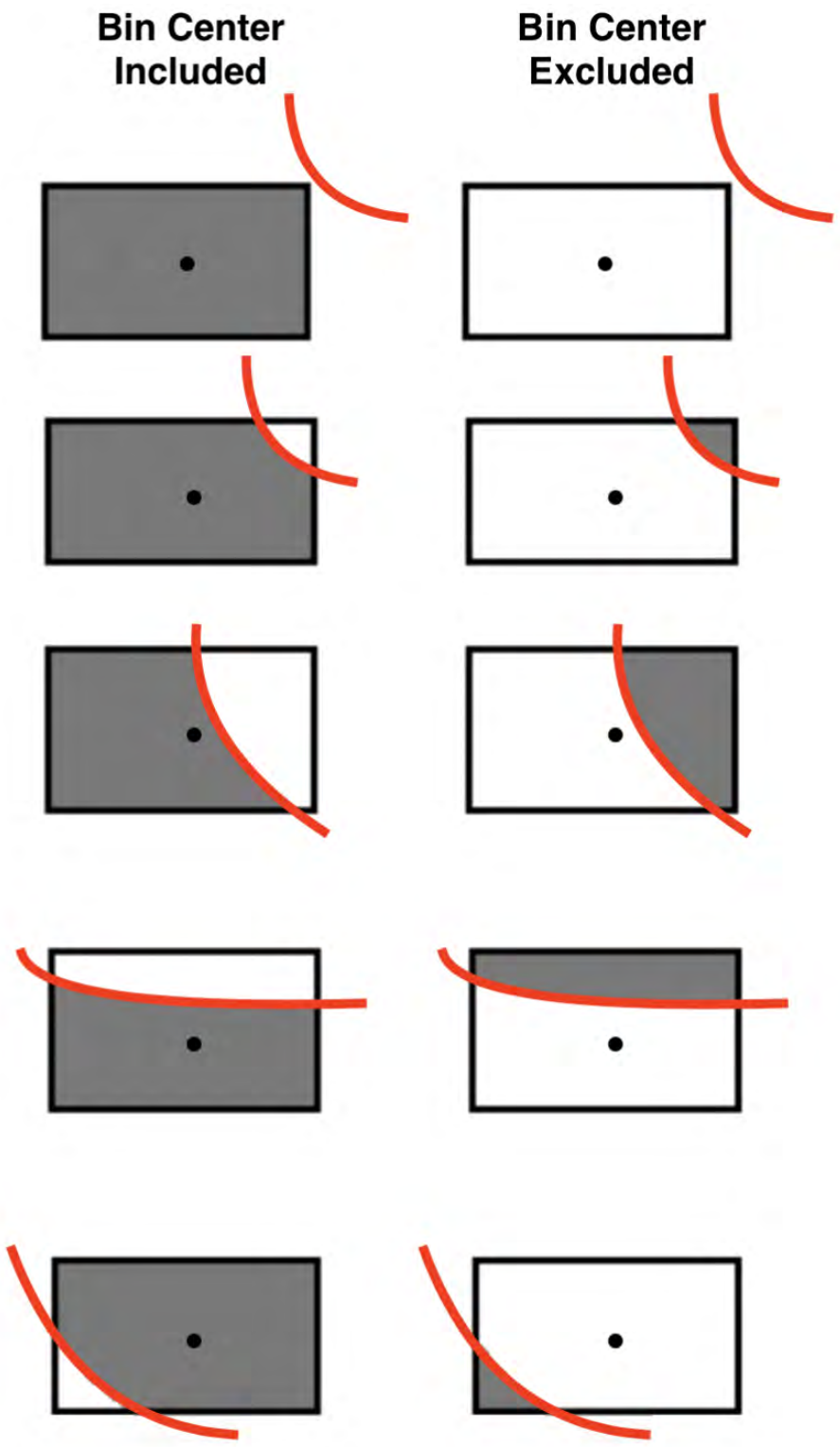

Figure 3.10 The different scenarios of how the cut (red) overlays on bins (black rectangles) with respect to the location of the bin center (black dots). Shaded regions are regions of the bin that are included in the cut and are calculated using the cutting algorithm.

applied to the data and is calculated using the triangle/trapezoid area ($\frac{1}{2}bh$ or $\frac{1}{2}[b_1 + b_2]h$, respectively) formula to calculate the area of the bin that is included in the cut. The two areas (rectangular + triangular/trapezoidal) are then summed to together and divided by the total bin area to get a percentage of the bin that is included in the cut. This percentage is then multiplied by the total counts within the bin. This assumes uniform count distribution within each bin, justified from bin definitions.

A secondary 2D histogram is produced using the explained cutting algorithm to account for more accurate event selection before the production of an energy spectrum. A liquid scintillator histogram that has a cut applied is shown in Figure 3.11. The post-cut histogram is ready to be converted into an energy spectrum.

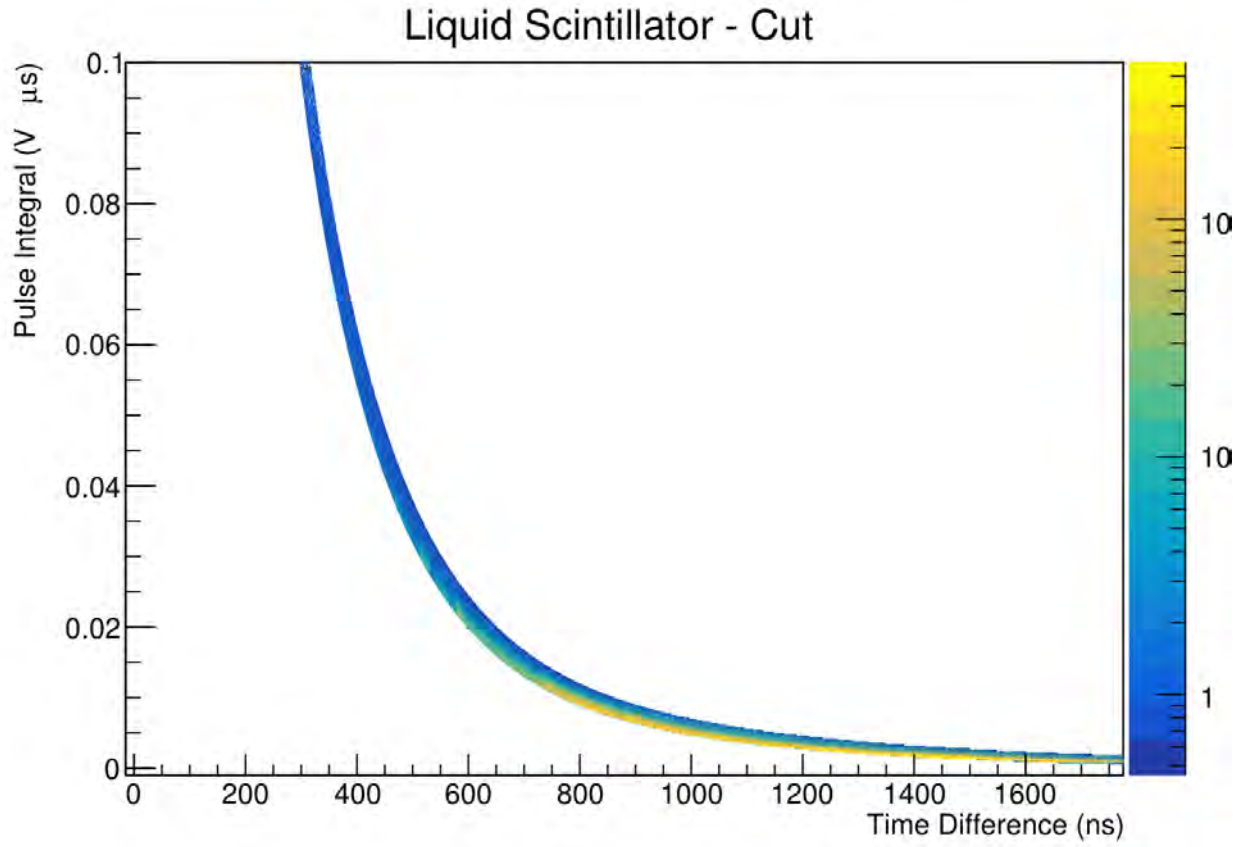

Figure 3.11 The liquid scintillator histogram, as seen in Figure 3.9, with the cut applied to the histogram using the describe cutting algorithm.

3.3 Energy Spectra

Using the liquid scintillator histogram with elastically scattered neutrons selected, as shown in Figure 3.11, it is possible to now create an energy spectrum. This is accomplished by taking the selected events and projecting onto the time axis (x axis) to produce a counts vs. time histogram. This is easily accomplished in ROOT with the `ProjectionX()` command that takes a 2D histogram and projects the histogram onto the x axis to make a 1D histogram. Utilizing the aforementioned command produces a time spectrum as show in Figure 3.12.

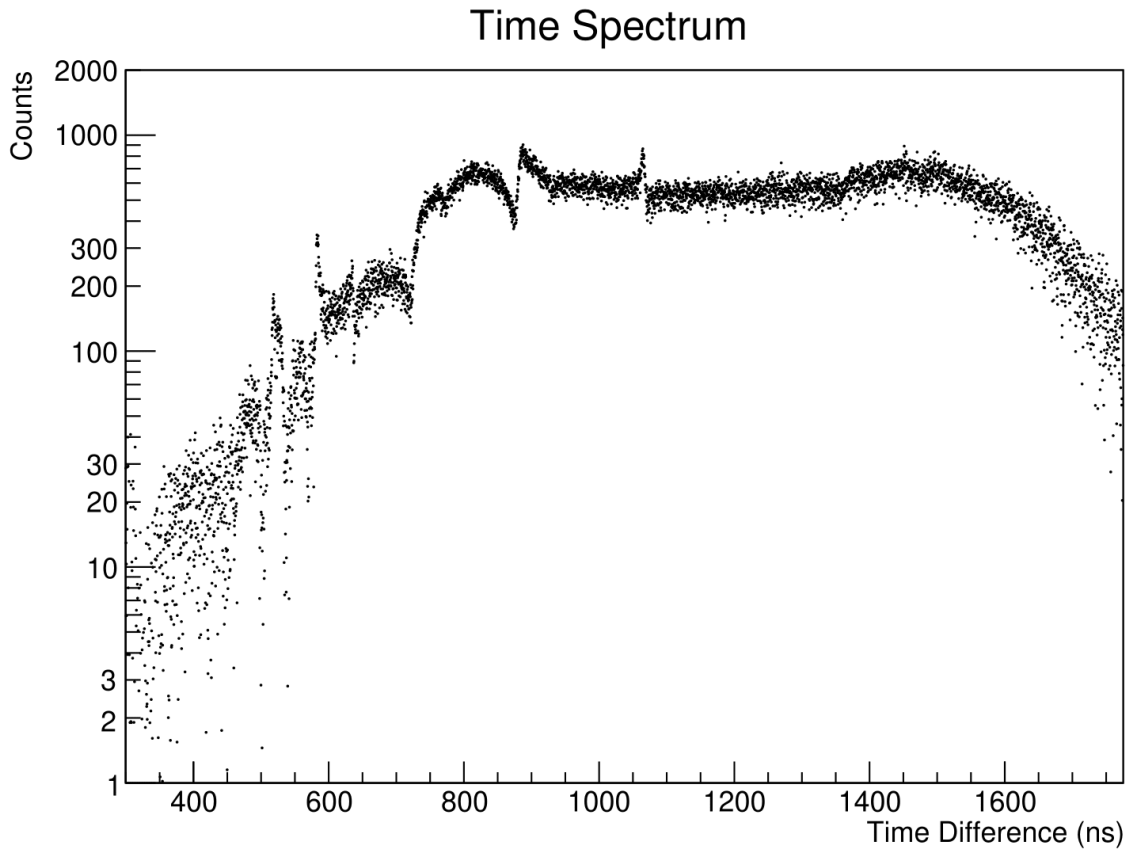

Figure 3.12 The selected elastic scattered neutron events as shown in Figure 3.11 projected onto the time axis to create a spectra of neutron counts as a function of time difference (ns). The black dots are the recorded counts.

As seen in Figure 3.12, some structure in the time spectra can already be seen from selecting elastic scattered neutrons. To turn the time spectrum into an energy spectrum for efficiency correction, the relativistic scattering kinematics in Chapter 1, Section 1.5 are

utilized to establish a relationship between time difference and E_n^{inc}.

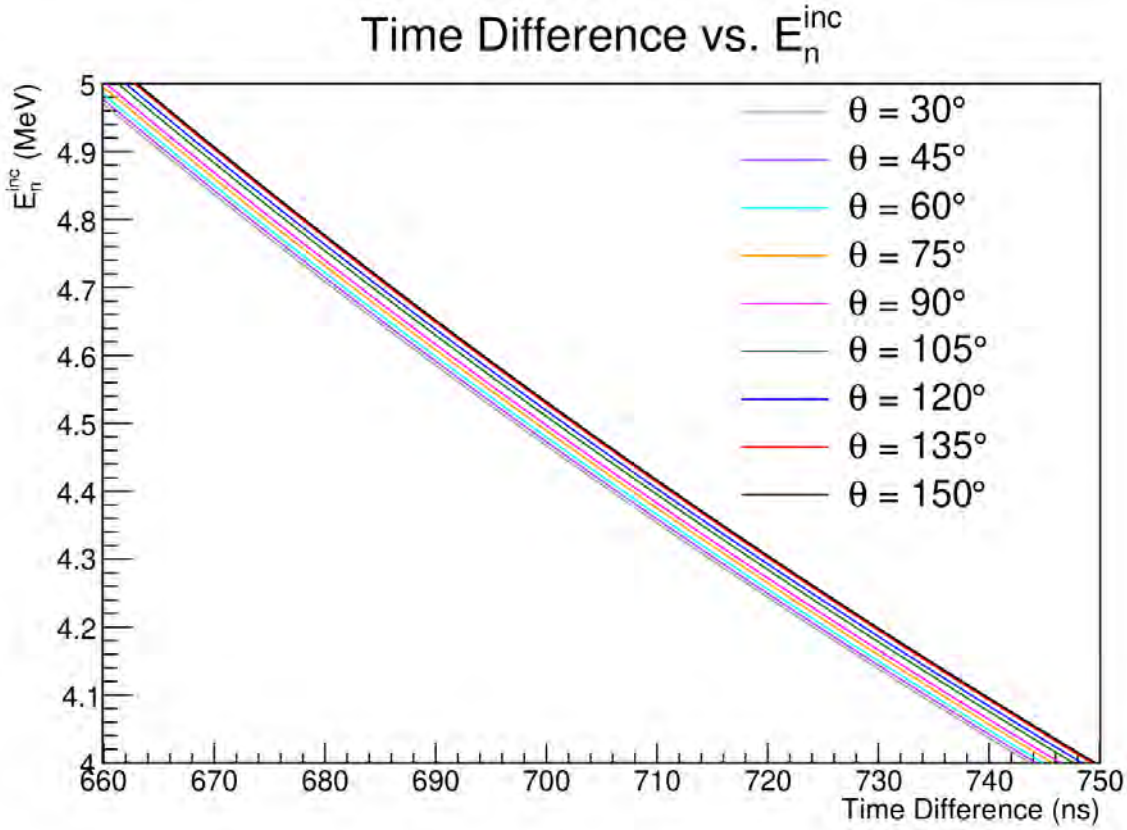

Figure 3.13 The kinematic relation between time difference (ns) to incident neutron energy E_n^{inc} (MeV) over different lab detected angles, θ. A zoomed in subset of the full time-difference region is shown see the differences of E_n^{inc} for a given time difference across different detector angles more clearly.

The conversion from time difference to incident neutron energy as shown in Figure 3.13 is used on the time spectrum (Figure 3.12), accounting for the appropriate detector angle, to produce an energy spectrum. In the process to produce an energy spectrum, the bin center of the time spectra is used and bin edges of the time spectrum is converted to E_n^{inc}, to produce the respective data point, and corresponding upper and lower uncertainty on the E_n^{inc} value. Additionally, given that a bin is an integration over constant time intervals corresponding to variable energy intervals, the counts are divided by the bin width. This effectively divides out the time integration and ensures that comparison of spectra (energy, cross section, etc.) is consistent between datasets and literature values as will be the case for

efficiency calculation and correction. This is also consistent with the theoretical motivation given in Chapter 1, Section 1.1. The resulting conversion, with uncertainties, is shown in Figure 3.14.

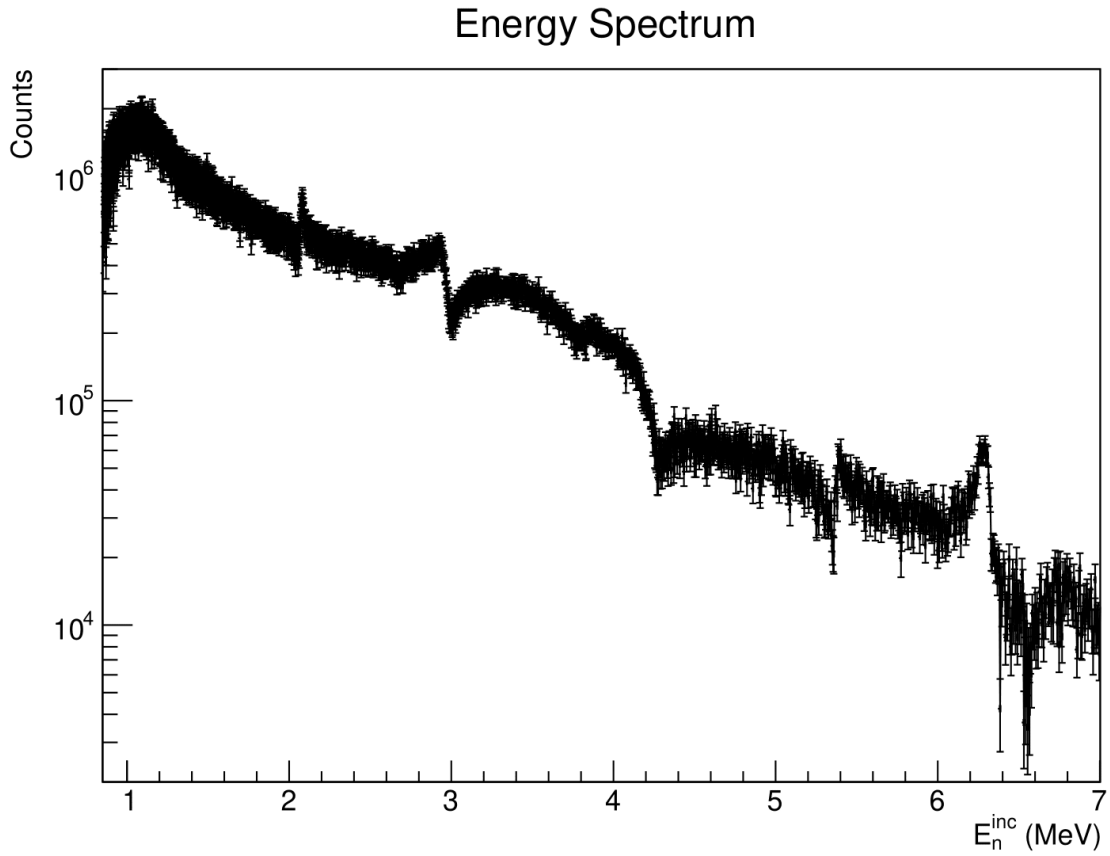

Figure 3.14 The energy spectrum produced using the kinematic relation between time difference and neutron incident energy E_n^{inc}.

The energy range that is displayed in Figure 3.14 is 0.85 – 7 MeV. The lower limit of 0.85 MeV is primarily driven by low counting statistics in the production of a detector efficiency as described in Section 3.4 and the arrival of the next micropulse (where lower energy neutrons would be overlapped with high energy neutrons from the next arriving pulse). The upper limit of 7 MeV is determined as a cutoff due to the decrease in measured neutron counts starting at 7 MeV from prompt fission neutron spectrum from ^{252}Cf and subsequently efficiency, as discussed in Section 3.4. As was the case with Figure 3.12, structures of interest begin to appear within the energy spectra as these structures will become notable features

in the integrated cross section.

3.4 Efficiency Correction

In reality, a detector is not able to measure every neutron that is incident upon the detector, resulting in an unwanted shape effect on the measured energy spectrum. To correct for this effect the detector efficiency (ε), defined as the relative probability for detecting a neutron at a given energy, is derived. This detector efficiency, which is energy dependent, is then applied to the measured carbon spectrum shown in Figure 3.14. The reference spectrum comes from the prompt fission neutron spectrum (PFNS) from the spontaneous fission of ^{252}Cf, which is considered a neutron data standard [27].

3.4.1 Efficiency Calculation

The calculation of the liquid scintillator detector efficiency begins with obtaining the ^{252}Cf PFNS and uncertainties from the IAEA (International Atomic Energy Agency) Neutron Data Standards [63]. The reference data are based upon the Mannhart evaluations [64, 65], plotted in Figure 3.15.

The range of energies for which the ^{252}Cf PFNS is considered a standard is 10 eV – 30 MeV. For the incident neutron energy range mentioned in Section 3.3, the smallest neutron energy occurs at $E_n^{emit} \approx 0.62$ MeV for $E_n^{inc} = 0.85$ MeV and a maximum $E_n^{emit} \approx 6.85$ MeV for $E_n^{inc} = 7$ MeV. The range of E_n^{emit} values, for the E_n^{inc} range used in this work, is well within the bounds over which the ^{252}Cf PFNS is considered a standard.

A ^{252}Cf source was placed in the center of the CoGNAC array and data were recorded measuring the prompt gamma rays and neutrons from the spontaneous fission source. By measuring the PFNS, this is similar to measuring the E_n^{emit} values in the carbon scattering setup. This allows for a relation between the two dataset to be developed through the translation of the cut, developed in Section 3.2, via scattering kinematics (Chapter 1, Section 1.5) to be applied onto the ^{252}Cf dataset.

Similar to the carbon dataset, the prompt gamma rays are centered at a time difference value of 0 ns and the subsequent neutrons are recorded. A correction for the prompt gamma

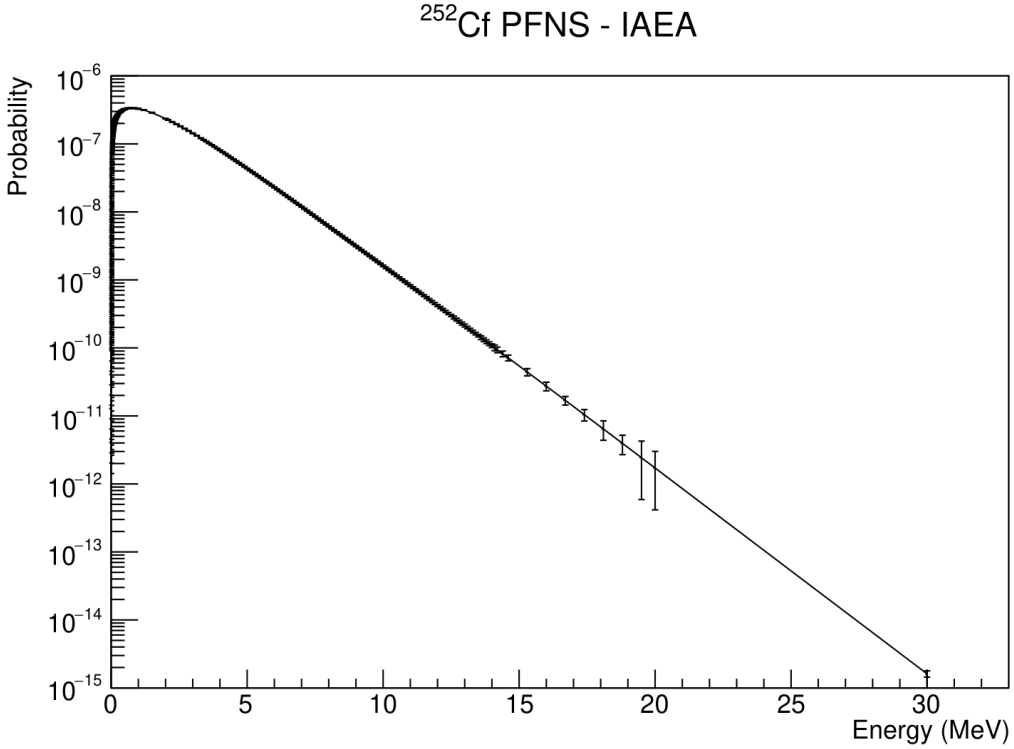

Figure 3.15 The ^{252}Cf PFNS as a function of neutron emitted energy E_n^{emit} obtained from the IAEA Neutron Data Standards [63] based on Refs [64, 65]

rays is also needed and the same procedure as in Section 3.1.1 is applied to the recorded ^{252}Cf dataset. The measured neutrons emitted from the ^{252}Cf source along with the translated cut is shown in Figure 3.16.

The cut algorithm in Section 3.2.1 is also applied to the ^{252}Cf histogram and the same time spectrum to energy spectrum procedure is used from Section 3.3 to produce a measured PFNS spectrum as seen in the liquid scintillator. For background subtraction, counts recorded at negative time differences before the prompt gamma ray (time difference $<$ -15 ns) were used. The selection is shown in Figure 3.17.

The background is developed as a function of pulse integral (can also be thought of E_n^{emit}) and counts are projected onto the y axis. During the conversion from a time spectrum, to energy spectrum, each corresponding energy bin gets subtracted by the respective background counts based on pulse integral value and is shown in Figure 3.18. The number of background counts is also divided by the time width of the background cut as a number of bins to obtain

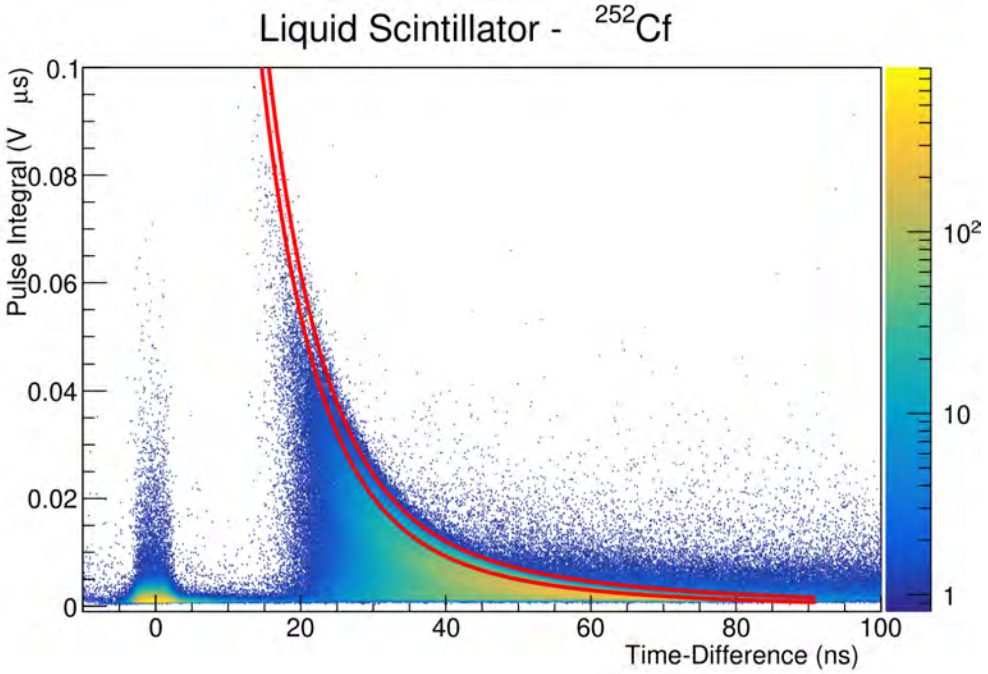

Figure 3.16 The ^{252}Cf liquid scintillator data recorded from spontaneous fission with the kinematically translated carbon cut (red) applied to the detector histogram.

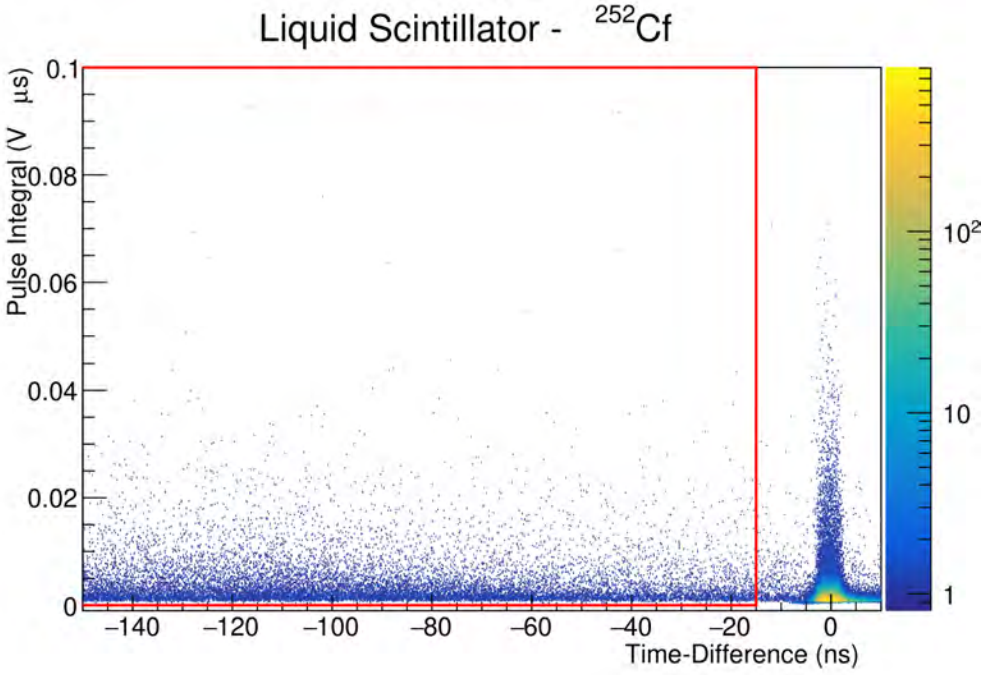

Figure 3.17 The liquid scintillator histogram data with the negative time difference values, ranging from -150 to -15 ns, selected (red). Near 0 ns is the prompt gamma ray from spontaneous fission of ^{252}Cf.

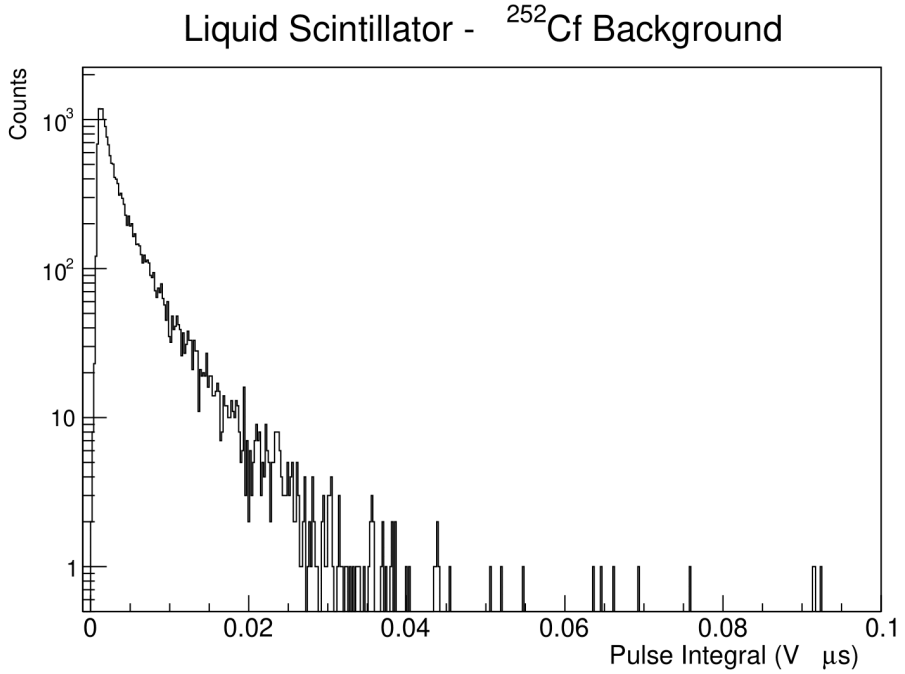

Figure 3.18 The used background of the ^{252}Cf data based on the cut and y-axis projection of Figure 3.17. The ^{252}Cf background is a function of pulse integral. The background presented is not divided by the number of time bins for clarity purposes so that the overall shape of the background can be viewed more clearly.

a background per bin value (not shown in Figure 3.18 for clarity purposes). Similarly, the recorded counts for a given energy bin (time bin that has been converted into an energy bin using scattering kinematics) are divided by the width of the energy bin. The recorded ^{252}Cf PFNS compared to the IAEA standard is shown in Figure 3.19. The IAEA ^{252}Cf values have been arbitrarily scaled by a factor of 10^{13} to ensure that the reference spectrum (Figure 3.15) is greater than the recorded spectrum.

The detector efficiency is found by dividing the data at each energy value, $s(E_n^{emit})$, by the scaled ^{252}Cf PFNS spectrum, $\xi(E_n^{emit})$, and is given in Equation 3.4

$$\varepsilon(E_n^{emit}) = \frac{s(E_n^{emit})}{\xi(E_n^{emit})}\,. \tag{3.4}$$

The calculated liquid scintillator detector efficiency is shown in Figure 3.20 is then applied to the measured carbon neutron elastic scattering spectrum shown in Figure 3.14.

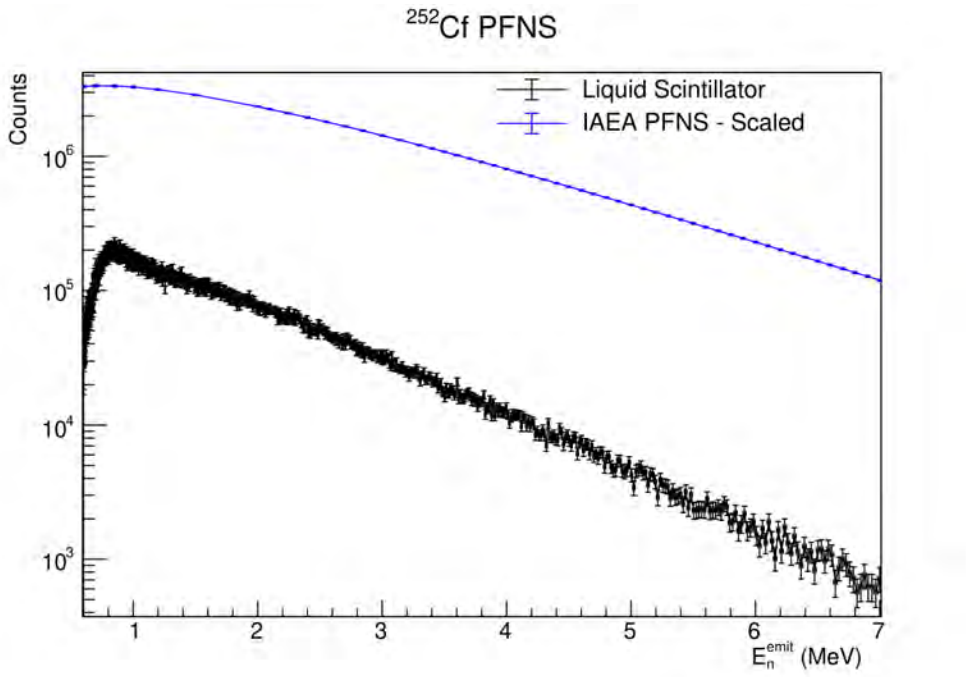

Figure 3.19 The recorded ^{252}Cf PFNS from the ^{252}Cf source placed in the center of the CoGNAC setup (black) compared with an arbitrarily scaled ^{252}Cf standard (blue). The plotted energy range for E_n^{emit} is 0.6 – 7 MeV.

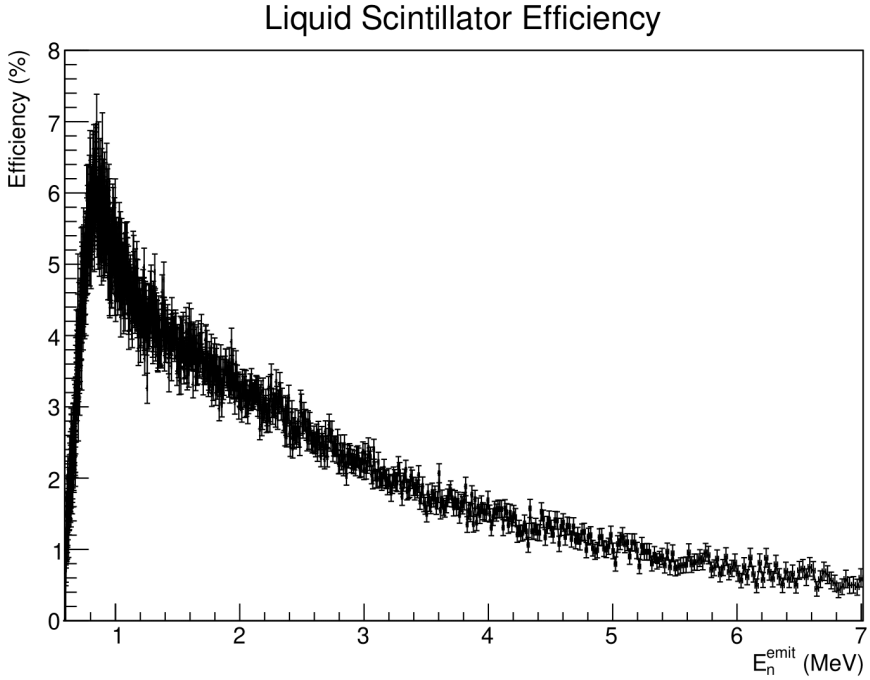

Figure 3.20 The calculated liquid scintillator detector efficiency using Equation 3.4. The plotted energy range for E_n^{emit} is 0.6 – 7 MeV.

3.4.2 Efficiency Application

The efficiency of the liquid scintillator calculated and shown in Figure 3.20 can now be applied to the energy spectrum shown in Figure 3.14. A conversion between neutron E_n^{inc} and E_n^{emit} is required as the PFNS and calculated efficiency are a function of E_n^{emit}. This can be done with Figure 3.6. The efficiency corrected spectrum is calculated as

$$c_\varepsilon\left(E_n^{inc}\right) = \frac{c\left(E_n^{inc}\right)}{\varepsilon\left(E_n^{emit}\right)}, \tag{3.5}$$

where $c\left(E_n^{inc}\right)$ is the raw counts of neutron elastically scattered neutrons from the carbon data and $\varepsilon\left(E_n^{emit}\right)$ is the efficiency (Figure 3.20) and $c_\varepsilon\left(E_n^{inc}\right)$ is the efficiency-corrected spectrum as a function of E_n^{inc}. The E_n^{emit} used in Equation 3.5 for the liquid scintillator efficiency is the same E_n^{emit} that is measured by the liquid scintillator for neutrons that scatter from ^{12}C at a given combination of E_n^{inc} and θ. No further bin width division is needed as the dimensions of the bins have already been divided in the production of the energy spectrum and the efficiency allowing for direct use of the two different quantities. The efficiency corrected spectrum is shown in Figure 3.21b.

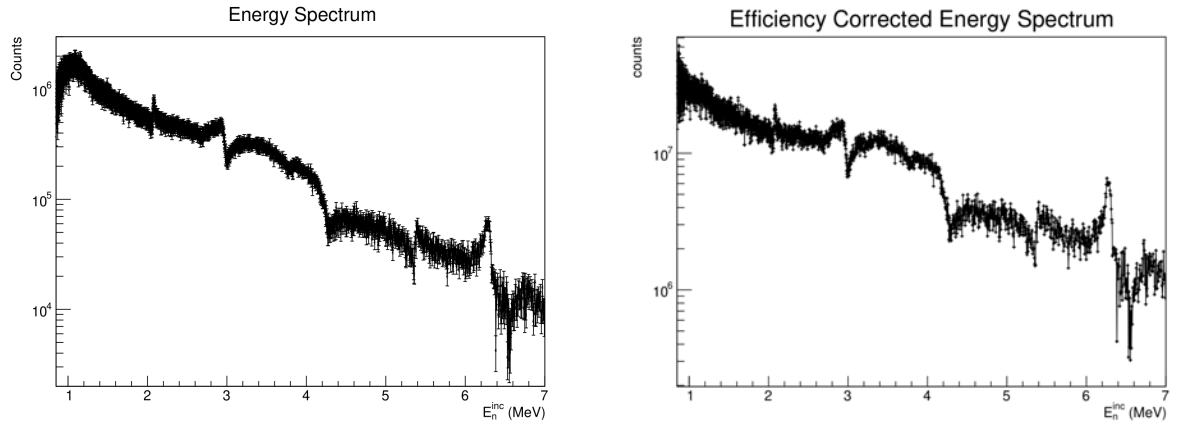

(a) **(b)**

Figure 3.21 The original energy spectrum as measured by the liquid scintillators is shown in Figure 3.21a. The energy spectrum of with efficiency correction is shown in Figure 3.21b. Plotted E_n^{inc} range is 0.85 – 7 MeV.

Looking at Figure 3.21, there is an overall shape agreement between the energy spectrum that does not have an efficiency applied (Figure 3.21a) but correcting the liquid scintillator

with the detector efficiency results in the most noticeable shape change at lower E_n^{inc} as seen in Figure 3.21b.

3.5 Neutron Flux

The flux was measured with a fission chamber located downstream of the CoGNAC array. The neutron beam induces fission events from the ^{235}U foil in the fission chamber. The neutron flux is calculated as

$$\Phi\left(E_n^{inc}\right) = \frac{f\left(E_n^{inc}\right)}{\sigma_f\left(E_n^{inc}\right)\Delta E}\,, \tag{3.6}$$

where $\Phi\left(E_n^{inc}\right)$ is the neutron flux as a function of incident neutron energy, $f\left(E_n^{inc}\right)$ is the number of fission events (neutron beam counts), $\sigma_f\left(E_n^{inc}\right)$ is the fission cross section of ^{235}U, and ΔE is the bin width (for bin width division as explained in Section 3.3). The fission cross section of ^{235}U is obtained from ENDF-B/VIII.0 [13, 66, 67], is a neutron cross section standard (standard energy range of $E_n^{inc} = 0.15$ – 200 MeV) [27, 29] within the range of this work ($E_n^{inc} = 0.85$ – 7 MeV) and is shown in Figure 3.22a. The fission cross section is divided out of the measured spectrum (Figure 3.22b) as the spectrum is measured relative to fission events of ^{235}U. The neutron flux is lastly calculated according to Equation 3.6 (Figure 3.22b divided by Figure 3.22a) and is shown in Figure 3.23.

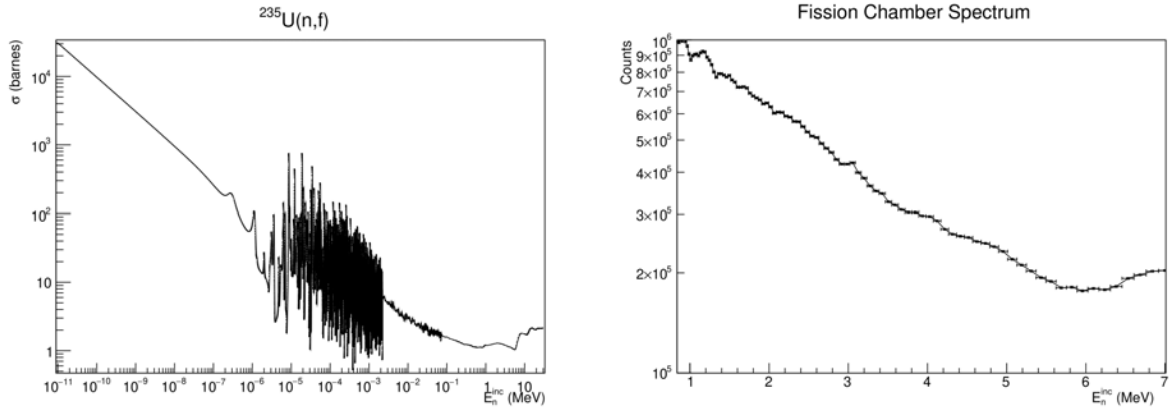

(a) **(b)**

Figure 3.22 The fission cross section of ^{235}U (Figure 3.22a) obtained from ENDF-B/VIII.0. The spectrum from the fission chamber (Figure 3.22b), with bin width division from $E_n^{inc} = 0.85$ – 7 MeV.

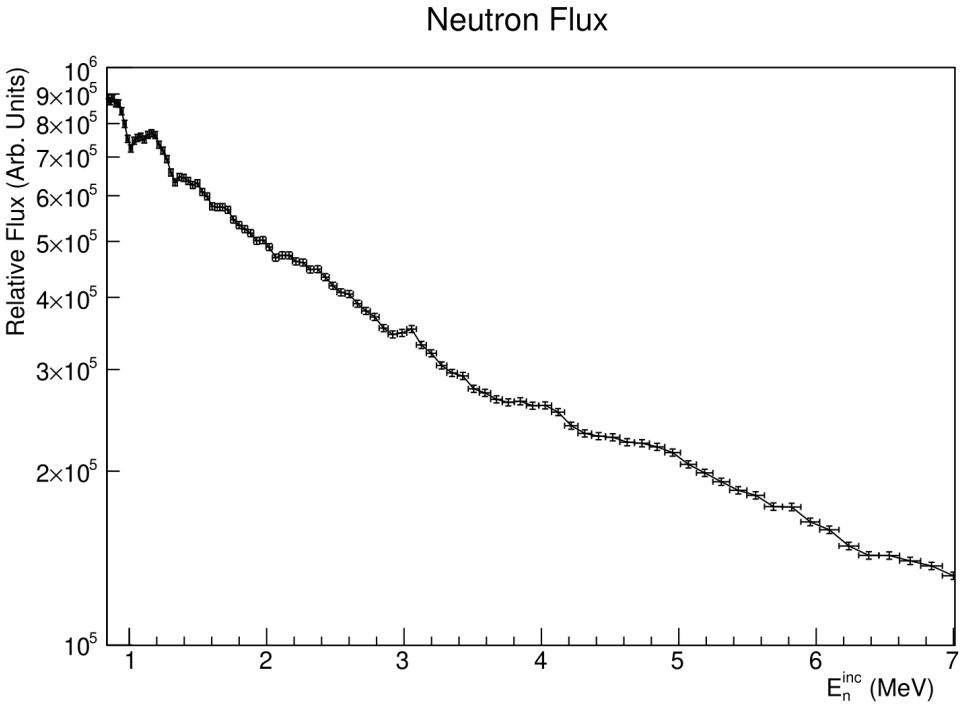

Figure 3.23 The neutron flux measured during the same beam cycle as the recorded carbon data at the fission chamber down beam of the CoGNAC setup from $E_n^{inc} = 0.85$ – 7 MeV.

3.6 Differential Angular Cross Section

To calculate the differential angular cross section $\frac{d\sigma}{d\Omega}$, one needs the measured spectrum of carbon elastic scattered neutrons, efficiency for the detector, and the measured neutron flux. The differential angular cross section as a function of incident neutron energy E_n^{inc} is calculated as shown in Equation 3.7

$$\frac{d\sigma}{d\Omega}\left(E_n^{inc}\right) = \frac{c\left(E_n^{inc}\right)}{\varepsilon\left(E_n^{emit}\right)\Phi\left(E_n^{inc}\right)} = \frac{c\left(E_n^{inc}\right)\xi\left(E_n^{emit}\right)\sigma_f\left(E_n^{inc}\right)}{s\left(E_n^{emit}\right)f\left(E_n^{inc}\right)}\,. \tag{3.7}$$

The later term in Equation 3.7 will be used to calculate the differential angular cross section and is in a useful form for uncertainty quantification and covariance calculation explained in Chapter 4. The carbon spectrum, $c\left(E_n^{inc}\right)$, is a function of incident neutron energy (Figure 3.14), $s\left(E_n^{emit}\right)$ is the measured PFNS spectrum from the ^{252}Cf source (Figure 3.19), $f\left(E_n^{inc}\right)$ is the measured neutron flux spectrum (Figure 3.22b), $\xi\left(E_n^{emit}\right)$ is the scaled ^{252}Cf PFNS from the Mannhart evaluation (Figure 3.15), and $\sigma_f\left(E_n^{inc}\right)$ is the ^{235}U fission cross section (Figure 3.22a). Calculating Equation 3.7 results in Figure 3.24.

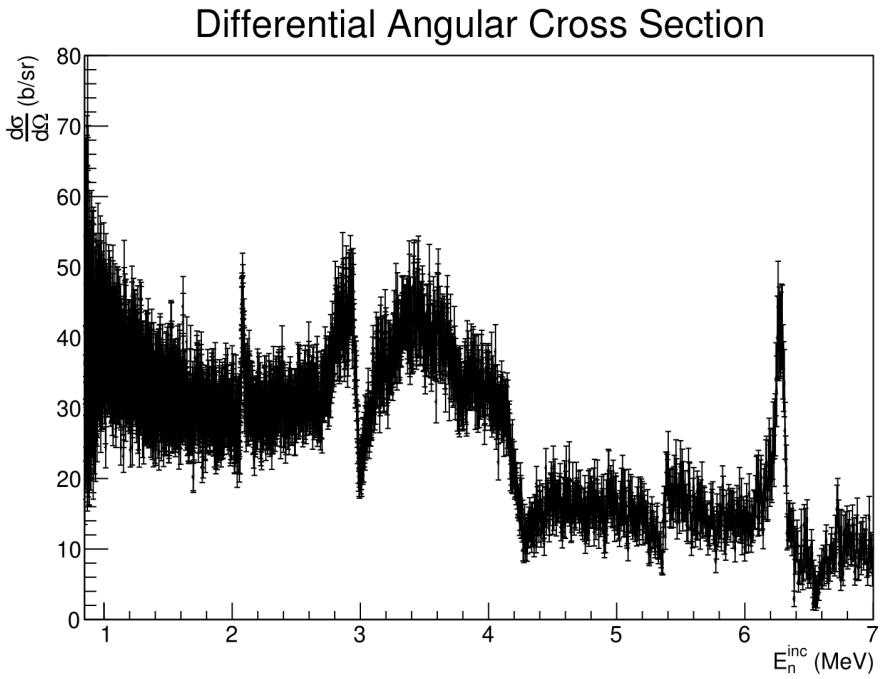

Figure 3.24 The differential angular cross section of a single liquid detector as describe by Equation 3.7 on the range of 0.85 - 7 MeV for E_n^{inc}

3.7 Integrated Cross Section

In order to calculate the integrated cross section utilizing the whole detector array, the liquid scintillators at the same angle are averaged together and then are integrated over the solid angle of the detector face. For example, all 6 liquid scintillators at $\theta = 120°$ will have their respective differential angular cross section $\frac{d\sigma}{d\Omega}$ averaged together. Averaging the differential angular cross section becomes clear when using Equation 3.7 with some simplification. If $x_i = \frac{c_i}{s_i}$ where i is the detector index, then summing each of the detectors produces

$$\begin{aligned}
\sum_i \frac{d\sigma}{d\Omega_i} &= \frac{x_i \xi \sigma_f}{6f} \\
&= \xi\sigma_f \left[\frac{x_1 + x_2 + x_3 + x_4 + x_5 + x_6}{6f}\right] \\
&= \frac{1}{6}\left[\frac{d\sigma}{d\Omega_1} + \frac{d\sigma}{d\Omega_2} + \frac{d\sigma}{d\Omega_3} + \frac{d\sigma}{d\Omega_4} + \frac{d\sigma}{d\Omega_5} + \frac{d\sigma}{d\Omega_6}\right] \\
&= \overline{\frac{d\sigma}{d\Omega}(\theta)}\,,
\end{aligned}$$

with the factor of 6 originating from the fact that 6 detector are shared at one given scattering angle, θ. This produces 9 averaged differential angular cross sections for each of the given 9 different θ values.

To calculate the integrated cross section for comparison with ENDF-B/VIII.0, the differential angular cross section is calculated as

$$\sigma\left(E_n^{inc}\right) = \int \overline{\frac{d\sigma}{d\Omega}\left(E_n^{inc}\right)} d\Omega = \int_{\phi_1}^{\phi_2} \int_{\theta_1}^{\theta_2} \overline{\frac{d\sigma}{d\Omega}\left(E_n^{inc}\right)} \sin\theta d\theta d\phi \,, \tag{3.8}$$

where θ_1 and θ_2 are $\pm 5°$ from the θ_d angle (Example: $\theta_1 = 115°$ and $\theta_2 = 125°$ for $\theta_d = 120°$). Finding the limits of integration for ϕ (ϕ_1 and ϕ_2) will depend on the value of θ given the fact that ϕ is not constant with changing θ. The necessary geometry to calculate what the respective limits of integration for ϕ is shown in Figure 3.25.

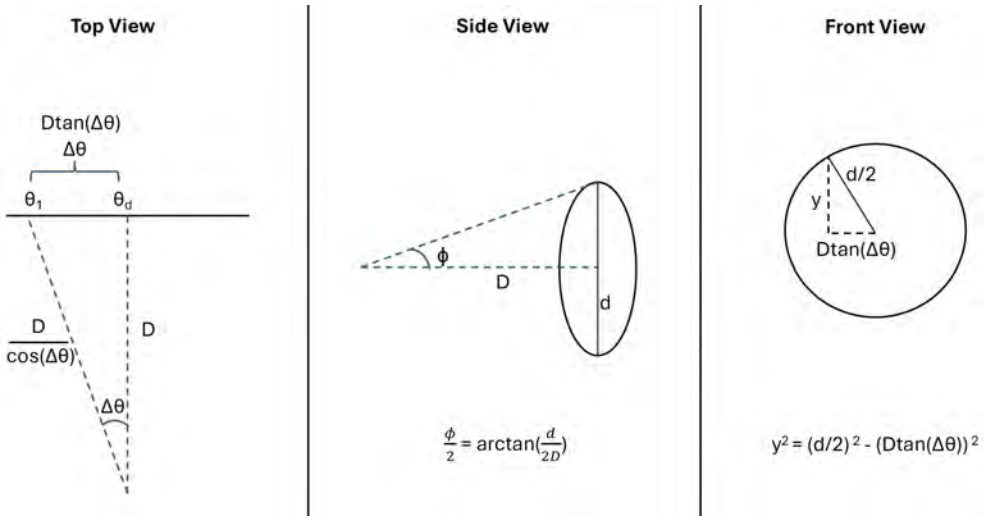

Figure 3.25 The geometric relationships to calculate the limits of integration for ϕ as shown from a top, side, and front view of the liquid scintillator. "D" is the distance from the center of CoGNAC to the liquid scintillator (1.02 m), "d" is the detector diameter, "y" is the effective distance of the liquid scintillator at a given θ and ϕ is the azimuthal value needed for the limits of integration.

The azimuthal angle ϕ is dependent upon the diameter of the liquid scintillator "d" and the distance from the center of CoGNAC to the liquid scintillator "D" as explained by the equation at the bottom of Figure 3.25 under the "Side View" section. Though, one needs an effective distance "y" that is smaller than the diameter of the liquid scintillator based

on the θ value. This effective distance is what is plugged into the equation to calculate ϕ is found simply by using the Pythagorean Theorem, as shown in the "Front View" section of Figure 3.25. The value of θ away from the detector center (θ_d) is $\Delta\theta$ (as seen in the "Top View" in Figure 3.25) and is used to calculate the distance away from the center of the detector Dtan($\Delta\theta$) which is used in the calculation of ϕ. This process is done for each θ_d value spanning from $\pm 5^\circ$ in 0.1° intervals. Table 3.2 summarizes the integration factor $\left(\int_{\phi_1}^{\phi_2}\int_{\theta_1}^{\theta_2}\sin\theta d\theta d\phi\right)$ applied to each of the averaged differential angular cross sections.

θ_d (°)	Integration Factor
150	0.13711
135	0.193903
120	0.236341
105	0.263569
90	0.272835
75	0.263508
60	0.236223
45	0.192839
30	0.136315

Table 3.2 The integration factor applied to each of the differential angular cross section data.

Once the differential angular cross sections have had their respective integration factors applied, the integrated cross section is calculated by summing each of the 9 spectra to produce an integrated angular cross section. The calculated integrated cross section result is presented in Chapter 5.

3.8 Peak Alignment Issue

During the data analysis process, it was discovered that there is a discrepancy with the location of structures within the calculated integrated cross section and what is reported in ENDF-B/VIII.0 for ^{12}C (n, el) cross section and previous experimental results. This discrepency is with respect to the E_n^{inc} location of structures in the integrated cross section. A plot of the integrated cross section without any time offset to the ^{252}Cf data and the carbon data is shown in Figure 3.26.

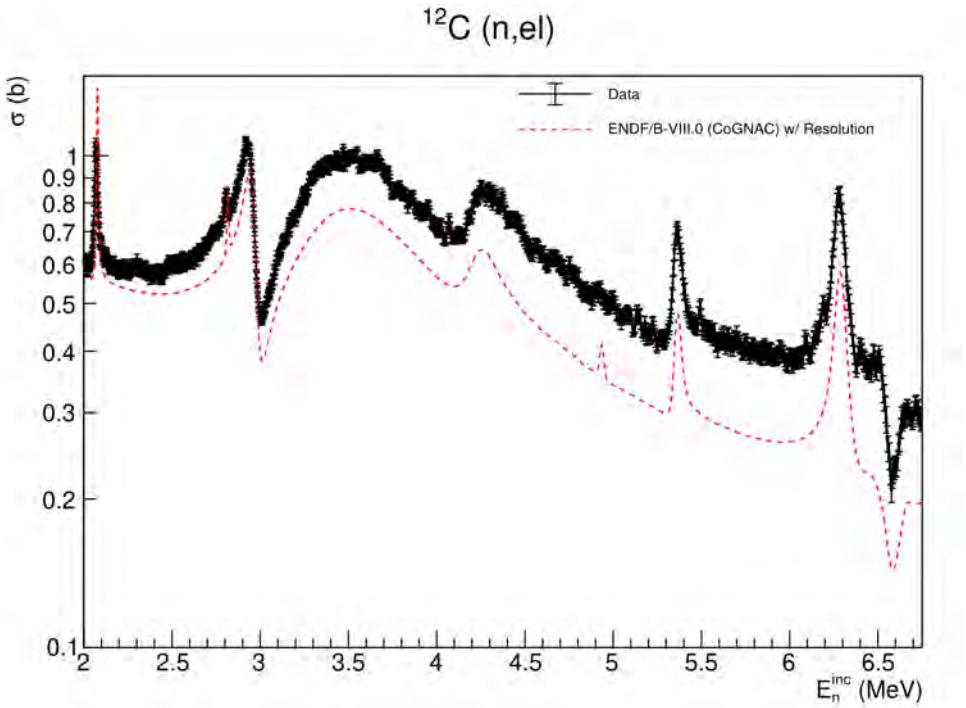

Figure 3.26 The ^{12}C integrated neutron elastic scattering without any time offset to the Carbon or ^{252}Cf data on the E_n^{inc} range of 2 – 6.75 MeV

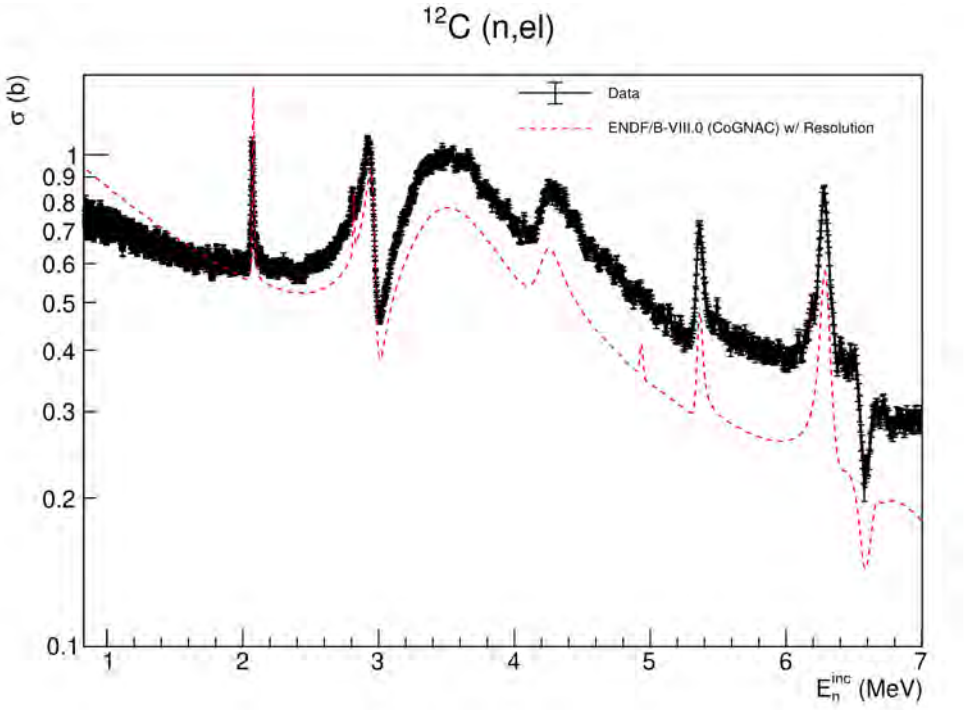

Figure 3.27 The same as Figure 3.26 but on the full analyzed E_n^{inc} range of 0.85 – 7 MeV. There is visible disagreement between the neutron standard region and the calculted cross section.

It can be seen when looking at the peak near 2 MeV and valley near 3 MeV, that the location of the peak is lower than was is indicated by ENDF-B/VIII.0 for neutron elastic scattering. Additionally, the peaks near 4.4 MeV, 5.4 MeV, and 6.3 MeV are higher than the reported location. Lastly, on the reported energy range, the standard region of the cross section (1 keV - 1.8 MeV) is not consistent with ENDF-B/VIII.0 as seen in Figure 3.27.

This misalignment indicates that there is an energy dependent offset. In an effort to align the measured integrated cross section with known resonances, a time offset of -1 ns is added to the time difference vs. E_n^{emit} relationship in the ^{252}Cf data. A uniform time offset corresponds to a non-uniform energy offset due to relativistic kinematics. This procedure results in the analyzed data being in agreement with the standard region for ^{12}C. The environmental conditions between the data taking setup for carbon and for measuring the PFNS of ^{252}Cf are different enough such that a 1 ns time difference is minimal enough to account for environmental differences in the two experimental data-taking setups. The integrated cross section with a -1 ns time offset (without any time offset in the carbon data) is shown in Figure 3.28. This level of time offset is consistent with time offsets required for CoGNAC (n, $n'\gamma$) measurements to obtain alignment with known resonance features.

Though when one zooms in on the structures around 2 MeV, 2.8 MeV, and 3 MeV, there is still a discrepancy in the data as seen in Figure 3.29.

Significant time and checks have been made to ensure that the relativistic kinematics presented in Chapter 1, Section 1.5 were implemented correctly and accurately in analysis codes. Additionally the methodology of analysis is similar to other analysis techniques done for cross section measurements with CoGNAC and no issues were able to be found. The difference in structure location disagreement was tracked back to the location of structures on the liquid scintillator histogram (Figure 3.2) disagreeing with the relativistic kinematics as predicted using the equations in Chapter 1, Section 1.5.

A simulation utilizing MCNP® (Monte Carlo N-Particle) [68, 69] ran by Josef Svoboda of P-2: Applied and Fundamental Physics, yielded the neutron time difference for neutrons

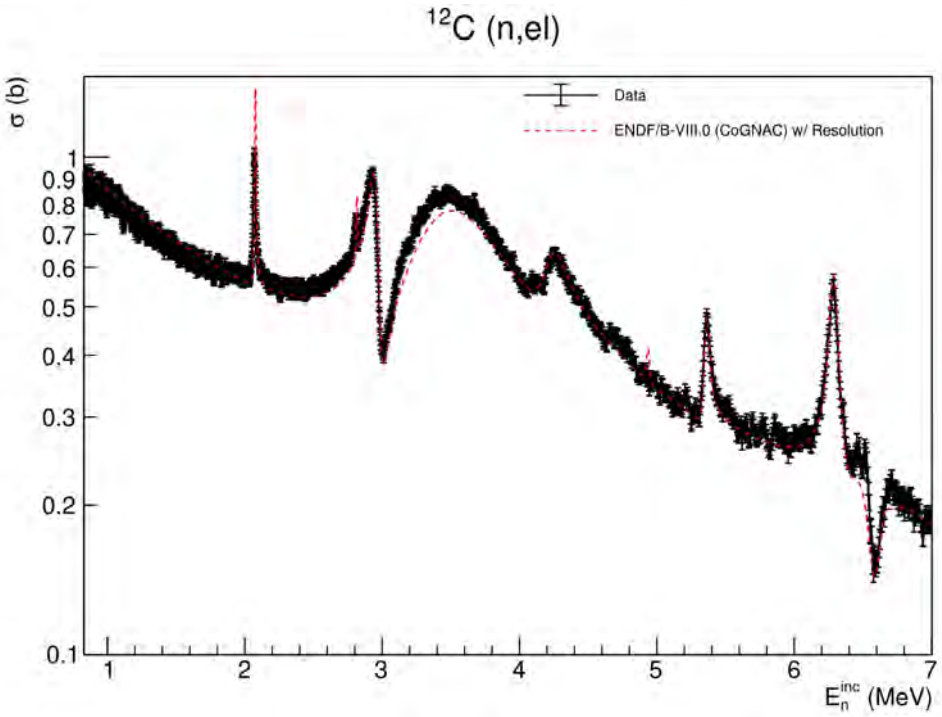

Figure 3.28 The calculated integrated cross section with a -1 ns offset applied to the ^{252}Cf data in the time difference vs. E_n^{emit}. The overall trend of the data agrees with the neutron standard region (1 keV – 1.8 MeV) of the ^{12}C neutron elastic scattering cross section.

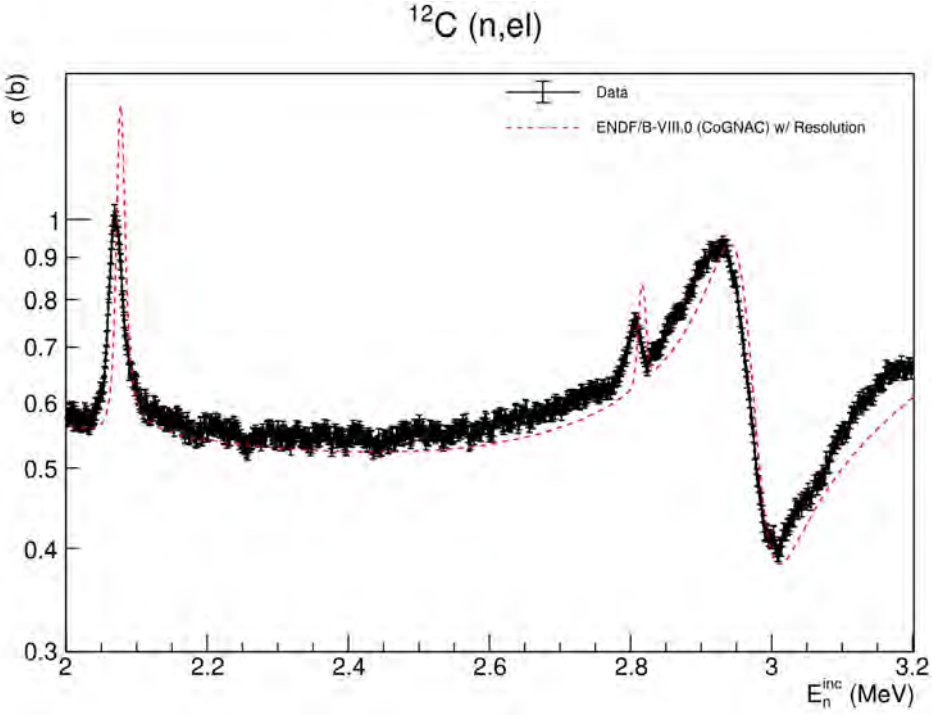

Figure 3.29 Same as Figure 3.28 but on zoomed in on the E_n^{inc} range of 2 - 3.2 MeV.

along flight path 15L coming from Target 4. The E_n^{inc} was taken in intervals of 1 MeV from 1 – 20 MeV with widths of 0.01% ($E_n^{inc} = 2 \pm 0.0002$ MeV). A simulated neutron flux is shown in Figure 3.30.

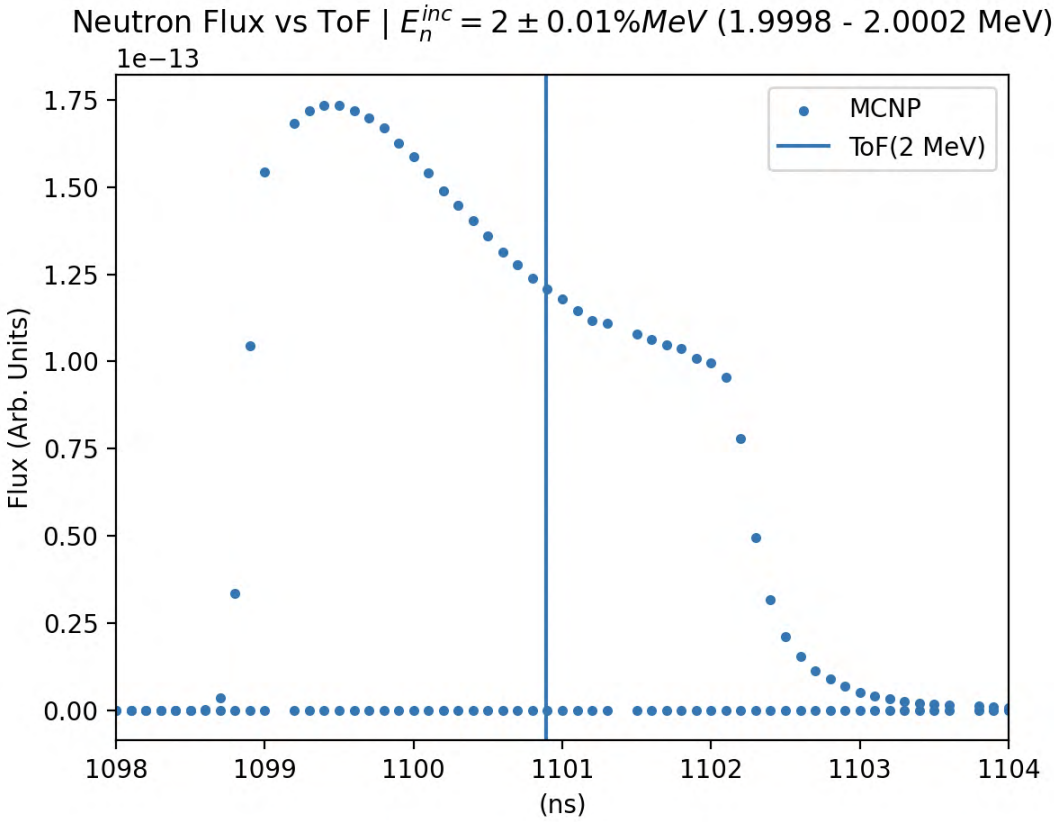

Figure 3.30 Simulated neutron flux using MCNP provided by Josef Svoboda of a $E_n^{inc} = 2 \pm 0.0002$ MeV neutron beam. The vertical line is the predicted neutron time difference utilizing scattering kinematics presented in Chapter 1, Section 1.5.

Even with a small spread in beam energy, there is structure of the neutron flux towards higher energies neutrons. A weighted average of the neutron time difference is taken with the weights being the respective flux values to produce a comparison between the predicted scattering kinematics values for a given E_n^{inc} and what is simulated in MCNP. The resulting comparison is shown in Figure 3.31.

As seen in Figure 3.31, MCNP tends to predict neutrons to have a shorter time difference than is predicted by scattering kinematics and is energy dependent. An offset with energy dependence is consistent with what appears in the carbon analysis. An additional time offset

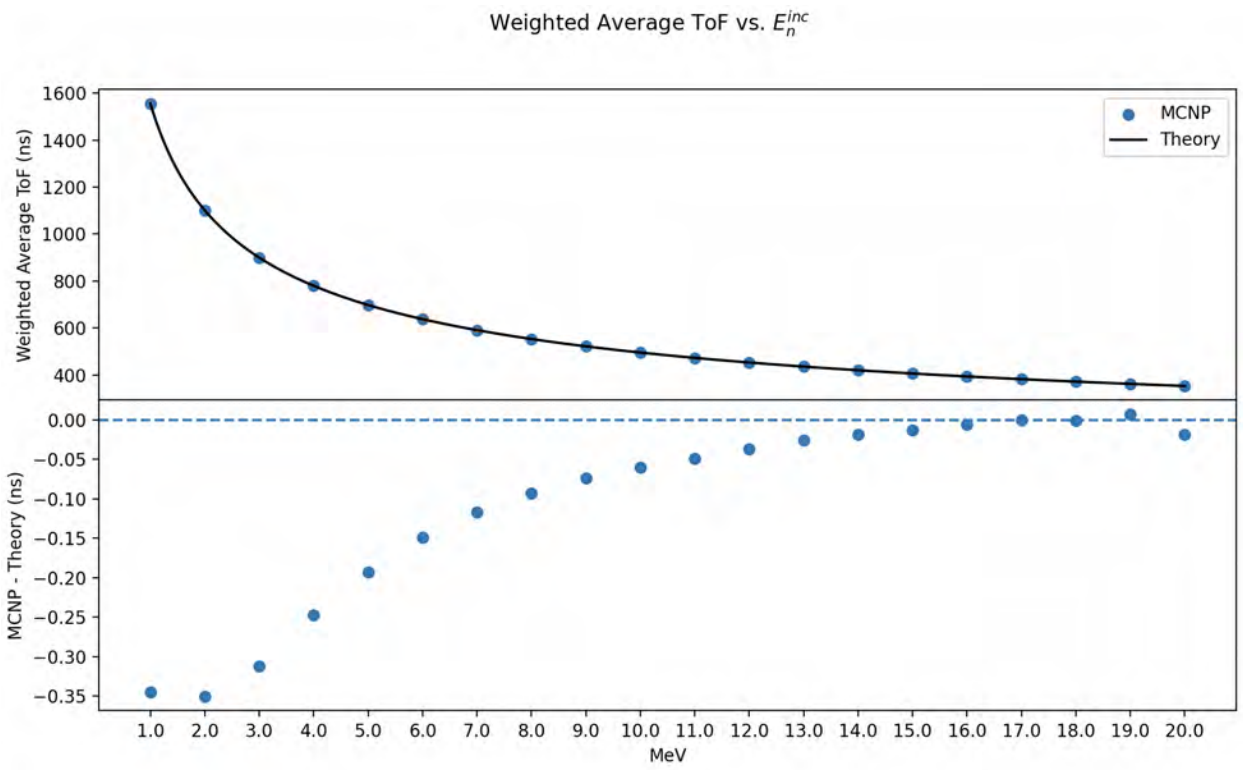

Figure 3.31 Top half of the plot shows the weighted average time difference of a neutron at a given E_n^{inc} (blue points) compared to using relativistic kinematics equations (black line). The difference between simulation and theory is shown in the bottom plot with the horizontal dashed line being equal to 0 (no difference).

was found by taking the difference between MCNP and Theory (scattering kinematics) and multiplying this time offset by 5 resulted in agreement between the calculated integrated cross section and what is seen in ENDF-B/VIII.0. A zoom in of the agreement with structures near 2 MeV, 2.8 MeV, and 3 MeV is shown in Figure 3.32 along with the previously mentioned -1 ns time offset included earlier.

Given the agreement by multiplying the time offset from MCNP to theory by a factor of 5, and the suggestion by simulation for shorter time differences by MCNP, this time difference is included into the integrated cross section calculation. Additionally, the total neutron cross section of carbon is equal to the elastic cross section up to the 1st excited state of ^{12}C (4.4398 MeV). The total cross section has been measured over numerous experiments implying the location of structures in the cross section below the 1st excited state is well know. As such, the introduction of a time offset to the carbon data to have structure below the 1st excited

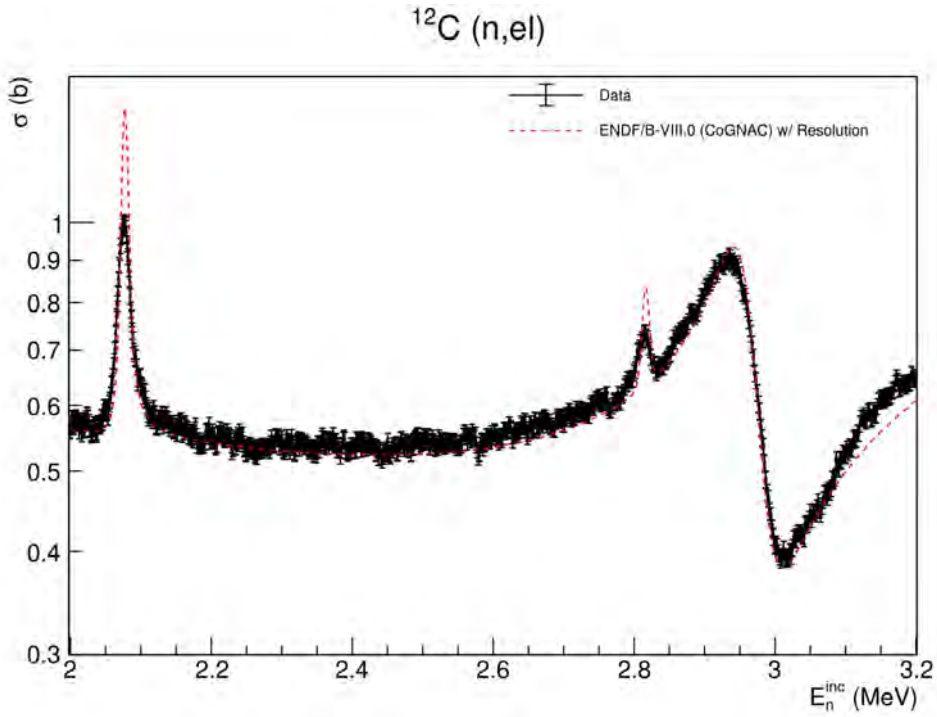

Figure 3.32 The ^{12}C integrated cross section with time offsets applied to the ^{252}Cf dataset and carbon using Figure 3.31.

state is justified. This time offset introduced into the carbon data is valid from 0.8 – 7 MeV based on best structure location agreement in the integrated cross section. An additional systematic uncertainty has been applied to the integrated result to reflect the need for the additional time corrections.

CHAPTER 4

UNCERTAINTY & COVARIANCE CALCULATION

While the analysis (Chapter 3) and results (Chapter 5) by themselves provides insight into the analyzed data, uncertainty quantification and the corresponding covariance and correlation matrices of the dataset provide a more complete picture of the obtained data and quantify the relationship of the presented results with itself over the range of reported energies. The covariance derivation procedures and results for the analysis performed for this dissertation are described in this chapter.

4.1 Covariance Calculation

Introduced in Chapter 1, the covariance **Cov** of a function $f(x)$ is found for the carbon spectrum, efficiency, flux, differential angular cross section, average differential angular cross section, and integrated cross section. The diagonal of the covariance matrix contains the variance **Var** for each of the calculated quantities. The variance is the square of the standard deviation (Gaussian 1σ) which is treated as the uncertainty for the measured and calculated quantities [41, 42, 43]. The main goal of calculating the covariance is to obtain uncertainties for calculated quantities (**Var**) and quantify the statistical relationship between the measured and calculated quantities across the reported neutron incident energy E_n^{inc} range.

The methodology of calculating the covariance matrix will involve solving the partial derivative of a given function $f(x)$ and carrying out the matrix multiplication as seen in Chapter 1, Section 1.6 given by Equation 1.39. In order to keep equations clear, x will not be displayed in equations and should be known to be the incident neutron energy E_n^{inc} or the emitted neutron energy E_n^{emit} dependent upon the quantity being calculated. Additionally, the subscripts i and j are used to denote two different neutron energies (either incident or emitted). For example y_i means quantity y (counts, PFNS, cross section, etc) at energy point i and the similar is true for y_j. For quantities notated as $\mathbf{Cov}[y_{ij}]$, means the covariance of y at the energy points of i and j. This notation is used in the case for the ^{252}Cf PFNS and ^{235}U fission cross section.

4.2 Carbon Spectrum

The function for calculating the carbon spectrum is

$$C = \frac{c - b}{\Delta E}\,, \tag{4.1}$$

where c is the carbon foreground counts, b is the background, and ΔE is the bin width (for bin width division). The covariance matrix $\mathbf{V}$, the matrix containing the uncertainties (as explained and defined in Equation 1.41 from Chapter 1, Section 1.6) of the quantities used in C, is simply constructed using the variance of the quantities at energies i and j on the diagonal. The uncertainty of measured counts is just the square root of the counts. The variance of c and b is the square of the uncertainty meaning $\mathbf{Var}[c] = c$. $\mathbf{V}$ is therefore

$$\mathbf{V} = \begin{bmatrix} \mathbf{Var}[c_i] & 0 & 0 & 0 \\ 0 & \mathbf{Var}[c_j] & 0 & 0 \\ 0 & 0 & \mathbf{Var}[b_i] & 0 \\ 0 & 0 & 0 & \mathbf{Var}[b_j] \end{bmatrix}. \tag{4.2}$$

The sensitivity matrix $\mathbf{A}$ is found by taking the partial derivative of f in Equation 4.1 with respect to each quantity (c or b) at energy i or j. This is then calculated to be

$$\mathbf{A} = \begin{bmatrix} \frac{\partial f_i}{\partial c_i} & \frac{\partial f_i}{\partial c_j} & \frac{\partial f_i}{\partial b_i} & \frac{\partial f_i}{\partial b_j} \\ \frac{\partial f_j}{\partial c_i} & \frac{\partial f_j}{\partial c_j} & \frac{\partial f_j}{\partial b_i} & \frac{\partial f_j}{\partial b_j} \end{bmatrix} = \begin{bmatrix} \frac{1}{\Delta E} & 0 & \frac{-1}{\Delta E} & 0 \\ 0 & \frac{1}{\Delta E} & 0 & \frac{-1}{\Delta E} \end{bmatrix}. \tag{4.3}$$

The covariance matrix $\mathbf{K_C}$ of C is given by

$$\mathbf{K_C} = \mathbf{AVA}^T \tag{4.4}$$

$$= \begin{bmatrix} \frac{1}{\Delta E} & 0 & \frac{-1}{\Delta E} & 0 \\ 0 & \frac{1}{\Delta E} & 0 & \frac{-1}{\Delta E} \end{bmatrix} \begin{bmatrix} \mathbf{Var}[c_i] & 0 & 0 & 0 \\ 0 & \mathbf{Var}[c_j] & 0 & 0 \\ 0 & 0 & \mathbf{Var}[b_i] & 0 \\ 0 & 0 & 0 & \mathbf{Var}[b_j] \end{bmatrix} \begin{bmatrix} \frac{1}{\Delta E} & 0 \\ 0 & \frac{1}{\Delta E} \\ \frac{-1}{\Delta E} & 0 \\ 0 & \frac{-1}{\Delta E} \end{bmatrix} \tag{4.5}$$

$$= \begin{bmatrix} \frac{\mathbf{Var}[c_i]+\mathbf{Var}[b_i]}{\Delta E^2} & 0 \\ 0 & \frac{\mathbf{Var}[c_j]+\mathbf{Var}[b_j]}{\Delta E^2} \end{bmatrix}. \tag{4.6}$$

The diagonals in Equations 4.6 are the variance of the carbon spectrum at energy points of i and j. It is important to note that the off diagonals in the calculated covariance matrix are 0 meaning there is no relationship between the background and measured carbon counts. This makes sense as these are two separate and independent measurements. The matrix in Equation 4.6 can further be simplified to

$$\mathbf{Cov}[C_{ij}] = \delta_{ij}\left[\frac{\mathbf{Var}[c_i] + \mathbf{Var}[b_i]}{\Delta E^2}\right], \tag{4.7}$$

where δ_{ij} is the Kronecker delta ($\delta_{ij} = 1$ if i=j and 0 otherwise) and knowing that $\mathbf{Cov}[x_{i=j}]$ = $\mathbf{Var}[x_i]$. Equation 4.7 shows that the form of the variance, and therefore the uncertainty (standard deviation) which is found by taking the square root of the variance, does not change with energy and each data point is only dependent upon the measured quantities at a given energy. Secondly, this is also a valuable form for implementation in analysis codes making covariance calculations iterative when the form becomes more complicated, as is the case with the integrated cross section.

4.3 Detector Efficiency

The calculation of the covariance matrix $\mathbf{K}_\varepsilon$ of the liquid scintillator detector efficiency follows the same process as the carbon spectrum with the addition of an existing covariance matrix for the ^{252}Cf PFNS. It is also important to note that for the efficiency, the neutron emitted energy E_n^{emit} is the energy of interest in this calculation. The equation for calculating the liquid scintillator efficiency is given by Equation 4.8

$$\varepsilon = \frac{s}{\xi}, \tag{4.8}$$

where s is the measured PFNS with background subtraction and bin width division, ΔE, accounted for and has a covariance of the same form of Equation 4.7. The ^{252}Cf PFNS standard is represented as ξ and also has an accompanying covariance that will be included in the covariance matrix $\mathbf{V}$. The sensitive matrix $\mathbf{A}$ is given by

$$\mathbf{A} = \begin{bmatrix} \frac{1}{\xi_i} & 0 & \frac{-s_i}{\xi_i^2} & 0 \\ 0 & \frac{1}{\xi_j} & 0 & \frac{-s_j}{\xi_j^2} \end{bmatrix}, \tag{4.9}$$

and the covariance matrix $\mathbf{V}$ is given by

$$\mathbf{V} = \begin{bmatrix} \mathbf{Var}[s_i] & 0 & 0 & 0 \\ 0 & \mathbf{Var}[s_j] & 0 & 0 \\ 0 & 0 & \mathbf{Var}[\xi_i] & \mathbf{Cov}[\xi_{ij}] \\ 0 & 0 & \mathbf{Cov}[\xi_{ji}] & \mathbf{Var}[\xi_j] \end{bmatrix}, \tag{4.10}$$

where the off diagonal contains the covariance of the ^{252}Cf PFNS. Conceptually, this is comes from the fact that each detector will measure a slightly different neutron spectrum from the ^{252}Cf source (due to small variations between each detector), but each detector is compared to the same reference standard and therefore becomes "linked". The covariance of the ^{252}Cf PFNS is obtained from the ENDF-B/VIII.0 correlation plot [13, 70] and is multiplied by the uncertainties in the ^{252}Cf PFNS standard from Refs. [63, 64, 65]. The PFNS correlation matrix of ^{252}Cf as used in this work is shown in Figure 4.1.

The correlation matrix is chosen to be shown to more clearly see the overall structure and behavior of the ^{252}Cf PFNS correlation matrix as well as to foreshadow some of the the major features that should appear in the integrated cross section correlation matrix (and similarly, the covariance matrix).

The covariance matrix $\mathbf{K}_\varepsilon$ is then calculated to be

$$\mathbf{K}_\varepsilon = \mathbf{AVA}^T \tag{4.11}$$

$$= \begin{bmatrix} \frac{1}{\xi_i} & 0 & \frac{-s_i}{\xi_i^2} & 0 \\ 0 & \frac{1}{\xi_j} & 0 & \frac{-s_j}{\xi_j^2} \end{bmatrix} \begin{bmatrix} \mathbf{Var}[s_i] & 0 & 0 & 0 \\ 0 & \mathbf{Var}[s_j] & 0 & 0 \\ 0 & 0 & \mathbf{Var}[\xi_i] & \mathbf{Cov}[\xi_{ij}] \\ 0 & 0 & \mathbf{Cov}[\xi_{ji}] & \mathbf{Var}[\xi_j] \end{bmatrix} \begin{bmatrix} \frac{1}{\xi_i} & 0 \\ 0 & \frac{1}{\xi_j} \\ \frac{-s_i}{\xi_i^2} & 0 \\ 0 & \frac{-s_j}{\xi_j^2} \end{bmatrix} \tag{4.12}$$

$$= \begin{bmatrix} \frac{\mathbf{Var}[s_i]}{\xi_i^2} + \frac{s_i^2}{\xi_i^4}\mathbf{Var}[\xi_i] & \frac{s_i s_j}{\xi_i^2 \xi_j^2}\mathbf{Cov}[\xi_{ij}] \\ \frac{s_i s_j}{\xi_i^2 \xi_j^2}\mathbf{Cov}[\xi_{ij}] & \frac{\mathbf{Var}[s_j]}{\xi_j^2} + \frac{s_j^2}{\xi_j^4}\mathbf{Var}[\xi_j] \end{bmatrix}. \tag{4.13}$$

Notice that off diagonal terms appear in the covariance matrix $\mathbf{K}_\varepsilon$ originate from the covari-

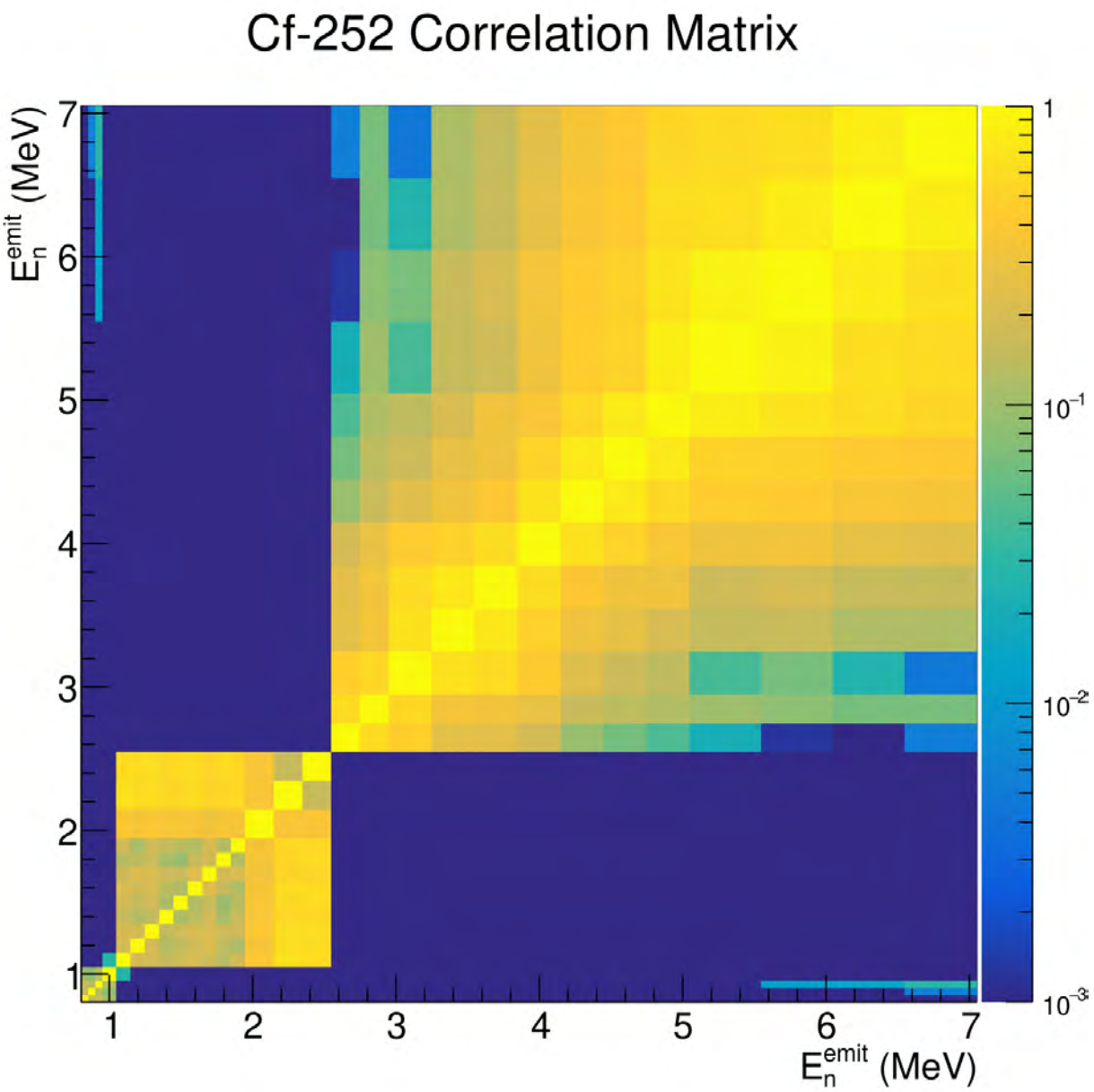

Figure 4.1 The correlation matrix of the ^{252}Cf PFNS obtained from ENDF-B/VIII.0 [13, 70] of the ^{252}Cf PFNS standard [63, 64, 65]. The x- and y-axis are plotted on the range of $E_n^{emit} = 0.6 - 7$ MeV.

ance of the ^{252}Cf PFNS. Equation 4.13 can be further simplified to

$$\mathbf{Cov}[\varepsilon_{ij}] = \delta_{ij}\left[\frac{\mathbf{Cov}[s_{ij}]}{\xi_i\xi_j}\right] + \frac{s_i s_j}{\xi_i^2\xi_j^2}\mathbf{Cov}[\xi_{ij}]\,. \tag{4.14}$$

4.4 Neutron Flux

The process for calculating the covariance matrix of the neutron flux $\mathbf{K_\Phi}$ is very similar to the process used for the detector efficiency. The flux is calculated to be

$$\Phi = \frac{f}{\sigma_f}\,, \tag{4.15}$$

where f is the number of counts in the fission chamber detector (with bin width division accounted for) and σ_f is the neutron induced fission cross section of ^{235}U. Similar to the PFNS of ^{252}Cf, there is also a correlation matrix for the fission cross section of ^{235}U. The correlation matrix is obtained from ENDF-B/VIII.0 [13, 71] and based on the work in Ref. [67]. The correlation matrix is shown in Figure 4.2.

The covariance is found by multiplying the correlation matrix by the appropriate uncertainty in the ^{235}U fission cross section. The block structure along the diagonal should also appear in the final correlation and covariance matrices of the integrated cross section. Similar to the calculation of the efficiency covariance, the calculation of the flux covariance $\mathbf{K_\Phi}$ follows the same procedure and is shown to be

$$\mathbf{K_\Phi} = \mathbf{AVA}^T \tag{4.16}$$

$$= \begin{bmatrix} \frac{1}{\sigma_{f_i}} & 0 & \frac{-f_i}{\sigma_{f_i}^2} & 0 \\ 0 & \frac{1}{\sigma_{f_j}} & 0 & \frac{-f_j}{\sigma_{f_j}^2} \end{bmatrix} \begin{bmatrix} \mathbf{Var}[f_i] & 0 & 0 & 0 \\ 0 & \mathbf{Var}[f_j] & 0 & 0 \\ 0 & 0 & \mathbf{Var}[\sigma_{f_i}] & \mathbf{Cov}[\sigma_{f_{ij}}] \\ 0 & 0 & \mathbf{Cov}[\sigma_{f_{ji}}] & \mathbf{Var}[\sigma_{f_j}] \end{bmatrix} \begin{bmatrix} \frac{1}{\sigma_{f_i}} & 0 \\ 0 & \frac{1}{\sigma_{f_j}} \\ \frac{-f_i}{\sigma_{f_i}^2} & 0 \\ 0 & \frac{-f_j}{\sigma_{f_j}^2} \end{bmatrix} \tag{4.17}$$

$$= \begin{bmatrix} \frac{\mathbf{Var}[f_i]}{\sigma_{f_i}^2} + \frac{f_i^2}{\sigma_{f_i}^4}\mathbf{Var}[\sigma_{f_i}] & \frac{f_i f_j}{\sigma_{f_i}^2\sigma_{f_j}^2}\mathbf{Cov}[\sigma_{f_{ij}}] \\ \frac{f_i f_j}{\sigma_{f_i}^2\sigma_{f_j}^2}\mathbf{Cov}[\sigma_{f_{ij}}] & \frac{\mathbf{Var}[f_j]}{\sigma_{f_j}^2} + \frac{f_j^2}{\sigma_{f_j}^4}\mathbf{Var}[\sigma_{f_j}] \end{bmatrix}, \tag{4.18}$$

where Equation 4.18 is of the same form as Equation 4.13. Equation 4.18 can be simplified to

$$\mathbf{Cov}[\Phi_{ij}] = \delta_{ij}\left[\frac{\mathbf{Cov}[f_{ij}]}{\sigma_{f_i}\sigma_{f_j}}\right] + \frac{f_i f_j}{\sigma_{f_i}^2\sigma_{f_j}^2}\mathbf{Cov}[\sigma_{f_{ij}}]\,. \tag{4.19}$$

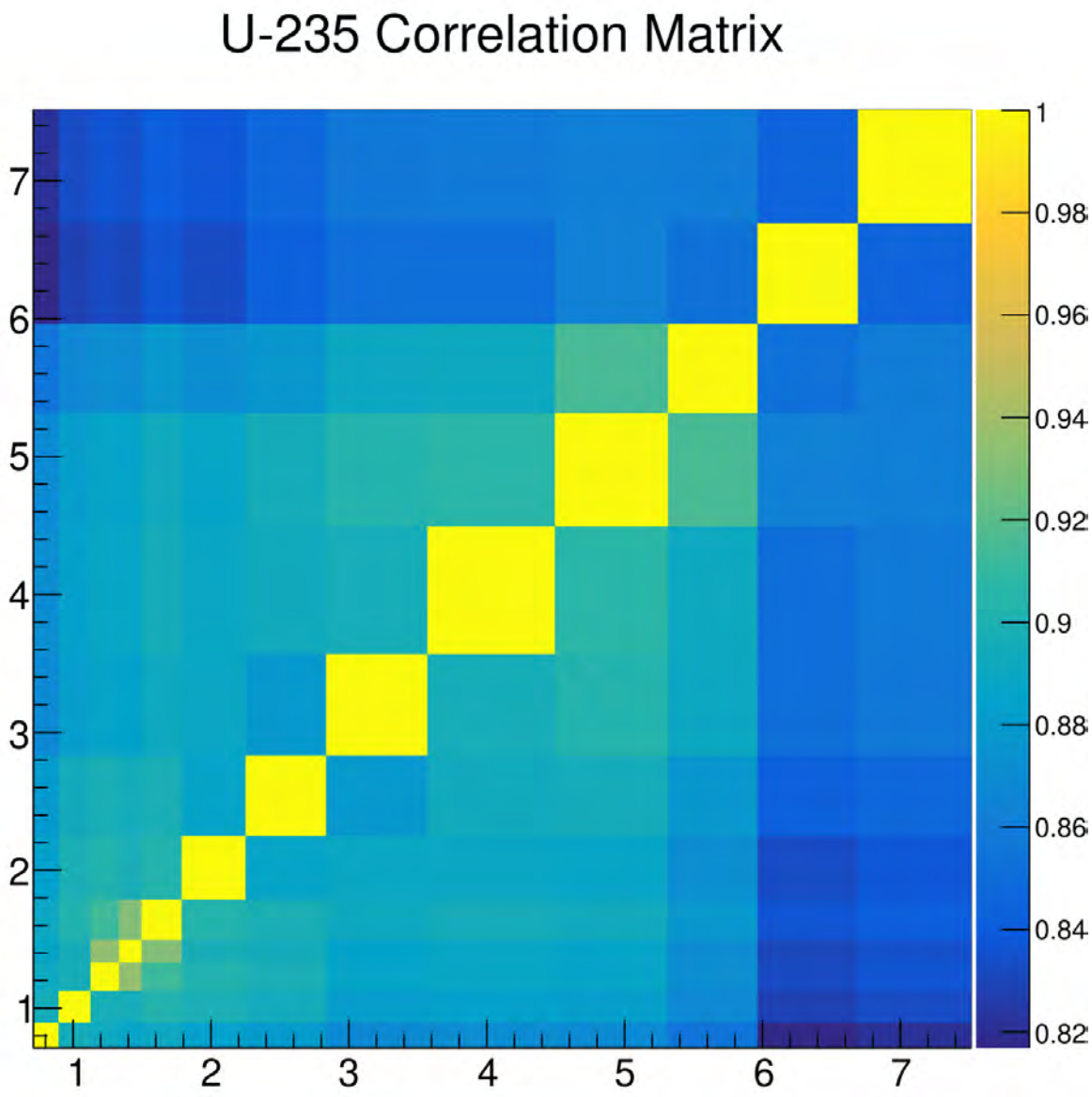

Figure 4.2 The correlation matrix of the ^{235}U fission cross section [67, 72] from ENDF-B/VIII.0 [13, 71]. The x- and y-axis are plotted on the range of $E_n^{inc} = 0.85 - 7$ MeV.

4.5 Differential Angular Cross Section

For calculating the covariance of the differential angular cross section $\mathbf{K}_{\frac{\mathbf{d}\sigma}{\mathbf{d}\Omega}}$, the equation to calculate $\frac{d\sigma}{d\Omega}$ is

$$\frac{d\sigma}{d\Omega} = \frac{c\xi\sigma_f}{sf}\,, \tag{4.20}$$

the sensitivity matrix $\mathbf{A}$ is given by

$$\mathbf{A} = \begin{bmatrix} \frac{\xi_i\sigma_{f_i}}{s_i f_i} & 0 & \frac{-c_i\xi_i\sigma_{f_i}}{s_i^2 f_i} & 0 & \frac{-c_i\xi_i\sigma_{f_i}}{s_i f_i^2} & 0 & \frac{c_i\sigma_{f_i}}{s_i f_i} & 0 & \frac{c_i\xi_i}{s_i f_i} & 0 \\ 0 & \frac{\xi_j\sigma_{f_j}}{s_j f_j} & 0 & \frac{-c_j\xi_j\sigma_{f_j}}{s_j^2 f_j} & 0 & \frac{-c_j\xi_j\sigma_{f_j}}{s_j f_j^2} & 0 & \frac{c_j\sigma_{f_j}}{s_j f_j} & 0 & \frac{c_j\xi_j}{s_j f_j} \end{bmatrix}, \tag{4.21}$$

the covariance matrix $\mathbf{V}$ is

$$\mathbf{V} = \begin{bmatrix} \mathbf{Var}[c_i] & 0 & 0 & 0 & 0 & 0 & 0 & 0 & 0 & 0 \\ 0 & \mathbf{Var}[c_j] & 0 & 0 & 0 & 0 & 0 & 0 & 0 & 0 \\ 0 & 0 & \mathbf{Var}[s_i] & 0 & 0 & 0 & 0 & 0 & 0 & 0 \\ 0 & 0 & 0 & \mathbf{Var}[s_j] & 0 & 0 & 0 & 0 & 0 & 0 \\ 0 & 0 & 0 & 0 & \mathbf{Var}[f_i] & 0 & 0 & 0 & 0 & 0 \\ 0 & 0 & 0 & 0 & 0 & \mathbf{Var}[f_j] & 0 & 0 & 0 & 0 \\ 0 & 0 & 0 & 0 & 0 & 0 & \mathbf{Var}[\xi_i] & \mathbf{Cov}[\xi_{ij}] & 0 & 0 \\ 0 & 0 & 0 & 0 & 0 & 0 & \mathbf{Cov}[\xi_{ji}] & \mathbf{Var}[\xi_j] & 0 & 0 \\ 0 & 0 & 0 & 0 & 0 & 0 & 0 & 0 & \mathbf{Var}[\xi_i] & \mathbf{Cov}[\xi_{ij}] \\ 0 & 0 & 0 & 0 & 0 & 0 & 0 & 0 & \mathbf{Cov}[\xi_{ji}] & \mathbf{Var}[\xi_j] \end{bmatrix}, \tag{4.22}$$

and lastly, the covariance of the differential angular cross section $\mathbf{K}_{\frac{\mathbf{d}\sigma}{\mathbf{d}\Omega}}$ is found to be

$$\mathbf{K}_{\frac{\mathbf{d}\sigma}{\mathbf{d}\Omega}} = \begin{bmatrix} \mathbf{Var}[\frac{d\sigma}{d\Omega}_i] & \mathbf{Cov}[\frac{d\sigma}{d\Omega}_{ij}] \\ \mathbf{Cov}[\frac{d\sigma}{d\Omega}_{ji}] & \mathbf{Var}[\frac{d\sigma}{d\Omega}_j] \end{bmatrix}, \tag{4.23}$$

with

$$\mathbf{Var}\left[\frac{d\sigma}{d\Omega}_{i(j)}\right] = \frac{\xi_i^2{\sigma_{f_i}}^2}{s_i^2 f_i^2}\mathbf{Var}[c_i] + \frac{c_i^2\xi_i^2{\sigma_{f_i}}^2}{s_i^4 f_i^2}\mathbf{Var}[s_i] + \frac{c_i^2\xi_i^2{\sigma_{f_i}}^2}{s_i^2 f_i^4}\mathbf{Var}[f_i] + \mathbf{Cov}\left[\frac{d\sigma}{d\Omega}_{ij}\right], \tag{4.24}$$

and

$$\mathbf{Cov}\left[\frac{d\sigma}{d\Omega}_{ij}\right] = \frac{c_i c_j\sigma_{f_i}\sigma_{f_j}}{s_i s_j f_i f_j}\mathbf{Cov}[\xi_{ij}] + \frac{c_i c_j\xi_i\xi_j}{s_i s_j f_i f_j}\mathbf{Cov}[\sigma_{f_{ij}}]\,, \tag{4.25}$$

again noting that if $i = j$ then $\mathbf{Cov}[\xi_{ij}]$ and $\mathbf{Cov}[\sigma_{f_{ij}}]$ are just $\mathbf{Var}[\xi_i]$ and $\mathbf{Var}[\sigma_{f_i}]$ respectively. Similarly, the covariance can be simplified to

$$\begin{aligned}\mathbf{Cov}\left[\frac{d\sigma}{d\Omega}\right] = \delta_{ij}\left[\frac{\xi_i^2 {\sigma_{f_i}}^2}{s_i^2 f_i^2}\mathbf{Var}[c_i] + \frac{c_i^2 \xi_i^2 {\sigma_{f_i}}^2}{s_i^4 f_i^2}\mathbf{Var}[s_i] + \frac{c_i^2 \xi_i^2 {\sigma_{f_i}}^2}{s_i^2 f_i^4}\mathbf{Var}[f_i]\right] \\ + \frac{c_i c_j \sigma_{f_i}\sigma_{f_j}}{s_i s_j f_i f_j}\mathbf{Cov}[\xi_{ij}] + \frac{c_i c_j \xi_i \xi_j}{s_i s_j f_i f_j}\mathbf{Cov}[\sigma_{f_{ij}}]\,,\end{aligned} \tag{4.26}$$

where only the covariance of the ^{235}U fission cross section and the ^{252}Cf PFNS contribute on the off diagonals.

4.6 Detector Average

For the covariance matrix calculation of the detector average $\mathbf{K}_{\frac{\mathbf{d\sigma}}{\mathbf{d\Omega}}}$, it is desirable to represent terms in the variance and off diagonal covariance in simplified terms of already calculated quantities. In order to establish a pattern for the detector average only two detectors (x and y) that share the same θ_d are used in the derivation. This simplification also more clearly shows the relationship and pattern in the variance and off diagonal covariance term. The function for the average differential angular cross section $\overline{\frac{d\sigma}{d\Omega}}$ is given by

$$\overline{\frac{d\sigma}{d\Omega}} = \frac{\xi\sigma_f}{nf}\left(\frac{c_x}{s_x} + \frac{c_y}{s_y}\right)\,, \tag{4.27}$$

where the subscripts of x and y correspond to detectors x and y and n is the number of detectors at a given θ_d (in this example, $n = 2$).

For the covariance matrix $\mathbf{V}$

$$\mathbf{V} = \begin{bmatrix}\mathbf{V_X} & 0 & 0\\ 0 & \mathbf{V_Y} & 0\\ 0 & 0 & \mathbf{V_O}\end{bmatrix}\,, \tag{4.28}$$

where $\mathbf{V_X}$ is the matrix pertaining to the x detector (c_x and s_x), $\mathbf{V_Y}$ is the matrix pertaining to the y detector, and $\mathbf{V_O}$ is the matrix for shared terms such as the neutron flux counts f,

^{235}U fission cross section σ_f, and the ^{252}Cf PFNS ξ and are defined as

$$\mathbf{V_X} = \begin{bmatrix} c_{x_i} & 0 & 0 & 0 \\ 0 & c_{x_j} & 0 & 0 \\ 0 & 0 & s_{x_i} & 0 \\ 0 & 0 & 0 & s_{x_i} \end{bmatrix}, \tag{4.29}$$

$$\mathbf{V_Y} = \begin{bmatrix} c_{y_i} & 0 & 0 & 0 \\ 0 & c_{y_j} & 0 & 0 \\ 0 & 0 & s_{y_i} & 0 \\ 0 & 0 & 0 & s_{y_i} \end{bmatrix}, \tag{4.30}$$

$$\mathbf{V_O} = \begin{bmatrix} f_i & 0 & 0 & 0 & 0 & 0 \\ 0 & f_j & 0 & 0 & 0 & 0 \\ 0 & 0 & \mathbf{Var}[\xi_i] & \mathbf{Cov}[\xi_{ij}] & 0 & 0 \\ 0 & 0 & \mathbf{Cov}[\xi_{ji}] & \mathbf{Var}[\xi_j] & 0 & 0 \\ 0 & 0 & 0 & 0 & \mathbf{Var}[\sigma_{f_i}] & \mathbf{Cov}[\sigma_{f_{ij}}] \\ 0 & 0 & 0 & 0 & \mathbf{Cov}[\sigma_{f_{ji}}] & \mathbf{Var}[\sigma_{f_j}] \end{bmatrix}, \tag{4.31}$$

resulting in a 14x14 matrix for Equation 4.28. The sensitivity matrix is then calculated to be

$$\mathbf{A} = \begin{bmatrix} \mathbf{A_X} & \mathbf{A_Y} & \mathbf{A_f} & \mathbf{A}_\xi & \mathbf{A}_{\sigma_\mathbf{f}} \end{bmatrix}, \tag{4.32}$$

with the x detector sensitivity matrix $\mathbf{A_X}$, y detector sensitivity matrix $\mathbf{A_Y}$, neutron flux sensitivity matrix $\mathbf{A_f}$, the ^{252}Cf PFNS sensitivity matrix $\mathbf{A}_\xi$, and the ^{235}U fission cross section sensitivity $\mathbf{A}_{\sigma_\mathbf{f}}$ matrix are all defined to be

$$\mathbf{A_X} = \begin{bmatrix} \frac{\xi_i \sigma_{f_i}}{n s_{x_i} f_i} & 0 & -\frac{c_{x_i} \xi_i \sigma_{f_i}}{n s_{x_i}^2 f_i} & 0 \\ 0 & \frac{\xi_j \sigma_{f_j}}{n s_{x_j} f_j} & 0 & -\frac{c_{x_j} \xi_j \sigma_{f_j}}{n s_{x_j}^2 f_j} \end{bmatrix} = \begin{bmatrix} \frac{1}{n c_{x_i}} \frac{d\sigma}{d\Omega} x_i & 0 & -\frac{1}{n s_{x_i}} \frac{d\sigma}{d\Omega} x_i & 0 \\ 0 & \frac{1}{n c_{x_j}} \frac{d\sigma}{d\Omega} x_j & 0 & -\frac{1}{n s_{x_j}} \frac{d\sigma}{d\Omega} x_j \end{bmatrix}, \tag{4.33}$$

$$\mathbf{A_Y} = \begin{bmatrix} \frac{\xi_i \sigma_{f_i}}{n s_{y_i} f_i} & 0 & -\frac{c_{y_i} \xi_i \sigma_{f_i}}{n s_{y_i}^2 f_i} & 0 \\ 0 & \frac{\xi_j \sigma_{f_j}}{n s_{y_j} f_j} & 0 & -\frac{c_{y_j} \xi_j \sigma_{f_j}}{n s_{y_j}^2 f_j} \end{bmatrix} = \begin{bmatrix} \frac{1}{n c_{y_i}} \frac{d\sigma}{d\Omega} y_i & 0 & -\frac{1}{n s_{y_i}} \frac{d\sigma}{d\Omega} y_i & 0 \\ 0 & \frac{1}{n c_{y_j}} \frac{d\sigma}{d\Omega} y_j & 0 & -\frac{1}{n s_{y_j}} \frac{d\sigma}{d\Omega} y_j \end{bmatrix}, \tag{4.34}$$

$$\mathbf{A_f} = \begin{bmatrix} -\frac{c_{x_i}\xi_i\sigma_{f_i}}{ns_{x_i}f_i^2} - \frac{c_{y_i}\xi_i\sigma_{f_i}}{ns_{y_i}f_i^2} & 0 \\ 0 & -\frac{c_{x_j}\xi_j\sigma_{f_j}}{ns_{x_j}f_j^2} - \frac{c_{y_j}\xi_j\sigma_{f_j}}{ns_{y_j}f_j^2} \end{bmatrix} = \begin{bmatrix} \frac{-1}{nf_i}\left(\frac{d\sigma}{d\Omega}_{x_i} + \frac{d\sigma}{d\Omega}_{y_i}\right) & 0 \\ 0 & \frac{-1}{nf_j}\left(\frac{d\sigma}{d\Omega}_{x_j} + \frac{d\sigma}{d\Omega}_{y_j}\right) \end{bmatrix}, \quad (4.35)$$

$$\mathbf{A}_\xi = \begin{bmatrix} \frac{c_{x_i}\sigma_{f_i}}{ns_{x_i}f_i} + \frac{c_{y_i}\sigma_{f_i}}{ns_{y_i}f_i} & 0 \\ 0 & \frac{c_{x_j}\sigma_{f_j}}{ns_{x_j}f_j} + \frac{c_{y_j}\sigma_{f_j}}{ns_{y_j}f_j} \end{bmatrix} = \begin{bmatrix} \frac{1}{n\xi_i}\left(\frac{d\sigma}{d\Omega}_{x_i} + \frac{d\sigma}{d\Omega}_{y_i}\right) & 0 \\ 0 & \frac{1}{n\xi_j}\left(\frac{d\sigma}{d\Omega}_{x_j} + \frac{d\sigma}{d\Omega}_{y_j}\right) \end{bmatrix}, \quad (4.36)$$

$$\mathbf{A}_{\sigma_\mathbf{f}} = \begin{bmatrix} \frac{c_{x_i}\xi_i}{ns_{x_i}f_i^2} + \frac{c_{y_i}\xi_i}{ns_{y_i}f_i^2} & 0 \\ 0 & \frac{c_{x_j}\xi_j}{ns_{x_j}f_j^2} + \frac{c_{y_j}\xi_j}{ns_{y_j}f_j^2} \end{bmatrix} = \begin{bmatrix} \frac{1}{n\sigma_{f_i}}\left(\frac{d\sigma}{d\Omega}_{x_i} + \frac{d\sigma}{d\Omega}_{y_i}\right) & 0 \\ 0 & \frac{1}{n\sigma_{f_j}}\left(\frac{d\sigma}{d\Omega}_{x_j} + \frac{d\sigma}{d\Omega}_{y_j}\right) \end{bmatrix}, \quad (4.37)$$

with the right-most matrices highlighting a simplification into already calculated differential angular cross section with $\mathbf{A}$ having dimensions of 2x14. The covariance matrix of the average differential angular cross section $\mathbf{K}_{\frac{\mathbf{d}\sigma}{\mathbf{d}\Omega}}$ can then be calculated to be

$$\mathbf{K}_{\frac{\mathbf{d}\sigma}{\mathbf{d}\Omega}} = \mathbf{K}_{\frac{\mathbf{d}\sigma}{\mathbf{d}\Omega\,\mathbf{x}}} + \mathbf{K}_{\frac{\mathbf{d}\sigma}{\mathbf{d}\Omega\,\mathbf{y}}} + \mathbf{K}_{\frac{\mathbf{d}\sigma}{\mathbf{d}\Omega\,\mathbf{f}}} + \mathbf{K}_{\frac{\mathbf{d}\sigma}{\mathbf{d}\Omega\,\xi}} + \mathbf{K}_{\frac{\mathbf{d}\sigma}{\mathbf{d}\Omega\,\sigma_\mathbf{f}}}, \quad (4.38)$$

which is a sum of individual component matrices of the x detector $\mathbf{K}_{\frac{\mathbf{d}\sigma}{\mathbf{d}\Omega\,\mathbf{x}}}$, the y detector $\mathbf{K}_{\frac{\mathbf{d}\sigma}{\mathbf{d}\Omega\,\mathbf{y}}}$, the counts in the flux $\mathbf{K}_{\frac{\mathbf{d}\sigma}{\mathbf{d}\Omega\,\mathbf{f}}}$, the PFNS of ^{252}Cf $\mathbf{K}_{\frac{\mathbf{d}\sigma}{\mathbf{d}\Omega\,\xi}}$, and the fission cross section of ^{235}U $\mathbf{K}_{\frac{\mathbf{d}\sigma}{\mathbf{d}\Omega\,\sigma_\mathbf{f}}}$. Each component matrix is defined respectively

$$\mathbf{K}_{\frac{\mathbf{d}\sigma}{\mathbf{d}\Omega\,\mathbf{x}}} = \begin{bmatrix} \frac{1}{n^2}\frac{d\sigma}{d\Omega}_{x_i}^2\left(\frac{\mathbf{Var}[c_{x_i}]}{c_{x_i}^2} + \frac{\mathbf{Var}[s_{x_i}]}{s_{x_i}^2}\right) & 0 \\ 0 & \frac{1}{n^2}\frac{d\sigma}{d\Omega}_{x_j}^2\left(\frac{\mathbf{Var}[c_{x_j}]}{c_{x_j}^2} + \frac{\mathbf{Var}[s_{x_j}]}{s_{x_j}^2}\right) \end{bmatrix}, \quad (4.39)$$

$$\mathbf{K}_{\frac{\mathbf{d}\sigma}{\mathbf{d}\Omega\,\mathbf{y}}} = \begin{bmatrix} \frac{1}{n^2}\frac{d\sigma}{d\Omega}_{y_i}^2\left(\frac{\mathbf{Var}[c_{y_i}]}{c_{y_i}^2} + \frac{\mathbf{Var}[s_{y_i}]}{s_{y_i}^2}\right) & 0 \\ 0 & \frac{1}{n^2}\frac{d\sigma}{d\Omega}_{y_j}^2\left(\frac{\mathbf{Var}[c_{y_j}]}{c_{y_j}^2} + \frac{\mathbf{Var}[s_{y_j}]}{s_{y_j}^2}\right) \end{bmatrix}, \quad (4.40)$$

$$\mathbf{K}_{\frac{\mathbf{d}\sigma}{\mathbf{d}\Omega\,\mathbf{f}}} = \begin{bmatrix} \frac{\mathbf{Var}[f_i]}{n^2 f_i^2}\left(\frac{d\sigma}{d\Omega}_{x_i} + \frac{d\sigma}{d\Omega}_{y_i}\right)^2 & 0 \\ 0 & \frac{\mathbf{Var}[f_j]}{n^2 f_j^2}\left(\frac{d\sigma}{d\Omega}_{x_j} + \frac{d\sigma}{d\Omega}_{y_j}\right)^2 \end{bmatrix}, \quad (4.41)$$

$$\mathbf{K}_{\frac{\mathbf{d}\sigma}{\mathbf{d}\Omega\,\xi}} = \begin{bmatrix} \frac{\mathbf{Var}[\xi_i]}{n^2\xi_i^2}\left(\frac{d\sigma}{d\Omega}_{x_i} + \frac{d\sigma}{d\Omega}_{y_i}\right)^2 & \frac{\mathbf{Cov}[\xi_{ij}]}{n^2\xi_i\xi_j}\left(\frac{d\sigma}{d\Omega}_{x_i} + \frac{d\sigma}{d\Omega}_{y_i}\right)\left(\frac{d\sigma}{d\Omega}_{x_j} + \frac{d\sigma}{d\Omega}_{y_j}\right) \\ \frac{\mathbf{Cov}[\xi_{ji}]}{n^2\xi_i\xi_j}\left(\frac{d\sigma}{d\Omega}_{x_i} + \frac{d\sigma}{d\Omega}_{y_i}\right)\left(\frac{d\sigma}{d\Omega}_{x_j} + \frac{d\sigma}{d\Omega}_{y_j}\right) & \frac{\mathbf{Var}[\xi_j]}{n^2\xi_j^2}\left(\frac{d\sigma}{d\Omega}_{x_j} + \frac{d\sigma}{d\Omega}_{y_j}\right)^2 \end{bmatrix}, \quad (4.42)$$

$$\mathbf{K}_{\overline{\frac{\mathbf{d}\sigma}{\mathbf{d}\Omega}}_{\sigma_\mathbf{f}}} = \begin{bmatrix} \frac{\mathbf{Var}[\sigma_{f_i}]}{n^2\sigma_{f_i}^2}\left(\frac{d\sigma}{d\Omega}_{x_i}+\frac{d\sigma}{d\Omega}_{y_i}\right)^2 & \frac{\mathbf{Cov}[\sigma_{f_{ij}}]}{n^2\sigma_{f_i}\sigma_{f_j}}\left(\frac{d\sigma}{d\Omega}_{x_i}+\frac{d\sigma}{d\Omega}_{y_i}\right)\left(\frac{d\sigma}{d\Omega}_{x_j}+\frac{d\sigma}{d\Omega}_{y_j}\right) \\ \frac{\mathbf{Cov}[\sigma_{f_{ij}}]}{n^2\sigma_{f_i}\sigma_{f_j}}\left(\frac{d\sigma}{d\Omega}_{x_i}+\frac{d\sigma}{d\Omega}_{y_i}\right)\left(\frac{d\sigma}{d\Omega}_{x_j}+\frac{d\sigma}{d\Omega}_{y_j}\right) & \frac{\mathbf{Var}[\sigma_{f_j}]}{n^2\sigma_{f_j}^2}\left(\frac{d\sigma}{d\Omega}_{x_j}+\frac{d\sigma}{d\Omega}_{y_j}\right)^2 \end{bmatrix}, \quad (4.43)$$

where once again, the off diagonal in the average differential angular cross section covariance $\mathbf{K}_{\overline{\frac{\mathbf{d}\sigma}{\mathbf{d}\Omega}}}$ contains the combined covariances of the ^{252}Cf PFNS and ^{235}U fission cross section as each detector shares the same neutron flux and each detector is referenced against the same ^{252}Cf PFNS standard and ^{235}U fission cross section. The simplified calculated covariance of $\overline{\frac{d\sigma}{d\Omega}}$ is

$$\begin{aligned} \mathbf{Cov}\left[\overline{\frac{d\sigma}{d\Omega}}_{ij}\right] = \delta_{ij}\Bigg[&\frac{1}{n^2}\frac{d\sigma}{d\Omega}_{x_i}^2\left(\frac{\mathbf{Var}[c_{x_i}]}{c_{x_i}^2}+\frac{\mathbf{Var}[s_{x_i}]}{s_{x_i}^2}\right)+ \\ &\frac{1}{n^2}\frac{d\sigma}{d\Omega}_{y_i}^2\left(\frac{\mathbf{Var}[c_{y_i}]}{c_{y_i}^2}+\frac{\mathbf{Var}[s_{y_i}]}{s_{y_i}^2}\right)+ \\ &\frac{\mathbf{Var}[f_i]}{n^2 f_i^2}\left(\frac{d\sigma}{d\Omega}_{x_i}+\frac{d\sigma}{d\Omega}_{y_i}\right)^2\Bigg]+ \\ &\frac{\mathbf{Cov}[\xi_{ji}]}{n^2\xi_i\xi_j}\left(\frac{d\sigma}{d\Omega}_{x_i}+\frac{d\sigma}{d\Omega}_{y_i}\right)\left(\frac{d\sigma}{d\Omega}_{x_j}+\frac{d\sigma}{d\Omega}_{y_j}\right)+ \\ &\frac{\mathbf{Cov}[\sigma_{f_{ij}}]}{n^2\sigma_{f_i}\sigma_{f_j}}\left(\frac{d\sigma}{d\Omega}_{x_i}+\frac{d\sigma}{d\Omega}_{y_i}\right)\left(\frac{d\sigma}{d\Omega}_{x_j}+\frac{d\sigma}{d\Omega}_{y_j}\right). \end{aligned} \quad (4.44)$$

It can be seen in the covariance matrix in Equation 4.38 and the simplified covariance in Equation 4.44 that the variance is of a form that is dependent on the sum of the individual counts (c, s, and f) along with the variance of the ^{252}Cf PFNS and the ^{235}U fission cross section. Similarly, the off diagonal in the calculated covariance matrix is dependent on the covariance of the ^{252}Cf PFNS and the ^{235}U fission cross section and is scaled by the square of the sum of the individual differential angular cross section divided by the number of detectors squared.

4.7 Integrated Cross Section

Finding the covariance matrix of the integrated cross section $\mathbf{K}_{\sigma(\mathbf{n},\mathbf{el})}$ will follow in a similar form and manner as calculating the covariance matrix of the average differential angular cross section in Section 4.6. A simplified example will be used once again to be able to see the pattern in the covariance matrix $\mathbf{K}_{\sigma(\mathbf{n},\mathbf{el})}$ easily. The calculation of the integrated

cross section for elastic scattering is calculated as

$$\sigma(n,\mathrm{el}) = \frac{\xi\sigma_f}{f}\left[\frac{\theta_1}{n}\left(\frac{c_x}{s_x}+\frac{c_y}{s_y}\right)+\frac{\theta_2}{m}\left(\frac{c_a}{s_a}+\frac{c_b}{s_b}\right)\right], \tag{4.45}$$

where θ_1 and θ_2 are the integration factors from Table 3.2 in Chapter 3, Section 3.7, n is the number of detectors related to θ_1 and similarly m is the number of detectors related to θ_2, x and y are individual detectors related to θ_1 while a and b are individual detectors related to θ_2, ξ is the value of the ^{252}Cf PFNS, σ_f is the fission cross section of ^{235}U, and f is the number of flux counts.

The covariance matrix $\mathbf{V}_{\sigma(\mathbf{n,el})}$ is constructed as

$$\mathbf{V}_{\sigma(\mathbf{n,el})} = \begin{bmatrix} \mathbf{V}_{\theta_1} & 0 & 0 \\ 0 & \mathbf{V}_{\theta_2} & 0 \\ 0 & 0 & \mathbf{V_O} \end{bmatrix}, \tag{4.46}$$

where the sub matrix of covariances related to the θ_1 term is given by $\mathbf{V}_{\theta_1}$, the sub matrix of covariances related to θ_2 term is given by $\mathbf{V}_{\theta_2}$, and the sub matrix containing the flux counts, ^{252}Cf PFNS, and fission cross section of ^{235}U is given by $\mathbf{V_O}$

$$\mathbf{V}_{\theta_1} = \begin{bmatrix} \mathbf{Var}[c_{x_i}] & 0 & 0 & 0 & 0 & 0 & 0 & 0 \\ 0 & \mathbf{Var}[c_{x_j}] & 0 & 0 & 0 & 0 & 0 & 0 \\ 0 & 0 & \mathbf{Var}[s_{x_i}] & 0 & 0 & 0 & 0 & 0 \\ 0 & 0 & 0 & \mathbf{Var}[s_{x_j}] & 0 & 0 & 0 & 0 \\ 0 & 0 & 0 & 0 & \mathbf{Var}[c_{y_i}] & 0 & 0 & 0 \\ 0 & 0 & 0 & 0 & 0 & \mathbf{Var}[c_{y_j}] & 0 & 0 \\ 0 & 0 & 0 & 0 & 0 & 0 & \mathbf{Var}[s_{y_i}] & 0 \\ 0 & 0 & 0 & 0 & 0 & 0 & 0 & \mathbf{Var}[s_{y_j}] \end{bmatrix}, \tag{4.47}$$

$$\mathbf{V}_{\theta_2} = \begin{bmatrix} \mathbf{Var}[c_{a_i}] & 0 & 0 & 0 & 0 & 0 & 0 & 0 \\ 0 & \mathbf{Var}[c_{a_j}] & 0 & 0 & 0 & 0 & 0 & 0 \\ 0 & 0 & \mathbf{Var}[s_{a_i}] & 0 & 0 & 0 & 0 & 0 \\ 0 & 0 & 0 & \mathbf{Var}[s_{a_j}] & 0 & 0 & 0 & 0 \\ 0 & 0 & 0 & 0 & \mathbf{Var}[c_{b_i}] & 0 & 0 & 0 \\ 0 & 0 & 0 & 0 & 0 & \mathbf{Var}[c_{b_j}] & 0 & 0 \\ 0 & 0 & 0 & 0 & 0 & 0 & \mathbf{Var}[s_{b_i}] & 0 \\ 0 & 0 & 0 & 0 & 0 & 0 & 0 & \mathbf{Var}[s_{b_j}] \end{bmatrix}, \tag{4.48}$$

$$\mathbf{V_O} = \begin{bmatrix} \mathbf{Var}[f_i] & 0 & 0 & 0 & 0 & 0 \\ 0 & \mathbf{Var}[f_j] & 0 & 0 & 0 & 0 \\ 0 & 0 & \mathbf{Var}[\xi_i] & \mathbf{Cov}[\xi_{ij}] & 0 & 0 \\ 0 & 0 & \mathbf{Cov}[\xi_{ji}] & \mathbf{Var}[\xi_j] & 0 & 0 \\ 0 & 0 & 0 & 0 & \mathbf{Var}[\sigma_{f_i}] & \mathbf{Cov}[\sigma_{f_{ij}}] \\ 0 & 0 & 0 & 0 & \mathbf{Cov}[\sigma_{f_{ji}}] & \mathbf{Var}[\sigma_{f_j}] \end{bmatrix}, \tag{4.49}$$

where the dimension of the covariance matrix $\mathbf{V}_{\sigma(\mathbf{n},\mathbf{el})}$ is 22x22. The sensitivity matrix $\mathbf{A}_{\sigma(\mathbf{n},\mathbf{el})}$ is given by (with simplification of terms using the differential angular cross section when appropriate $\frac{c\xi\sigma_f}{sf} = \frac{d\sigma}{d\Omega}$)

$$\mathbf{A}_{\sigma(\mathbf{n},\mathbf{el})} = \left[\mathbf{A}_{\theta_1} + \mathbf{A}_{\theta_2} + \mathbf{A_f} + \mathbf{A}_{\xi} + \mathbf{A}_{\sigma_\mathbf{f}} \right], \tag{4.50}$$

where $\mathbf{A}_{\theta_1}$ is the sensitivity matrix for the quantities related to θ_1, $\mathbf{A}_{\theta_2}$ is the sensitivity matrix for the quantities related to θ_2, $\mathbf{A_f}$ is the sensitivity matrix with respect to the flux counts, $\mathbf{A}_{\xi}$ is the sensitivity matrix with respect the ^{252}Cf PFNS, and $\mathbf{A}_{\sigma_\mathbf{f}}$ is the sensitivity matrix for the fission cross section of ^{235}U. Each sensitivity matrix is given by

$$\mathbf{A}_{\theta_1} = \begin{bmatrix} \frac{\theta_1}{nc_{x_i}}\frac{d\sigma}{d\Omega}x_i & 0 & \frac{-\theta_1}{ns_{x_i}}\frac{d\sigma}{d\Omega}x_i & 0 & \frac{\theta_1}{nc_{y_i}}\frac{d\sigma}{d\Omega}y_i & 0 & \frac{-\theta_1}{ns_{y_i}}\frac{d\sigma}{d\Omega}y_i & 0 \\ 0 & \frac{\theta_1}{nc_{x_j}}\frac{d\sigma}{d\Omega}x_j & 0 & \frac{-\theta_1}{ns_{x_j}}\frac{d\sigma}{d\Omega}x_j & 0 & \frac{\theta_1}{nc_{y_j}}\frac{d\sigma}{d\Omega}y_j & 0 & \frac{-\theta_1}{ns_{y_j}}\frac{d\sigma}{d\Omega}y_j \end{bmatrix}, \tag{4.51}$$

$$\mathbf{A_{\theta_2}} = \begin{bmatrix} \frac{\theta_2}{mc_{a_i}}\frac{d\sigma}{d\Omega}a_i & 0 & \frac{-\theta_2}{ms_{a_i}}\frac{d\sigma}{d\Omega}a_i & 0 & \frac{\theta_2}{mc_{b_i}}\frac{d\sigma}{d\Omega}b_i & 0 & \frac{-\theta_2}{ms_{b_i}}\frac{d\sigma}{d\Omega}b_i & 0 \\ 0 & \frac{\theta_2}{mc_{a_j}}\frac{d\sigma}{d\Omega}a_j & 0 & \frac{-\theta_2}{ms_{a_j}}\frac{d\sigma}{d\Omega}a_j & 0 & \frac{\theta_2}{mc_{b_j}}\frac{d\sigma}{d\Omega}b_j & 0 & \frac{-\theta_2}{ms_{b_j}}\frac{d\sigma}{d\Omega}b_j \end{bmatrix}, \tag{4.52}$$

$$\mathbf{A_f} = \begin{bmatrix} \frac{-\theta_1}{nf_i}\left(\frac{d\sigma}{d\Omega}x_i + \frac{d\sigma}{d\Omega}y_i\right) + \frac{-\theta_2}{mf_i}\left(\frac{d\sigma}{d\Omega}a_i + \frac{d\sigma}{d\Omega}b_i\right) & 0 \\ 0 & \frac{-\theta_1}{nf_j}\left(\frac{d\sigma}{d\Omega}x_j + \frac{d\sigma}{d\Omega}y_j\right) + \frac{-\theta_2}{mf_j}\left(\frac{d\sigma}{d\Omega}a_j + \frac{d\sigma}{d\Omega}b_j\right) \end{bmatrix}, \tag{4.53}$$

$$\mathbf{A_\xi} = \begin{bmatrix} \frac{\theta_1}{n\xi_i}\left(\frac{d\sigma}{d\Omega}x_i + \frac{d\sigma}{d\Omega}y_i\right) + \frac{\theta_2}{m\xi_i}\left(\frac{d\sigma}{d\Omega}a_i + \frac{d\sigma}{d\Omega}b_i\right) & 0 \\ 0 & \frac{\theta_1}{n\xi_j}\left(\frac{d\sigma}{d\Omega}x_j + \frac{d\sigma}{d\Omega}y_j\right) + \frac{\theta_2}{m\xi_j}\left(\frac{d\sigma}{d\Omega}a_j + \frac{d\sigma}{d\Omega}b_j\right) \end{bmatrix}, \tag{4.54}$$

$$\mathbf{A_{\sigma_f}} = \begin{bmatrix} \frac{\theta_1}{n\sigma_{f_i}}\left(\frac{d\sigma}{d\Omega}x_i + \frac{d\sigma}{d\Omega}y_i\right) + \frac{\theta_2}{m\sigma_{f_i}}\left(\frac{d\sigma}{d\Omega}a_i + \frac{d\sigma}{d\Omega}b_i\right) & 0 \\ 0 & \frac{\theta_1}{n\sigma_{f_j}}\left(\frac{d\sigma}{d\Omega}x_j + \frac{d\sigma}{d\Omega}y_j\right) + \frac{\theta_2}{m\sigma_{f_j}}\left(\frac{d\sigma}{d\Omega}a_j + \frac{d\sigma}{d\Omega}b_j\right) \end{bmatrix}, \tag{4.55}$$

where similar to Equations 4.33, 4.34, 4.35, 4.36, 4.37, there is a dependence on the individual differential angular cross sections, with the added integration factor. The covariance matrix for the integrated cross section $\mathbf{K_{\sigma(n,el)}}$ is calculated to be

$$\mathbf{K_{\sigma(n,el)}} = \mathbf{K_{\theta_1}} + \mathbf{K_{\theta_2}} + \mathbf{K_f} + \mathbf{K_\xi} + \mathbf{K_{\sigma_f}}\,, \tag{4.56}$$

where the submatrix $\mathbf{K_{\theta_1}}$ pertaining to θ_1 is given by

$$\mathbf{K_{\theta_1}} = \begin{bmatrix} \mathbf{D_{\theta_{1i}}} & 0 \\ 0 & \mathbf{D_{\theta_{1j}}} \end{bmatrix}, \tag{4.57}$$

where the diagonal components $\mathbf{D_{\theta_{1k}}}$ with energy index $k = i$ or j given by

$$\mathbf{D_{\theta_{1k}}} = \frac{\theta_1^2}{n^2}\left[\frac{d\sigma}{d\Omega}^2_{x_k}\left(\frac{\mathbf{Var}[c_{x_k}]}{c_{x_k}^2} + \frac{\mathbf{Var}[s_{x_k}]}{s_{x_k}^2}\right) + \frac{d\sigma}{d\Omega}^2_{y_k}\left(\frac{\mathbf{Var}[c_{y_k}]}{c_{y_k}^2} + \frac{\mathbf{Var}[s_{y_k}]}{s_{y_k}^2}\right)\right]. \tag{4.58}$$

Similarly, for quantities related to θ_2

$$\mathbf{K_{\theta_2}} = \begin{bmatrix} \mathbf{D_{\theta_{2i}}} & 0 \\ 0 & \mathbf{D_{\theta_{2j}}} \end{bmatrix}, \tag{4.59}$$

with

$$\mathbf{D_{\theta_{2k}}} = \frac{\theta_2^2}{m^2}\left[\frac{d\sigma}{d\Omega}^2_{a_k}\left(\frac{\mathbf{Var}[c_{a_k}]}{c_{a_k}^2}+\frac{\mathbf{Var}[s_{a_k}]}{s_{a_k}^2}\right)+\frac{d\sigma}{d\Omega}^2_{b_k}\left(\frac{\mathbf{Var}[c_{b_k}]}{c_{b_k}^2}+\frac{\mathbf{Var}[s_{b_k}]}{s_{b_k}^2}\right)\right]. \tag{4.60}$$

For quantities related to the flux counts f

$$\mathbf{K_f} = \begin{bmatrix}\mathbf{D_{f_i}} & 0\\ 0 & \mathbf{D_{f_j}}\end{bmatrix}, \tag{4.61}$$

with

$$\mathbf{D_{f_k}} = \left[\frac{\theta_1}{n}\left(\frac{d\sigma}{d\Omega}_{x_k}+\frac{d\sigma}{d\Omega}_{y_k}\right)+\frac{\theta_2}{m}\left(\frac{d\sigma}{d\Omega}_{a_k}+\frac{d\sigma}{d\Omega}_{b_k}\right)\right]^2\frac{\mathbf{Var}[f_k]}{f_k^2}. \tag{4.62}$$

Quantities related to the ^{252}Cf PFNS ξ can be expressed as

$$\mathbf{K}_\xi = \begin{bmatrix}\mathbf{D}_{\xi_i} & \mathbf{C}_{\xi_{ij}}\\ \mathbf{C}_{\xi_{ji}} & \mathbf{D}_{\xi_j}\end{bmatrix}, \tag{4.63}$$

where the diagonal (variance) $\mathbf{D}_{\xi_k}$ and the off diagonal (covariance) $\mathbf{C}_{\xi_{ij}}$ is given by

$$\mathbf{D}_{\xi_k} = \left[\frac{\theta_1}{n}\left(\frac{d\sigma}{d\Omega}_{x_k}+\frac{d\sigma}{d\Omega}_{y_k}\right)+\frac{\theta_2}{m}\left(\frac{d\sigma}{d\Omega}_{a_k}+\frac{d\sigma}{d\Omega}_{b_k}\right)\right]^2\frac{\mathbf{Var}[\xi_k]}{\xi_k^2}, \tag{4.64}$$

and

$$\begin{aligned}\mathbf{C}_{\xi_{ij}} = \mathbf{C}_{\xi_{ji}} = \frac{\mathbf{Cov}[\xi_{ij}]}{\xi_i\xi_j} * \left[\frac{\theta_1}{n}\left(\frac{d\sigma}{d\Omega}_{x_i}+\frac{d\sigma}{d\Omega}_{y_i}\right)+\frac{\theta_2}{m}\left(\frac{d\sigma}{d\Omega}_{a_i}+\frac{d\sigma}{d\Omega}_{b_i}\right)\right] * \\ \left[\frac{\theta_1}{n}\left(\frac{d\sigma}{d\Omega}_{x_j}+\frac{d\sigma}{d\Omega}_{y_j}\right)+\frac{\theta_2}{m}\left(\frac{d\sigma}{d\Omega}_{a_j}+\frac{d\sigma}{d\Omega}_{b_j}\right)\right].\end{aligned} \tag{4.65}$$

Quantities related to the ^{235}U PFNS σ_f can be expressed as

$$\mathbf{K}_{\sigma_f} = \begin{bmatrix}\mathbf{D}_{\sigma_{f_i}} & \mathbf{C}_{\sigma_{f_{ij}}}\\ \mathbf{C}_{\sigma_{f_{ji}}} & \mathbf{D}_{\sigma_{f_j}}\end{bmatrix}, \tag{4.66}$$

where the diagonal (variance) $\mathbf{D}_{\sigma_{f_k}}$ and the off diagonal (covariance) $\mathbf{C}_{\sigma_{f_{ij}}}$ is given by

$$\mathbf{D}_{\sigma_{f_k}} = \left[\frac{\theta_1}{n}\left(\frac{d\sigma}{d\Omega}_{x_k}+\frac{d\sigma}{d\Omega}_{y_k}\right)+\frac{\theta_2}{m}\left(\frac{d\sigma}{d\Omega}_{a_k}+\frac{d\sigma}{d\Omega}_{b_k}\right)\right]^2\frac{\mathbf{Var}[\sigma_{f_k}]}{\sigma_{f_k}^2}, \tag{4.67}$$

and

$$\begin{aligned}\mathbf{C}_{\sigma_{f_{ij}}} = \mathbf{C}_{\sigma_{f_{ji}}} = \frac{\mathbf{Cov}[\sigma_{f_{ij}}]}{\sigma_{f_i}\sigma_{f_j}} * \left[\frac{\theta_1}{n}\left(\frac{d\sigma}{d\Omega}_{x_i}+\frac{d\sigma}{d\Omega}_{y_i}\right)+\frac{\theta_2}{m}\left(\frac{d\sigma}{d\Omega}_{a_i}+\frac{d\sigma}{d\Omega}_{b_i}\right)\right] * \\ \left[\frac{\theta_1}{n}\left(\frac{d\sigma}{d\Omega}_{x_j}+\frac{d\sigma}{d\Omega}_{y_j}\right)+\frac{\theta_2}{m}\left(\frac{d\sigma}{d\Omega}_{a_j}+\frac{d\sigma}{d\Omega}_{b_j}\right)\right].\end{aligned} \tag{4.68}$$

The generalized covariance of the integrated cross section $\mathbf{Cov}[\sigma(n,\mathrm{el})]$ can be expressed as

$$
\begin{aligned}
&\mathbf{Cov}[\sigma(n,\mathrm{el})_{ij}] = \\
&\delta_{ij}\left\{\frac{\theta_1^2}{n^2}\left[\frac{d\sigma}{d\Omega_{x_k}}^2\left(\frac{\mathbf{Var}[c_{x_k}]}{c_{x_k}^2}+\frac{\mathbf{Var}[s_{x_k}]}{s_{x_k}^2}\right)+\frac{d\sigma}{d\Omega_{y_k}}^2\left(\frac{\mathbf{Var}[c_{y_k}]}{c_{y_k}^2}+\frac{\mathbf{Var}[s_{y_k}]}{s_{y_k}^2}\right)\right]+\right. \\
&\frac{\theta_2^2}{m^2}\left[\frac{d\sigma}{d\Omega_{a_k}}^2\left(\frac{\mathbf{Var}[c_{a_k}]}{c_{a_k}^2}+\frac{\mathbf{Var}[s_{a_k}]}{s_{a_k}^2}\right)+\frac{d\sigma}{d\Omega_{b_k}}^2\left(\frac{\mathbf{Var}[c_{b_k}]}{c_{b_k}^2}+\frac{\mathbf{Var}[s_{b_k}]}{s_{b_k}^2}\right)\right]+ \\
&\left.\left[\frac{\theta_1}{n}\left(\frac{d\sigma}{d\Omega_{x_k}}+\frac{d\sigma}{d\Omega_{y_k}}\right)+\frac{\theta_2}{m}\left(\frac{d\sigma}{d\Omega_{a_k}}+\frac{d\sigma}{d\Omega_{b_k}}\right)\right]^2\frac{\mathbf{Var}[f_k]}{f_k^2}\right\}+ \\
&\frac{\mathbf{Cov}[\xi_{ij}]}{\xi_i\xi_j}*\left[\frac{\theta_1}{n}\left(\frac{d\sigma}{d\Omega_{x_i}}+\frac{d\sigma}{d\Omega_{y_i}}\right)+\frac{\theta_2}{m}\left(\frac{d\sigma}{d\Omega_{a_i}}+\frac{d\sigma}{d\Omega_{b_i}}\right)\right]* \\
&\left[\frac{\theta_1}{n}\left(\frac{d\sigma}{d\Omega_{x_j}}+\frac{d\sigma}{d\Omega_{y_j}}\right)+\frac{\theta_2}{m}\left(\frac{d\sigma}{d\Omega_{a_j}}+\frac{d\sigma}{d\Omega_{b_j}}\right)\right]+ \\
&\frac{\mathbf{Cov}[\sigma_{f_{ij}}]}{\sigma_{f_i}\sigma_{f_j}}*\left[\frac{\theta_1}{n}\left(\frac{d\sigma}{d\Omega_{x_i}}+\frac{d\sigma}{d\Omega_{y_i}}\right)+\frac{\theta_2}{m}\left(\frac{d\sigma}{d\Omega_{a_i}}+\frac{d\sigma}{d\Omega_{b_i}}\right)\right]* \\
&\left[\frac{\theta_1}{n}\left(\frac{d\sigma}{d\Omega_{x_j}}+\frac{d\sigma}{d\Omega_{y_j}}\right)+\frac{\theta_2}{m}\left(\frac{d\sigma}{d\Omega_{a_j}}+\frac{d\sigma}{d\Omega_{b_j}}\right)\right],
\end{aligned}
\tag{4.69}
$$

where the pattern becomes clear with the generalized form being shown in Equation 4.70 as a sum over each θ where it is implied that n will change with the respective number of detectors (x, y correspond to θ_1 for example) for a given θ

$$
\begin{aligned}
&\mathbf{Cov}[\sigma(n,\mathrm{el})_{ij}] = \\
&\delta_{ij}\left\{\sum_\theta\left(\frac{\theta^2}{n^2}\left[\frac{d\sigma}{d\Omega_{x_k}}^2\left(\frac{\mathbf{Var}[c_{x_k}]}{c_{x_k}^2}+\frac{\mathbf{Var}[s_{x_k}]}{s_{x_k}^2}\right)+\frac{d\sigma}{d\Omega_{y_k}}^2\left(\frac{\mathbf{Var}[c_{y_k}]}{c_{y_k}^2}+\frac{\mathbf{Var}[s_{y_k}]}{s_{y_k}^2}\right)\right]\right)+\right. \\
&\left.\left(\sum_\theta\left[\frac{\theta}{n}\left(\frac{d\sigma}{d\Omega_{x_k}}+\frac{d\sigma}{d\Omega_{y_k}}\right)\right]\right)^2\frac{\mathbf{Var}[f_k]}{f_k^2}\right\}+ \\
&\left(\frac{\mathbf{Cov}[\xi_{ij}]}{\xi_i\xi_j}+\frac{\mathbf{Cov}[\sigma_{f_{ij}}]}{\sigma_{f_i}\sigma_{f_j}}\right)\left(\sum_\theta\left[\frac{\theta}{n}\left(\frac{d\sigma}{d\Omega_{x_i}}+\frac{d\sigma}{d\Omega_{y_i}}\right)\right]*\sum_\theta\left[\frac{\theta}{n}\left(\frac{d\sigma}{d\Omega_{x_j}}+\frac{d\sigma}{d\Omega_{y_j}}\right)\right]\right).
\end{aligned}
\tag{4.70}
$$

The resulting covariance for the integrated cross section is a scaled of the number of detectors that are used. For the covariance terms in Equation 4.69, it can be seen that the covariance of the ^{252}Cf PFNS and ^{235}U fission cross section get scaled by the average differential angular cross section multiplied by the square of the integration factor.

The final range of the calculated uncertainties of the integrated cross section, as given by Equation 4.70, and the respective relative uncertainty is given in Table 4.1 over the incident neutron energy range of $E_n^{inc} = 0.85$ – 7 MeV.

Quantity Uncertainty	Min. Value	Max Value
Scaled Integrated Cross Section (barns)	0.00703902	0.0262674
Relative (%)	2.14572	6.49204

Table 4.1 The calculated uncertainties of the measured integrated cross section over the incident neutron energy range of $E_n^{inc} = 0.85$ – 7 MeV.

4.8 Correlation Matrix

The correlation matrix for the integrated cross section $\sigma(n, \mathrm{el})$ is calculated to show the relationship between data points on a scale of -1 (anti correlated) to +1 (correlated). The correlation matrix $\mathbf{Corr}[\sigma(n, \mathrm{el})]$ is simply calculated by taking the value of the covariance matrix at energy point i and j and is divided by the square root of the variance at energy point i and j. Explicitly, this is calculated as

$$\mathbf{Corr}[\sigma(n, \mathrm{el})_{ij}] = \frac{\mathbf{Cov}[\sigma(n, \mathrm{el})_{ij}]}{\sqrt{\mathbf{Var}[\sigma(n, \mathrm{el})_i]\mathbf{Var}[\sigma(n, \mathrm{el})_j]}}\,, \tag{4.71}$$

where it can be see that when the indices are equal ($i = j$) that the expression in Equation 4.71 is equal to 1 given the fact that the covariance on the diagonal is equal to the variance.

The covariance matrix and correlation matrix for the integrate cross section $\sigma(n, \mathrm{el})$ are presented in Chapter 5 along with other results.

CHAPTER 5

RESULTS & DISCUSSION

In this chapter the integrated cross section of carbon elastic scattering ^{12}C(n, el), the differential angular cross section $\frac{d\sigma}{d\Omega}$ as a function of neutron incident energy E_n^{inc}, and the differential angular cross section as a function of CM (center-of-mass) scattering angle $\tilde{\theta}_n$ (angular distributions) are all presented. All results will be plotted on an incident neutron energy E_n^{inc} range of 0.85 – 7 MeV unless otherwise stated.

5.1 ENDF-B/VIII.0 Cross Sections

The recorded and analyzed data should be compared with the existing evaluation for ^{12}C elastic scattering cross section in order to see consistencies or divergence. ENDF-B/VIII.0 [13] provides the needed comparison, as one intention for the reported data in this work is to provide experimental data for evaluators when reviewing the elastic scattering evaluation of ^{12}C. The neutron elastic scattering cross section of ^{12}C, from the ENDF-B/VIII.0 edition of the evaluation, is shown in Figure 5.1 with the data being provided by Ref. [40]. It is worth mentioning that the latest edition of the ENDF evaluation is ENDF-B/VIII.I, but the ^{12}C is identical to version VIII.0 and version VIII.I does not yet have a published citation.

It is not possible to obtain complete coverage around the carbon target (4π solid angle) due to the physical constraints of the detector size, the needed space for the neutron beam to enter and exit the detector array, along with the desire to minimize background/environmental scattered neutrons. As such, the evaluation (Figure 5.1) can be used to calculate the theoretical ENDF-B/VIII.0 ^{12}C (n, el) cross section as would be observed by the geometry of the liquid scintillators in the CoGNAC setup.

ENDF-B/VIII.0 provides differential angular cross sections in the evaluation file via Legendre polynomial coefficients a_ℓ (found in Ref. [73]) across the incident neutron energy range of 10 μeV – 20 MeV. To produce a differential angular cross section $\frac{d\sigma}{d\Omega}$ using the evaluation,

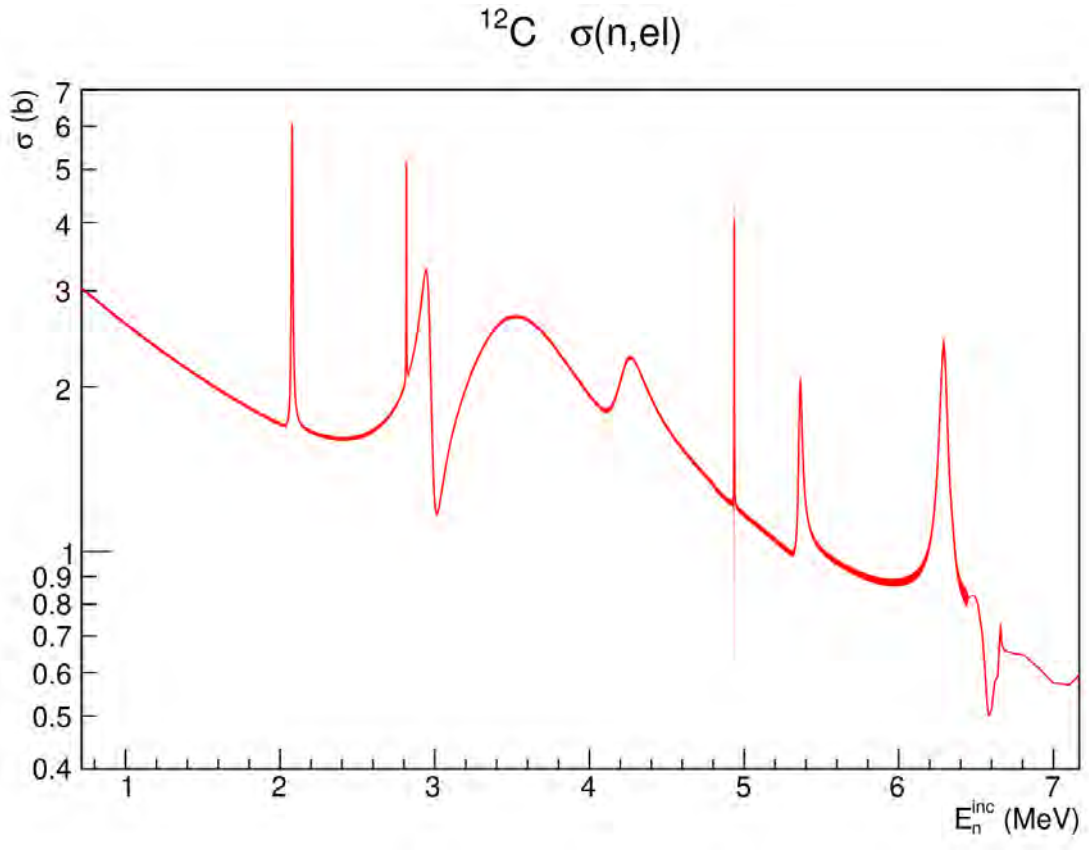

Figure 5.1 The ^{12}C neutron elastic scattering cross section, with uncertainty bands, obtained from ENDF-B/VIII.0 with data points from Ref. [40].

the following equation is used as provided by the ENDF-6 Formats Manual [74]

$$\frac{d\sigma}{d\Omega}\left(\tilde{\theta}_n, E_n^{inc}\right) = \frac{\sigma(n,\mathrm{el})}{2\pi}\sum_{l=0}^{N_\ell}\frac{2\ell+1}{2}a_\ell(E_n^{inc})P_\ell(\cos\tilde{\theta}_n)\,. \tag{5.1}$$

Here, $\tilde{\theta}_n$ is the neutron scattering angle in the CM frame, E_n^{inc} is the incident neutron energy, $\sigma(n,\mathrm{el})$ is the integrated neutron elastic scattering cross section (in this case, ^{12}C as shown in Figure 5.1), ℓ is the order of the Legendre polynomial, N_ℓ is the highest order with $N_\ell = 8$ for ^{12}C(n,el), a_ℓ is the Legendre coefficient provided by Ref. [73] in the CM frame, and P_ℓ is the Legendre polynomial term as a function of the cosine of the CM scattering angle. An example of the differential angular cross section is shown in Figure 5.2 for $\theta_n = 120°$.

In order to produce differential angular cross sections for comparisons with the data, a scattering angle θ_n in the lab frame, which is the same as the detector angle θ_d, is converted into the appropriate CM scattering angle $\tilde{\theta}_n = \tilde{\theta}_d$ based on the E_n^{inc} value. An example

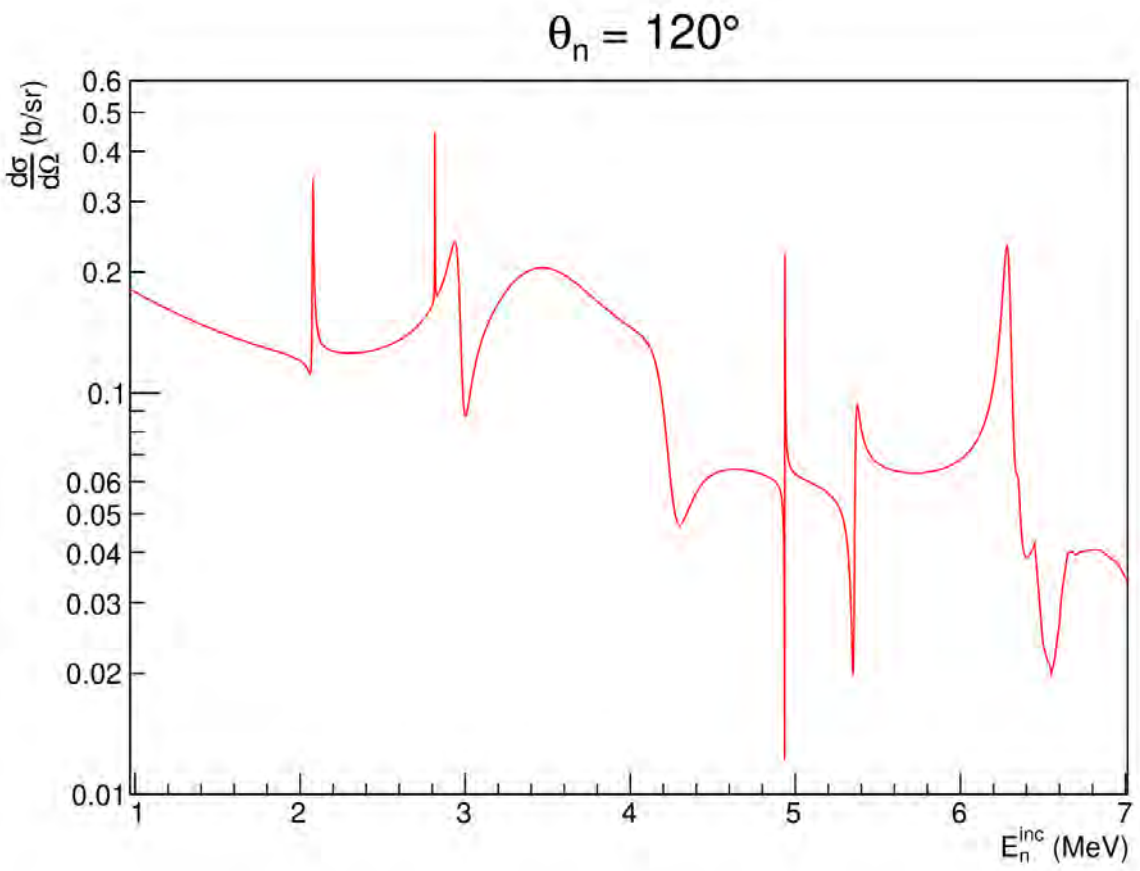

Figure 5.2 The differential angular cross section of neutron elastic scattering at a lab scattering angle of $\theta_n = 120°$.

relationship between the lab scattered angle and the same angle in the CM frame as a function of E_n^{inc} is shown in Figure 5.3.

The conversion of the lab scattering angle, that is dependent upon the location of the detector, into a CM scattering angle is due to the fact that the Legendre polynomials that are reported in Ref. [73] for the differential angular cross section are given in the CM frame. The calculated $\tilde{\theta}_n$ is then inserted into the the cosine term of Equation 5.1 to produce a Legendre polynomial that is then summed over all ℓ values and produces the resulting differential angular cross section seen in Figure 5.2 for the lab frame. The differential angular cross section is in the lab frame because θ_n is fixed causing $\widetilde{\theta}_n$ to vary over E_n^{inc}.

If Equation 5.1 is used to calculate the differential angular cross sections in successive small θ_n intervals one can integrate over the full solid angle of 4π: 0-180° in θ_n (2 radians) and

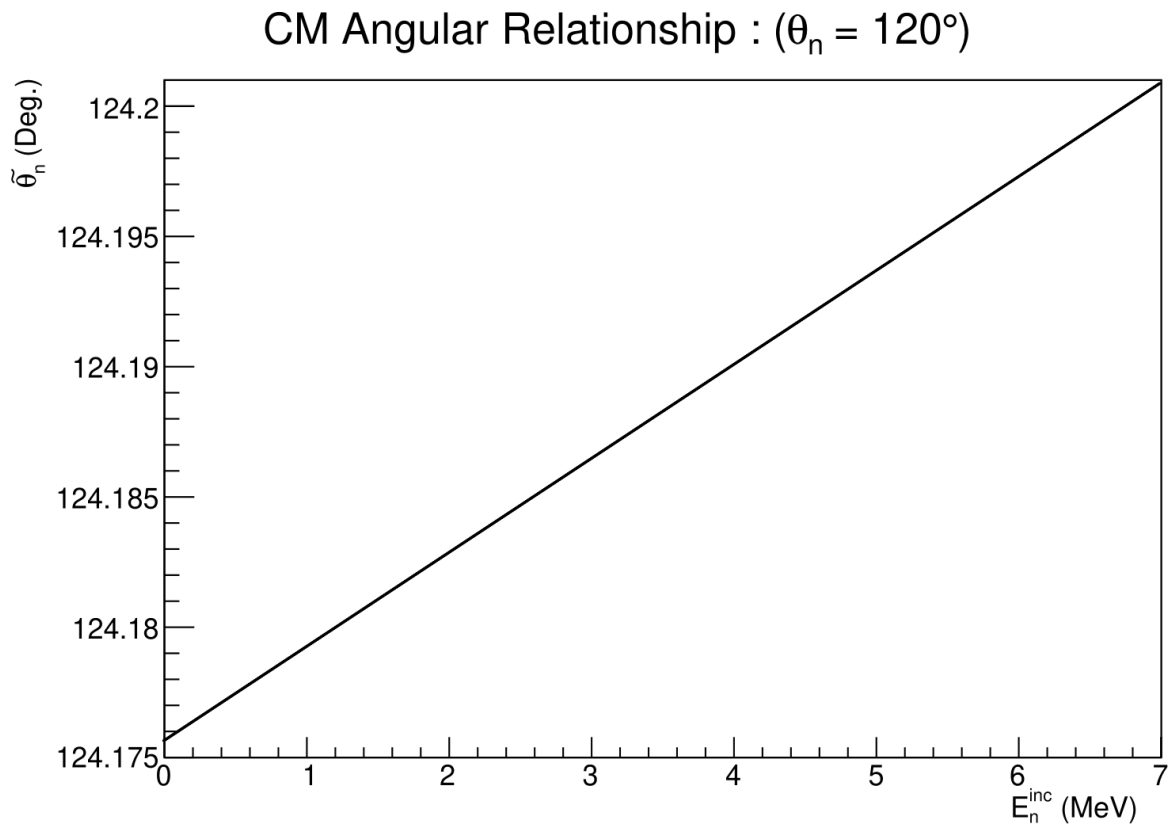

Figure 5.3 Relationship between lab scattering angle θ_n to CM scattering angle $\tilde{\theta}_n$ as a function of the neutron incident energy E_n^{inc}.

2π radians in φ with the assumption that neutrons scatter symmetrically in the azimuthal direction [74], and recover the full integrated cross section as seen in Figure 5.1.

Utilizing Equation 5.1 over the angular coverage that the liquid scintillators spans from the central angle $\theta_n \pm 5^\circ$ and in φ, which each θ value spanning a different range of angles for φ based on the geometric relationships described in Chapter 3, Section 3.7, Figure 3.25, it is possible to derive an integrated cross section based on the ENDF-B/VIII.0 evaluation for an elastically scattered neutron incorporating the geometry and resolution of the CoGNAC liquid scintillator array. This integrated cross section is shown in Figure 5.4 and is what the analyzed data are compared with.

As can be seen in Figure 5.4, the order of magnitude is reduced from the evaluation as not all angles are covered by the liquid scintillators. As such, only a subset of the full angular range in θ and φ are covered. Additionally, structures in the evaluation are reduced in

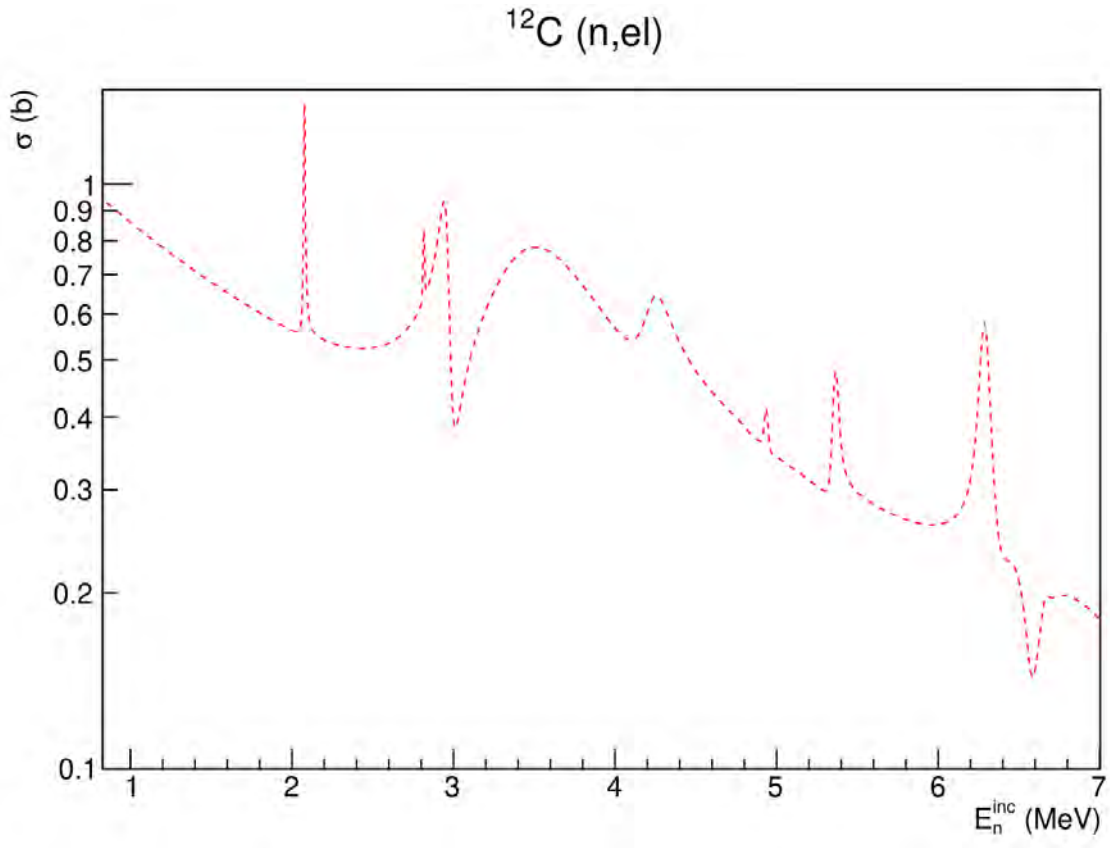

Figure 5.4 The derived integrated neutron elastic scattering cross section as observed by the CoGNAC setup using the liquid scintillators using ENDF-B/VIII.0 and accounting for detector resolution, in dashed red.

magnitude such as the peaks near 2.1 MeV, 2.8 MeV, and just below 5 MeV. This arises from introducing the detector resolution when deriving the neutron elastic scattering integrated cross section.

5.2 Integrated Cross Section

Given the analysis method and uncertainty quantification discussed in Chapters 3 and 4 respectively, and presenting the ENDF-B/VIII.0 evaluation accounting for the geometry and resolution of the CoGNAC setup, it is now possible to present the measured integrated cross section compared with the evaluation along with relative uncertainties and the corresponding correlation and covariance matrix. The measured integrated cross section is shown in Figure 5.5, the relative uncertainty of the measurement is shown in Figure 5.6, and the correlation and covariance matrices are shown in Figure 5.7 and Figure 5.8, respectively.

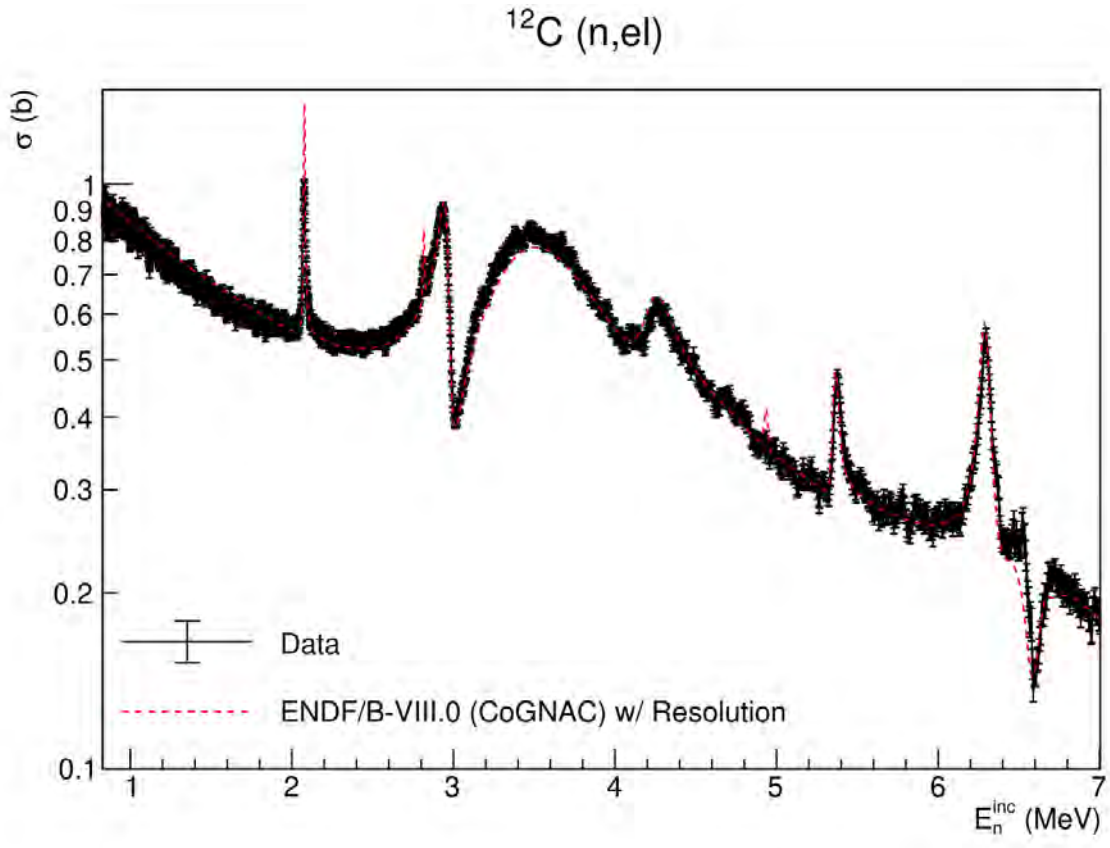

Figure 5.5 The measured integrated neutron elastic scattering cross section of ^{12}C (black) compared wtih the calculated integrated cross section using ENDF-B/VIII.0 for the CoGNAC setup (dashed red).

The measured integrated cross section presented in Figure 5.5, is scaled to the derived integrated cross section at 1.8 MeV due to the fact that the carbon elastic scattering cross section is a standard from 10 eV to 1.8 MeV. The scaled factor used is 0.00961096 which accounts for parameters such as number of target nuclei, flux magnitude, beam density, beam diameter, etc. There is good agreement with the ENDF-B/VIII.0 evaluation that is derived in comparison with the measured data. Additionally, the trend of the data in the standard region, 0.85 – 1.8 MeV for the reported data, agrees with evaluation. The measured cross section also follows the structures seen in the evaluation and is in good agreement with respect to magnitude and overall trend as E_n^{inc} increases.

The only major point of difference between the data and evaluation is at the peak in the evaluation just below 5 MeV. The only known dataset on EXFOR that reports measurement

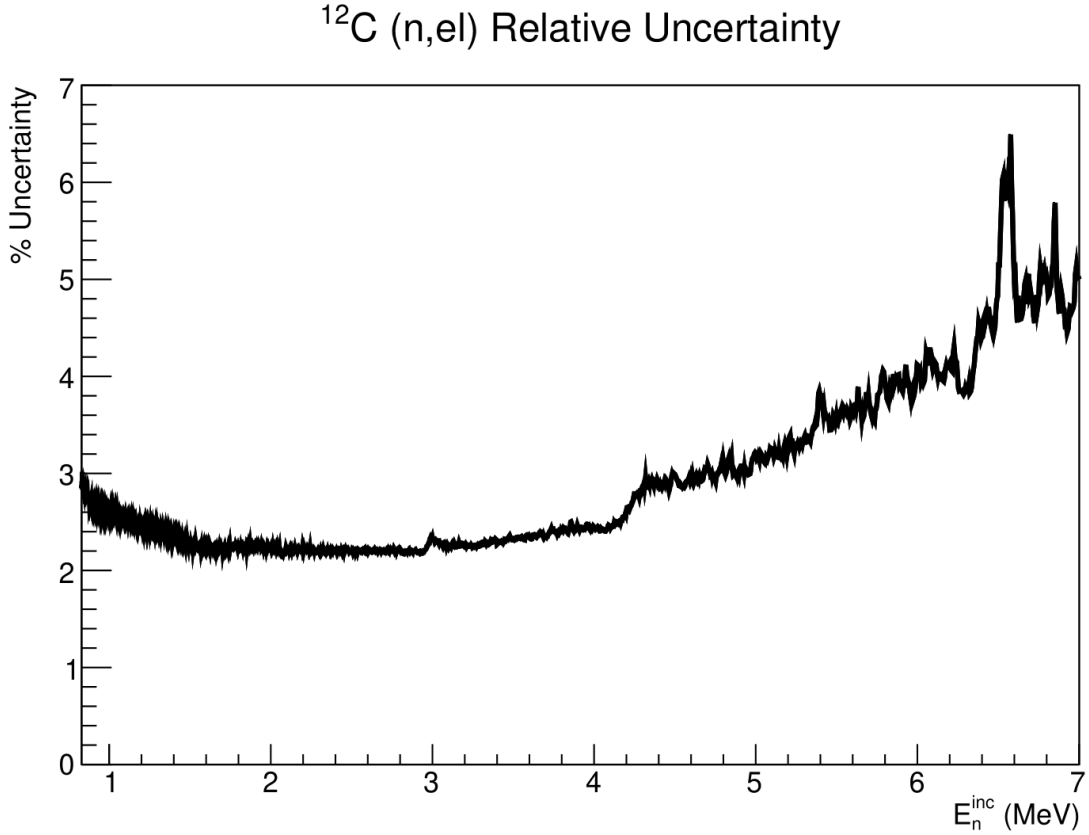

Figure 5.6 The relative uncertainty of the measured integrated cross section from Figure 5.5.

of this peak is found in Ref. [75] but is not seen in other available datasets. This peak is also not seen in the differential angular cross section data that are presented in Section 5.3, suggesting that it is not being suppressed when integrating over angles that are measured in this work. In contrast, the aforementioned peak is noticed in the inelastic cross section $(n,n'\gamma)$ using the CoGNAC setup for ^{12}C, as reported in Ref. [76], while ENDF-B/VIII.0 does not include this peak in the inelastic evaluation.

Looking at the relative uncertainty of the measured integrated cross section in Figure 5.6, the relative uncertainty increases with increasing energy and at low E_n^{inc} (0.85 – 1.8 MeV). The overall shape mimics a flip about the x axis of the efficiency of a liquid scintillator. This follows the trend with decreased measured counts at low energies and with increasing energy starting at $\approx$ 3 MeV. The measured relative uncertainty does not go lower than the relative uncertainty in the ^{235}U (n,f) cross section (1.27314%) nor the PFNS of ^{252}Cf

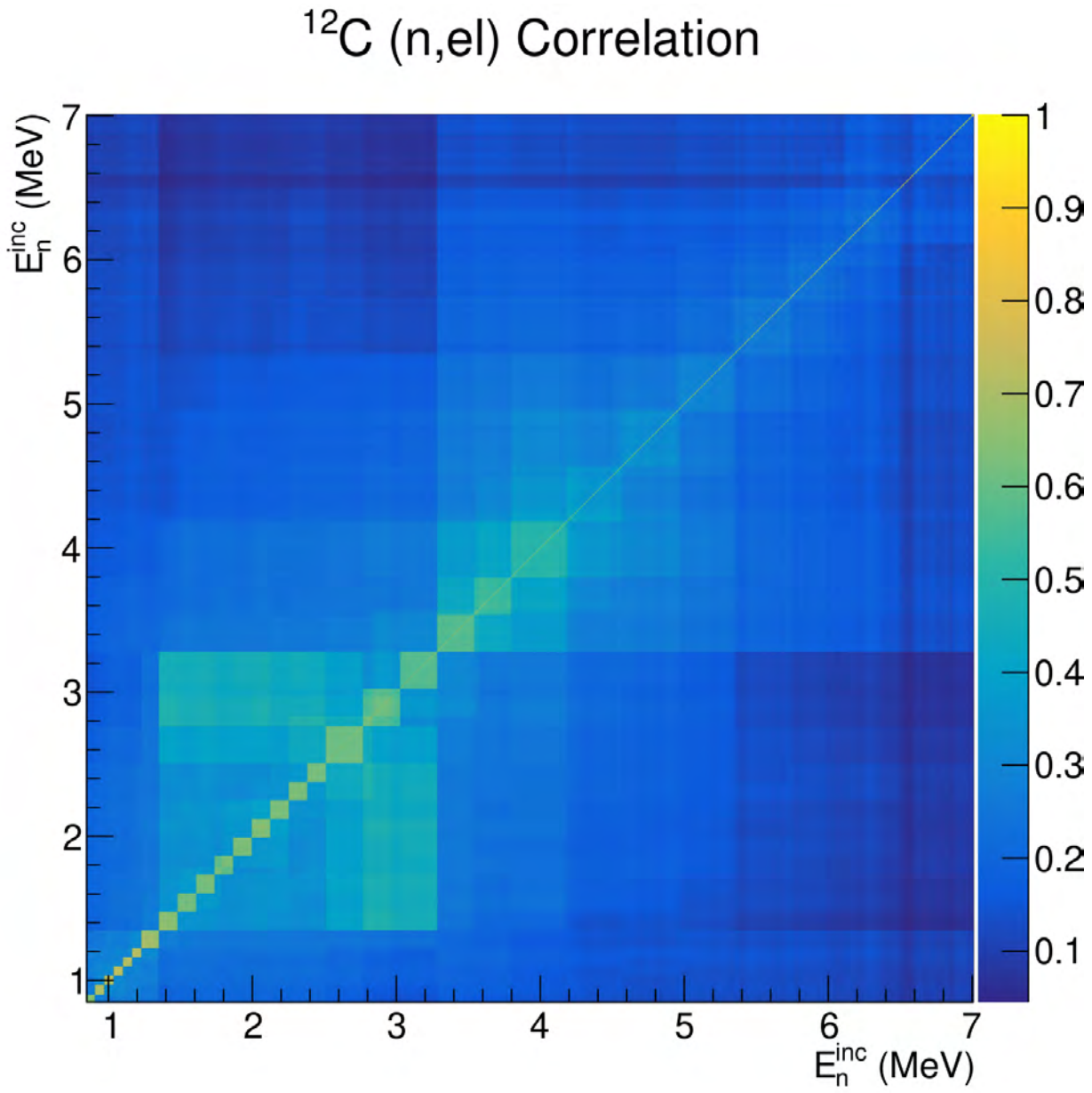

Figure 5.7 The correlation matrix of the measured integrated cross section from Figure 5.5.

(1.16586%) within the measured energy ranges as reported in ENDF-B/VIII.0 [71, 70], as these quantities were utilized directly in this analysis.

In the correlation matrix, Figure 5.7, the matrix is symmetric about the diagonal with the digonal values being equal to 1. Additionally, one can see the features of the ^{252}Cf PFNS correlation matrix (Figure 4.1), as the block structures along the diagonal and rectangles from the 2 – 3 MeV range, as well as those from the correlation matrix from the ^{235}U fission

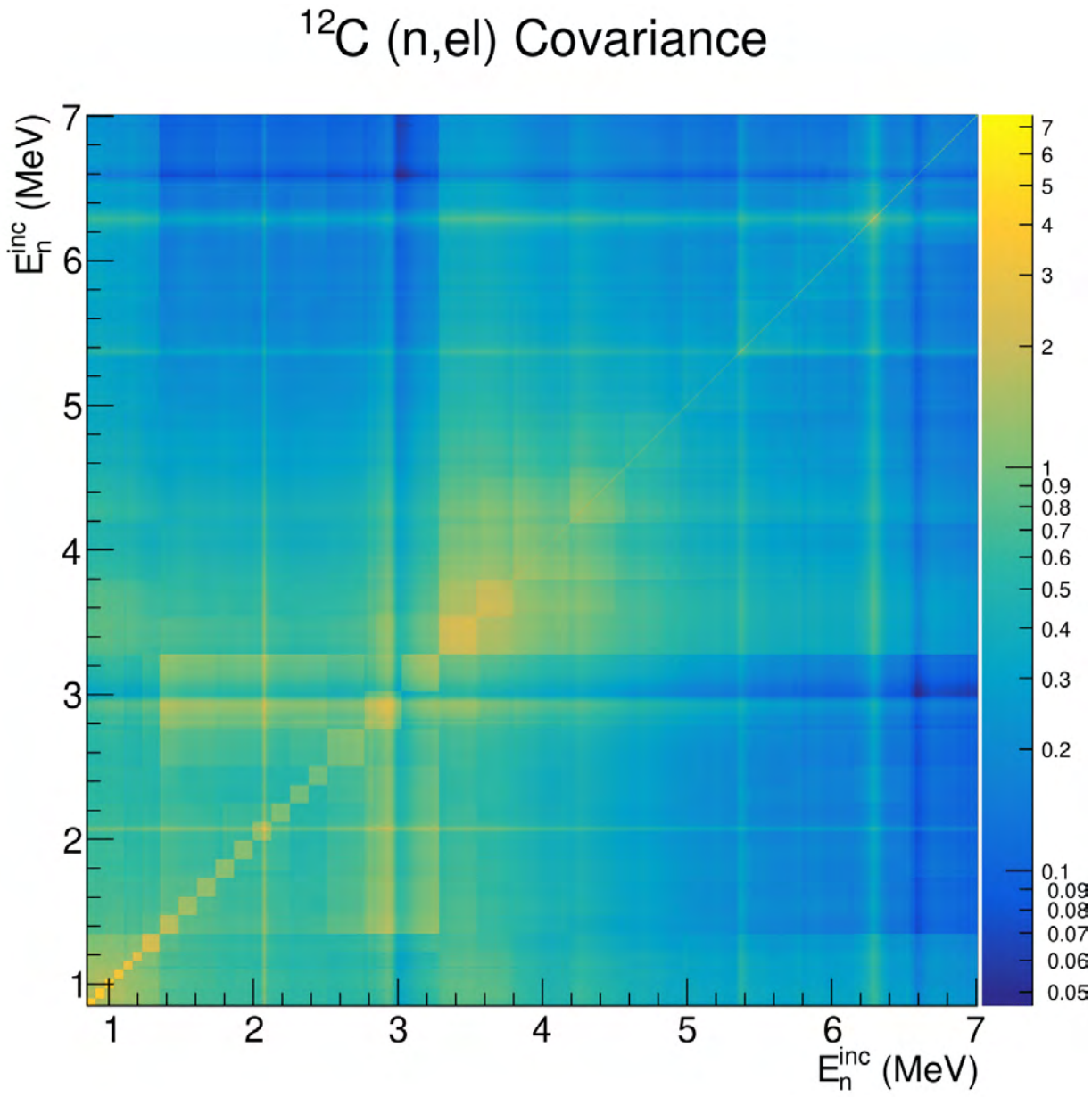

Figure 5.8 The covariance matrix of the measured integrated cross section from Figure 5.5.

cross section (Figure 4.2), as the block structures along the diagonal. This behavior comes from the fact that each detector shares a measured neutron flux that contains the information of the ^{235}U fission cross section and in the derivation of a detector efficiency measured relative to the PFNS of ^{252}Cf as described in Chapter 3.

Similar to the correlation matrix, the covariance matrix in Figure 5.8 is symmetric about the diagonal and the major features of the ^{252}Cf and ^{235}U correlation matrices (using the

process described in Chapter 4, Section 4.8 to covert between the correlation and covariance matrices) appear in the measured integrated cross section covariance matrix. The lines that run horizontally and vertically correspond to resonance structures within the measured cross section due to having higher absolute uncertainty but a lower relative uncertainty because of statistics. For example, the peaks in the measured integrated cross section close to 2.1 MeV, 3 MeV, 5.4 MeV, and 6.3 MeV appear as "bright" lines in the covariance matrix along with valleys in the measured integrated cross section near 3 MeV and 6.6 MeV.

5.3 Differential Angular Cross Section

The differential angular cross section $\frac{d\sigma}{d\Omega}$ can be measured at each of the 9 angles θ_d of the liquid scintillators. The corresponding differential angular cross sections are obtained by taking the average differential angular cross section across the detectors that share the same θ_d. The measured differential angular cross section is scaled to the value of the ENDF-B/VIII.0 differential angular cross section, that has CoGNAC liquid scintillator geometry and resolution applied, at 1.8 MeV for easy shape comparison. The scale factor for each of the differential angular cross section spectra is summarized in Table 5.1.

θ_d (°)	Scale Factor	Figure
150	0.00120035	5.9
135	0.001678793	5.10
120	0.00248327	5.11
105	0.00279897	5.12
90	0.0036084	5.13
75	0.00294293	5.14
60	0.00265083	5.15
45	0.192839	5.16
30	0.000817875	5.17

Table 5.1 The scale factor applied to each measured differential angular cross section based on the value of the ENDF-B/VIII.0 value at 1.8 MeV.

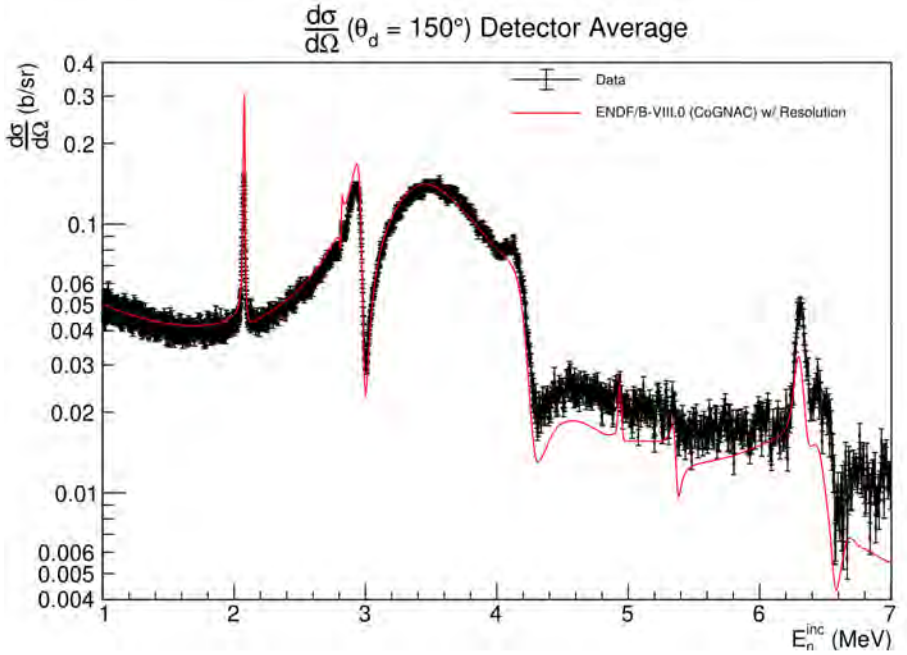

Figure 5.9 The measured differential angular cross section (black) for the averaged detectors at $\theta_d = 150°$ compared to the ENDF-B/VIII.0 differential angular cross section (red) with the liquid scintillator geometry and resolution applied.

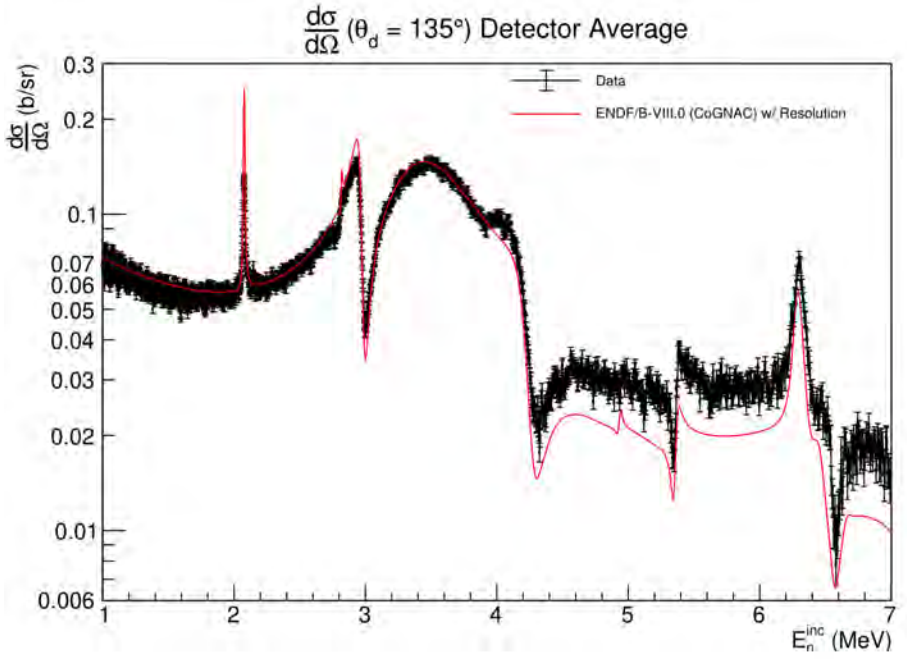

Figure 5.10 The measured differential angular cross section (black) for the averaged detectors at $\theta_d = 135°$ compared to the ENDF-B/VIII.0 differential angular cross section (red) with the liquid scintillator geometry and resolution applied.

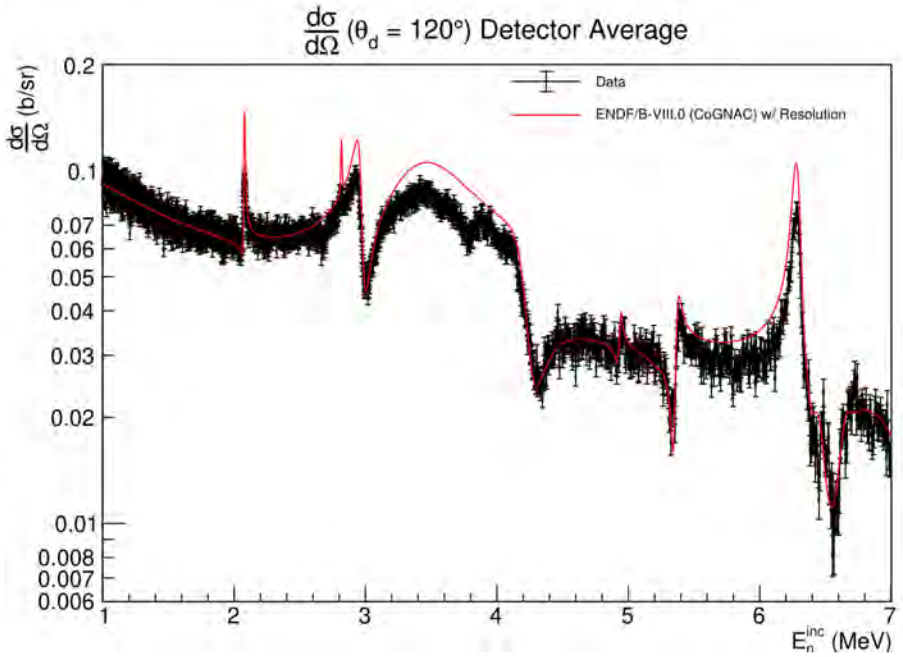

Figure 5.11 The measured differential angular cross section (black) for the averaged detectors at $\theta_d = 120°$ compared to the ENDF-B/VIII.0 differential angular cross section (red) with the liquid scintillator geometry and resolution applied.

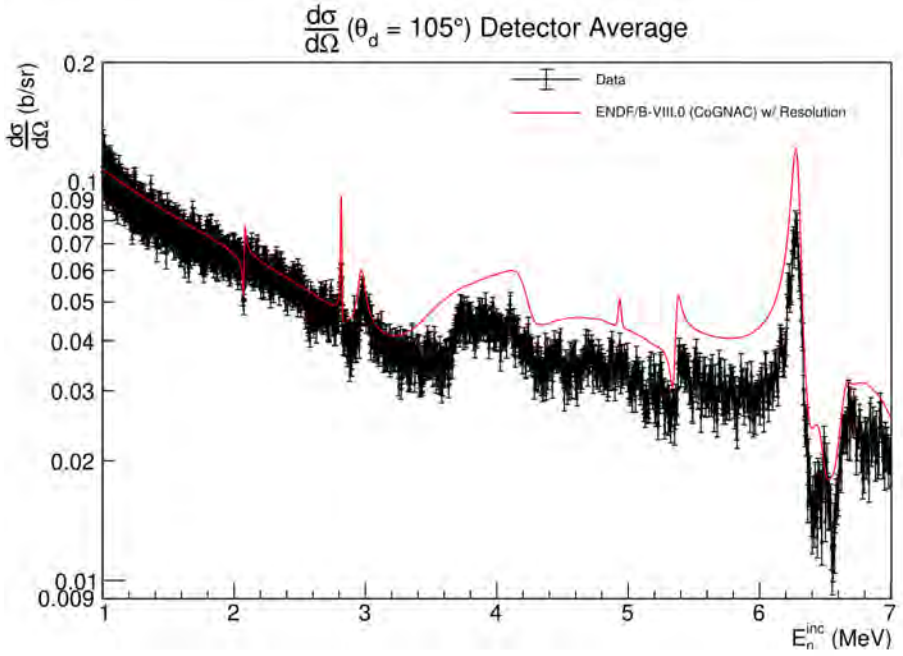

Figure 5.12 The measured differential angular cross section (black) for the averaged detectors at $\theta_d = 105°$ compared to the ENDF-B/VIII.0 differential angular cross section (red) with the liquid scintillator geometry and resolution applied.

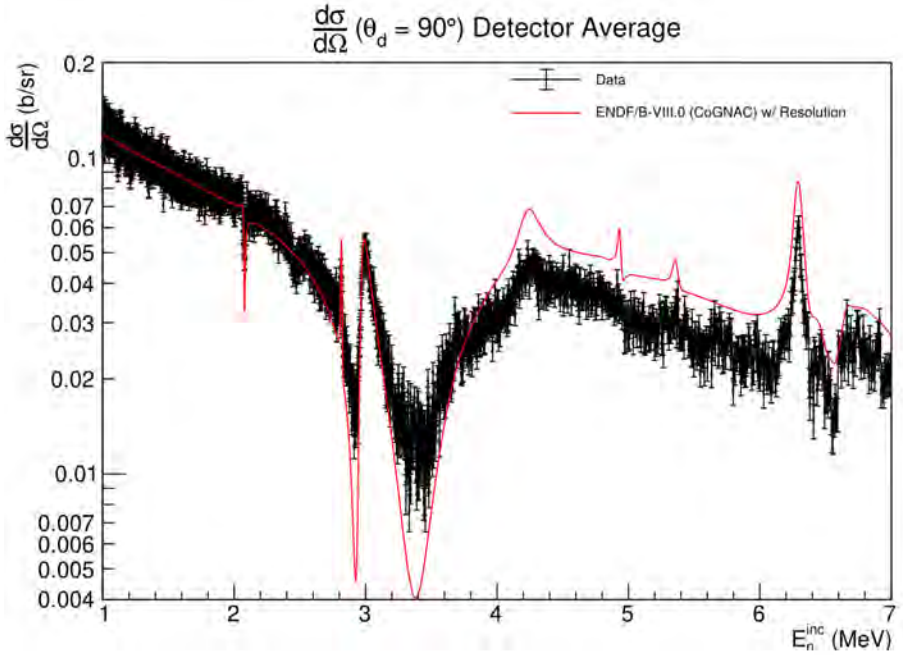

Figure 5.13 The measured differential angular cross section (black) for the averaged detectors at $\theta_d = 90°$ compared to the ENDF-B/VIII.0 differential angular cross section (red) with the liquid scintillator geometry and resolution applied.

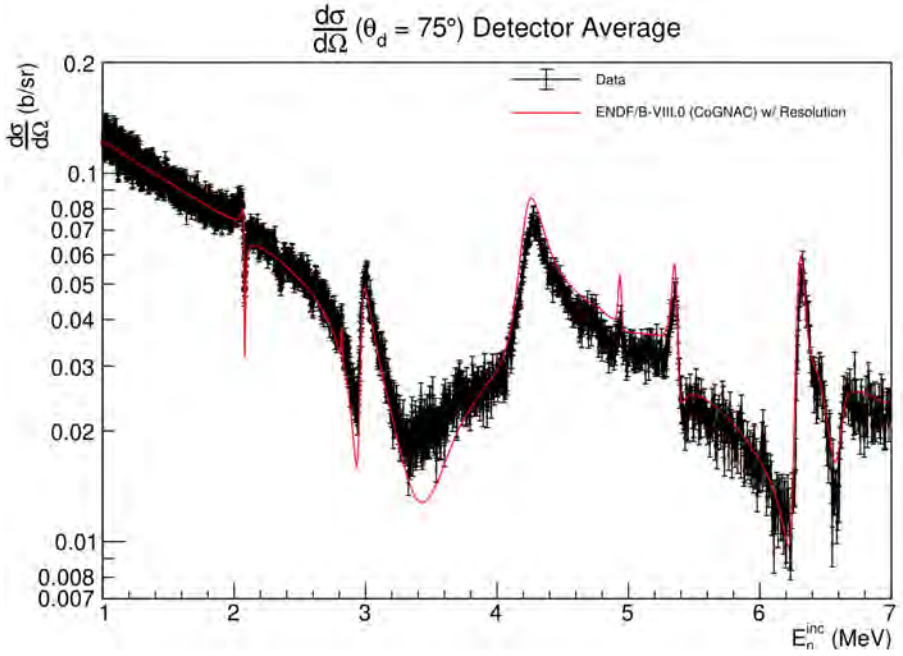

Figure 5.14 The measured differential angular cross section (black) for the averaged detectors at $\theta_d = 75°$ compared to the ENDF-B/VIII.0 differential angular cross section (red) with the liquid scintillator geometry and resolution applied.

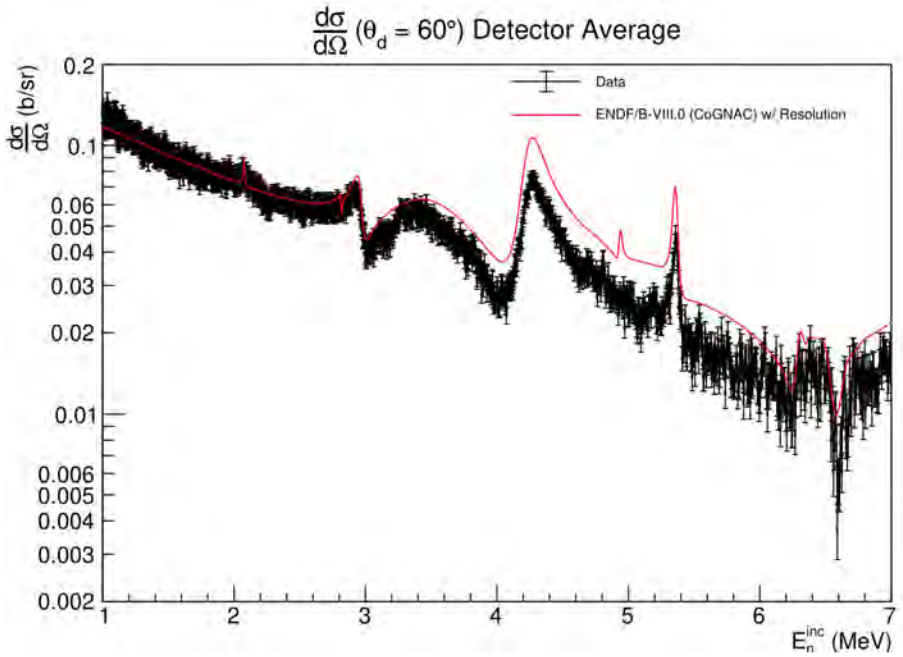

Figure 5.15 The measured differential angular cross section (black) for the averaged detectors at $\theta_d = 60°$ compared to the ENDF-B/VIII.0 differential angular cross section (red) with the liquid scintillator geometry and resolution applied.

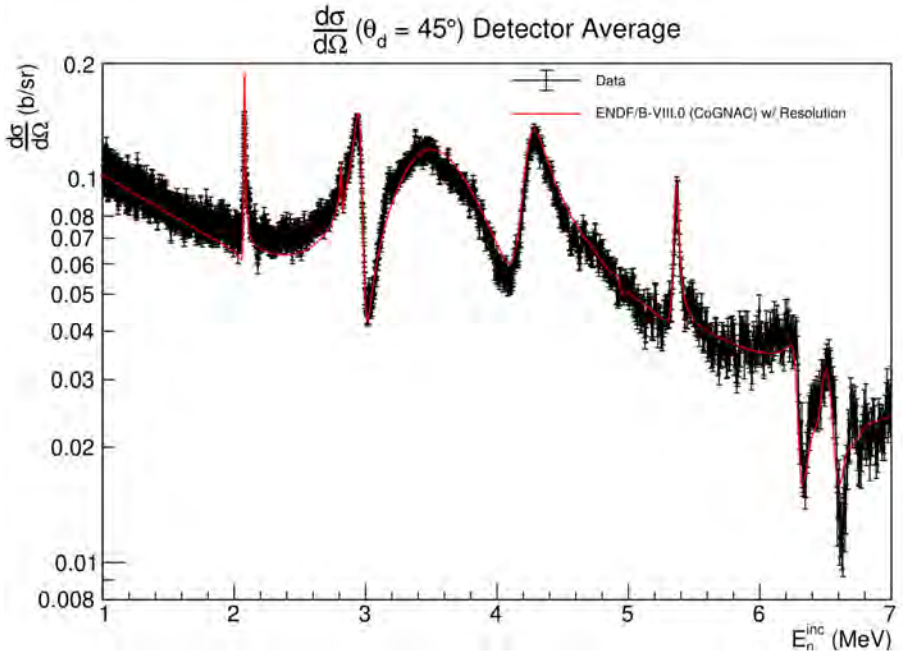

Figure 5.16 The measured differential angular cross section (black) for the averaged detectors at $\theta_d = 45°$ compared to the ENDF-B/VIII.0 differential angular cross section (red) with the liquid scintillator geometry and resolution applied.

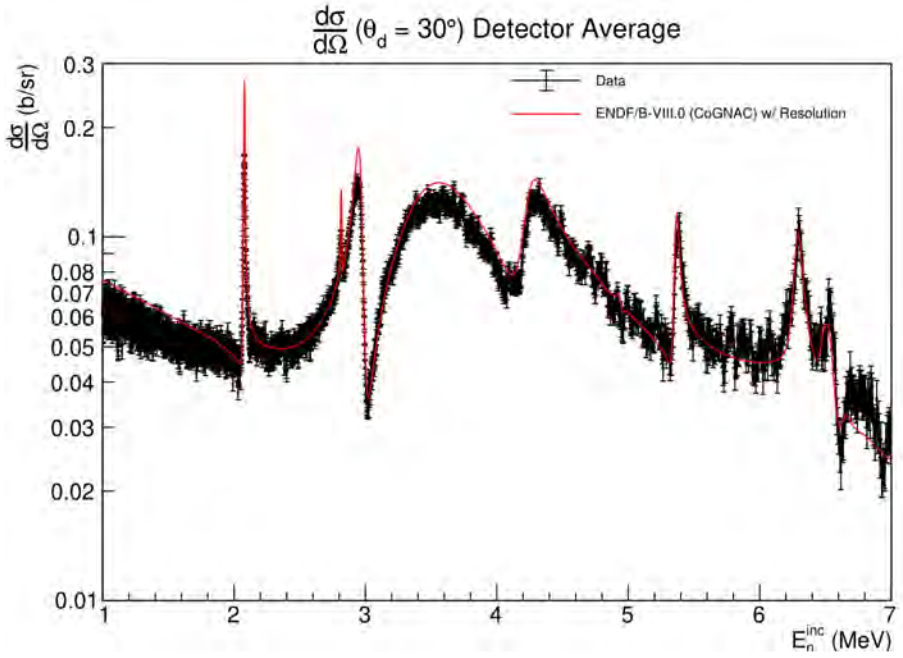

Figure 5.17 The measured differential angular cross section (black) for the averaged detectors at $\theta_d = 30°$ compared to the ENDF-B/VIII.0 differential angular cross section (red) with the liquid scintillator geometry and resolution applied.

Across all the measured θ_d, there is good shape agreement between the measured differential angular cross section and what is reported in the evaluation in the standard region (0.85 – 1.8 MeV). Similarly, there is good shape agreement up to 3 MeV and the overall trend of decreasing differential angular cross section values with increasing E_n^{inc} is consistent with the evaluation. Above 3 MeV, there is an amplitude difference between the measured differential angular cross section as shown in the evaluation. Detectors located at backward scattered angles, 150° and 135°, show higher values for the differential angular cross section than the evaluation whereas for other angles such as 105°, 90°, 75°, 60°, the measured differential angular cross section is lower than the evaluation. For detectors located at 120°, the measured differential angular cross section is lower than the evaluation in the range of 3 – 4 MeV and 5.5 – 6.3 MeV while agreeing in magnitude with the evaluation outside of this energy range. The two forward-scattered detectors located at 30° and 45° show the best agreement with the evaluation across the measured energy range. The respective contribution, as a percentage of the integrated cross section, is shown in Figure 5.18a for the

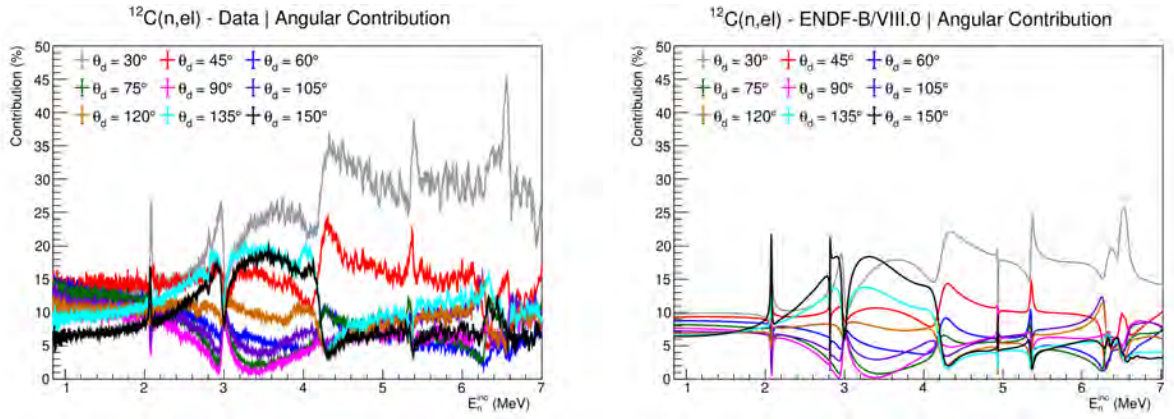

(a) **(b)**

Figure 5.18 The contribution of the differential angular cross section to the integrated cross section as a percentage. Figure 5.18a shows the contribution from the analyzed data while Figure 5.18b shows the contribution using the ENDF-B/VIII.0 evaluation.

measured data and for ENDF-B/VIII.0 in Figure 5.18b.

Looking at Figure 5.18, the two plots are made by taking the differential angular cross section as a percentage of the integrated cross section. As seen in both the measured data (Figure 5.18a) and in the evaluation (Figure 5.18b), the two forward angles of 30° and 45° are the two largest contributors to the integrated cross section. Additionally, the ordering of the contributions (from highest to lowest) is consistent between the two figures with only the two most backward scattered angles of 135° and 150° flipping in the $\approx 3-4$ MeV region.

5.4 Angular Distributions

Similar to the differential angular cross section data, it is possible to view the data as an angular distribution by keeping the E_n^{inc} value fixed and looking at the differential angular cross section as a function of the CM scattering angle $\tilde{\theta}_n$. The angular distributions are compared with the ENDF-B/VIII.0 angular distributions at reported E_n^{inc} values using Equation 5.1. For a given E_n^{inc}, as provided in Ref [73], at a given detection angle θ_d, the differential angular cross section is evaluated (via interpolation) at the reported E_n^{inc} of interest and is shown in Figures 5.19 – 5.21 . Additionally, to correct for the forward focusing effect from special relativity, as mentioned near the end of Chapter 1, Section 1.5, the data points have the solid angle scale factor given by Equation X (from the Roman numeral

equations from Chapter 1) applied for accurate comparison of the angular distributions of the data and evaluation. Each data point is also multiplied by the integration factor, given in Table 3.2 (Chapter 3), that accounts for the solid angle size of the liquid scintillator. The angular distribution made by the data points are then scaled to 90° of the ENDF-B/VIII.0 angular distribution for easier shape comparison of the data with the evaluation.

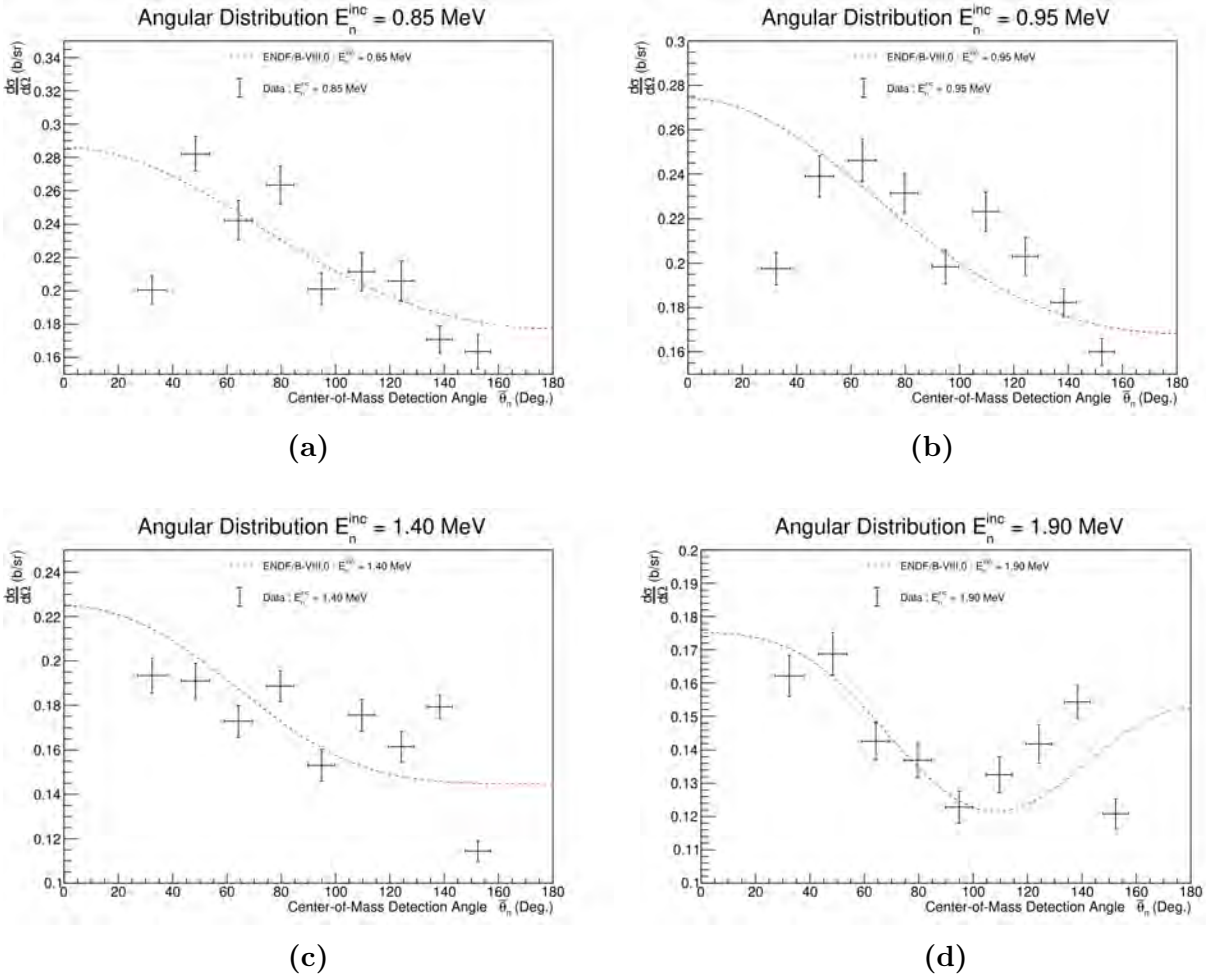

Figure 5.19 The measured CM angular distributions for E_n^{inc} values of 0.85 MeV (5.19a), 0.95 MeV (5.19b), 1.4 MeV (5.19c), and 1.9 MeV (5.19d) compared to the CM angular distributions from ENDF-B/VIII.0 (red dashed).

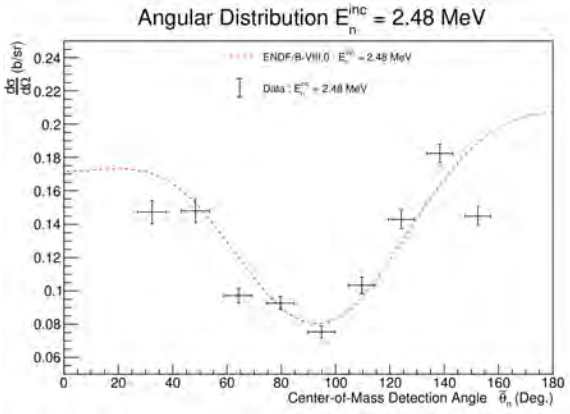

(a)

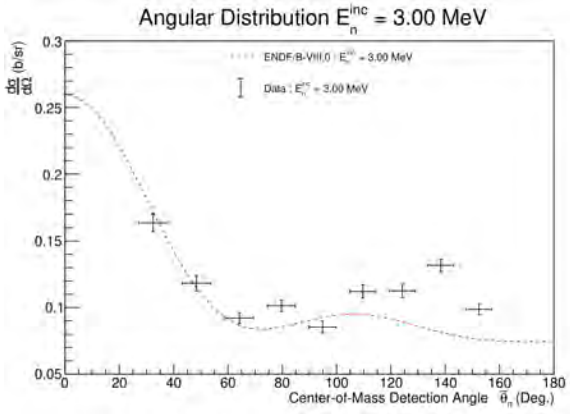

(b)

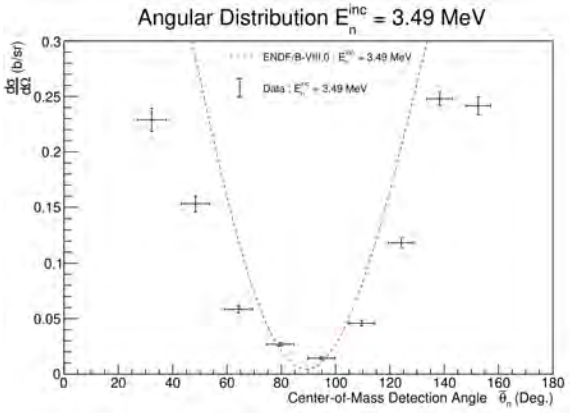

(c)

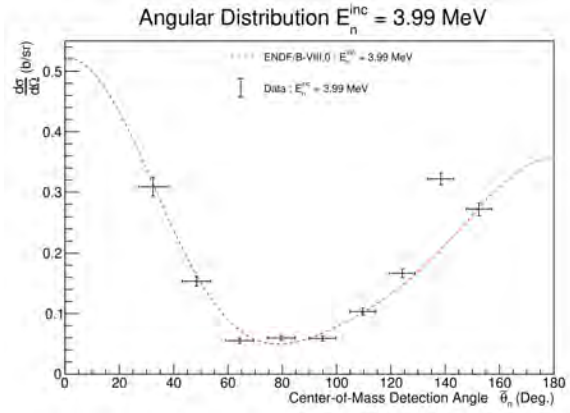

(d)

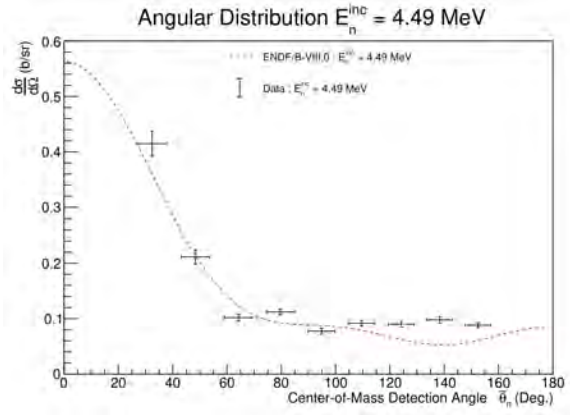

(e)

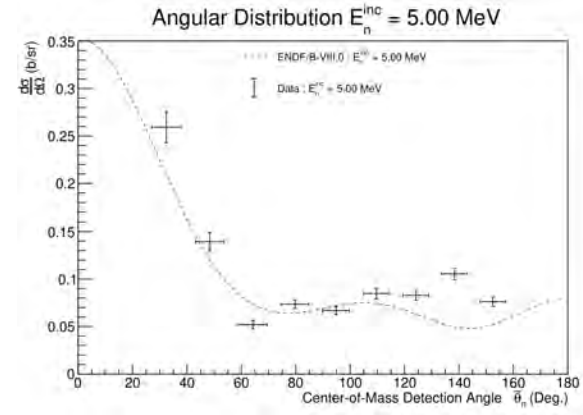

(f)

Figure 5.20 The measured CM angular distributions for E_n^{inc} values of 2.48 MeV (5.20a), 3 MeV (5.20b), 3.49 MeV (5.20c), 3.99 MeV (5.20d), 4.49 MeV (5.20e), and 5 MeV (5.20f) compared to the CM angular distributions from ENDF-B/VIII.0 (red dashed).

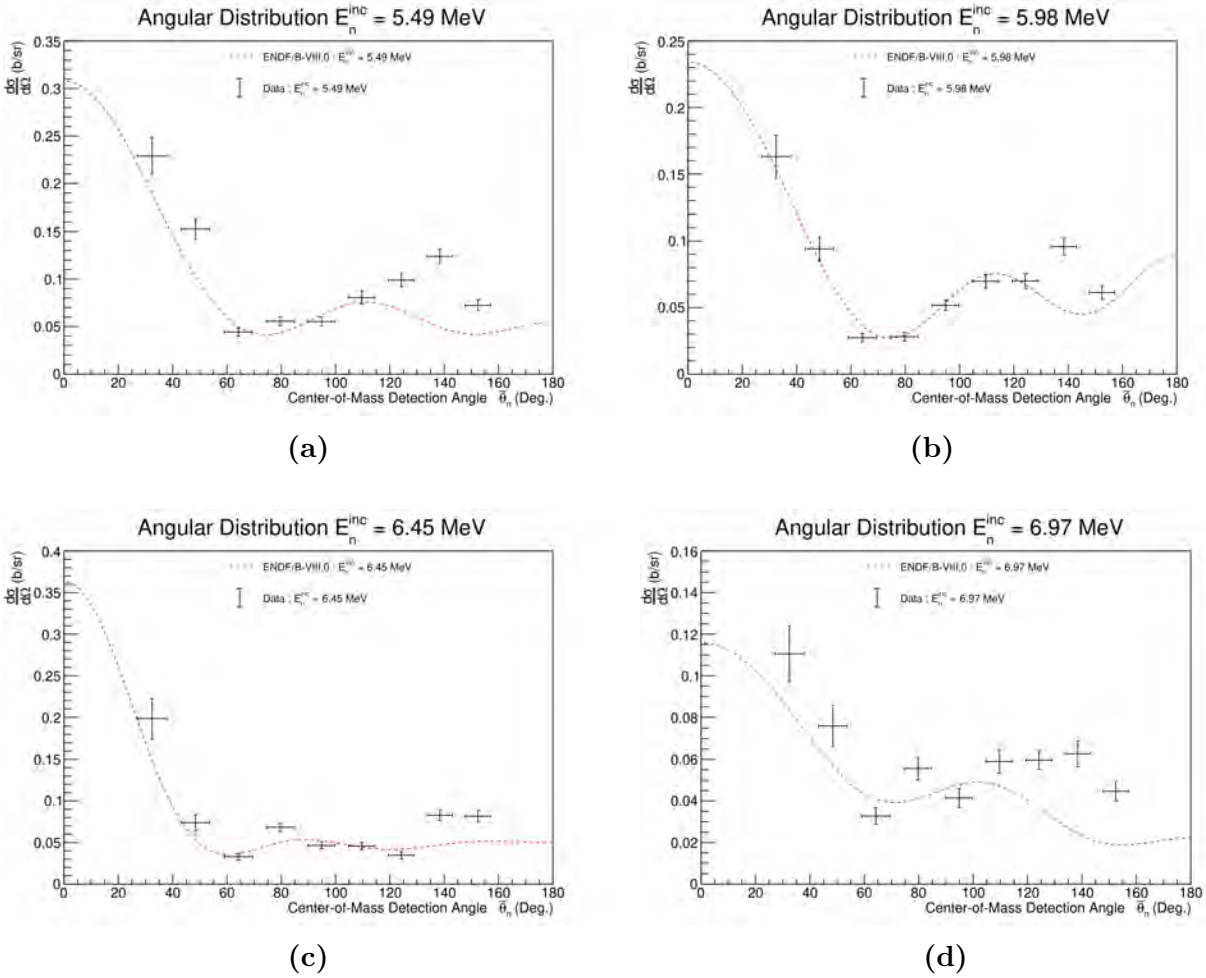

Figure 5.21 The measured CM angular distributions for E_n^{inc} values of 5.49 MeV (5.21a), 5.98 MeV (5.21b), 6.48 MeV (5.21c), and 6.97 MeV (5.21d) compared to the CM angular distributions from ENDF-B/VIII.0 (red dashed).

It can be seen from Figures 5.19, 5.20, and 5.21 that there is overall shape agreement between the measured and evaluated (ENDF-B/VIII.0) angular distributions in the energy ranges of 2.49 – 6.97 MeV (Figures 5.20 and 5.21). The best agreement occurs at 3.99 MeV (Figure 5.20d) minus the measured differential angular cross section for $\theta_d = 135°$. For lower E_n^{inc} values shown in Figure 5.19, the measured data oscillates more than the evaluation does with lower differential angular cross section values at forward scattered angles, before rising with increasing $\tilde{\theta}_n$ and decreasing again near $\theta_d = 90°$ before repeating the same behavior with increasing scattering angle. Figure 5.20a shows general agreement with lower measured differential angular cross section values at $\theta_d = 30°$ and $150°$. Similarly,

Figure 5.20c shows a widening of the angular distribution in comparison to the evaluation. For angular distributions that decrease with oscillatory behavior with increasing scattering angles (E_n^{inc} values of 3, 4.49 - 6.97 MeV in Figures 5.20b and 5.20e - 5.21d), there is shape agreement between the measured angular distribution and ENDF-B/VIII.0 with the exception of an increase in the differential angular cross section at $\theta_d = 135°$ that is consistent across the reported energy values and opposite of what is seen in the evaluation.

CHAPTER 6

CONCLUSIONS

The goal of this dissertation project was to measure the neutron elastic scattering cross section of ^{12}C. A measurement of the integrated cross section was accomplished along with analysis of the angular cross section information en route to producing the integrated cross section. Additionally, this measurement utilizes an established neutron data standard in the ^{252}Cf prompt fission neutron spectrum (PFNS).

Nuclear data impact not only experiments and simulations but also societal and applications of nuclear science. If the underlying data informing nuclear evaluations and simulations are incorrect and/or lacking, as is the case for scattering reactions on common nuclei such as carbon, this can have compounding uncertainties and inaccuracies. There is a lack of cross section data for the ^{12}C neutron elastic scattering cross section as shown in Figure 1.2, which is a common element found in structural, scientific, and biological systems.

The measurement made and presented in this dissertation takes advantage of the fact that the ^{252}Cf PFNS is a neutron data standard from 10 μeV to 30 MeV, which spans well beyond the limits of the emitted neutron energy range that is presented in this work. This makes the measured ^{12}C neutron elastic scattering cross section a reference measurement with respect to the ^{252}Cf PFNS.

This measurement utilized the CoGANC setup at the WNR Facility located at LANSCE where a range of neutron energies were simultaneously available, from the white neutron source, to measure the neutron elastic scattering cross section. The reported energy range for the incident neutron energy, E_n^{inc}, is 0.85 – 7 MeV which includes a portion of the carbon neutron elastic scattering cross section neutron data standard, ranging E_n^{inc} = 10 eV – 1.8 MeV, which serves as an anchor point for shape comparison of the measured cross section. Figure 5.5 there is shape agreement in the measured cross section and the ENDF-B/VIII.0 evaluation for ^{12}C neutron elastic scattering, with the evaluation having the geometry of the liquid scintillator coverage and resolution included.

Additionally, differential angular cross sections have been shown in comparison with their respective quantities from the ENDF-B/VIII.0 evaluation in Figures 5.9 through 5.17. The data are scaled to the standard region of the carbon standard for shape comparison and it can be seen that at lower incident neutron energies, that there is shape agreement with the evaluation. At higher energies, there are magnitude differences between the measured and evaluated differential angular cross section. This difference is not consistent across all detector angles as some have lower values than the evaluation while at other angles the values are higher than the evaluation; yet for the two most forward scattered angles, there is agreement with the evaluation across the range of measured incident neutron energies.

Angular distributions of the differential angular cross section are also shown across 14 incident neutron energies in Figures 5.19 through 5.21 where there are noticeable differences between the ENDF-B/VIII.0 evaluation and what has been measured in the data. For lower incident neutron energies, there is a noticeable difference in the shape behavior in comparison with the evaluation. With increasing incident neutron energy, there is better agreement between the measured angular distribution and the evaluation with respect to the shape across the reported scattering angles.

The measured integrated neutron elastic scattering cross section agrees well with the evaluation while showing shape differences when looking at the angular data. Such information is extremely valuable for evaluators when updating future versions of evaluations and for simulations and codes that rely on nuclear databases such as EXFOR. Given the demonstrated ability of the analysis techniques to produce a neutron elastic scattering cross section, along with detailed uncertainty quantification and covariances, it is desirable to apply such techniques to other stable nuclei that are also lacking in cross section data in the fast neutron region. Ongoing analysis is occurring for ^{28}Si and ^{16}O elastic scattering within the CoGNAC experimental program, with silicon [77] and oxygen [78] inelastic scattering results already published.

With respect to future developments and improvements, it is preferable to expand the

incident neutron energy range beyond the one studied in this work. While the lower energy value is limited by the arrival of the next micropulse, suppressing lower energy neutrons, expanding the measurement to higher incident neutron energies is possible. Two possible routes for increasing the measurement to higher incident neutron energies include further understanding the cause of the time shift as presented in Chapter 3, Section 3.8 and increasing the statistics of the ^{252}Cf PFNS measurement. For the former, more understanding into how the detectors behave at lower neutron energies versus high neutron energies is one avenue to explore that quantifies the liquid scintillator behavior beyond what has been done with respect to the derivation of an experiment-driven detector efficiency. Increasing the collection time for measuring the ^{252}Cf PFNS, or using a ^{252}Cf source with a higher activity, would allow more neutrons at higher emitted energies to be registered and collected, which is a current limitation with the measured ^{252}Cf PFNS.

These results are shared with the intention and hope of being of value to the nuclear data community and evaluators, but especially for users of nuclear data that rely upon accurate and well-characterized data. It is this effort of careful analysis and uncertainty quantification that can ultimately yield a more accurate and complete understanding of the nuclear landscape.

BIBLIOGRAPHY

[1] C. A. Bertulani, *et al. Introduction to nuclear reactions.* CRC Press, 2021.

[2] S. Pratt. *7.1 Definition of Cross Sections.* 2020. URL: https://web.pa.msu.edu/people/pratts/phy851/lectures/lectures_full.pdf.

[3] I. J. Thompson, *et al. Nuclear reactions for astrophysics: Principles, calculation and applications of low-energy reactions.* Cambridge University Press, 2009.

[4] P. L. Kapur, *et al.* "The dispersion formula for nuclear reactions". In: *Proceedings of the Royal Society of London. Series A. Mathematical and Physical Sciences* 166.925 (1938), pp. 277–295.

[5] E. P. Wigner, *et al.* "Higher angular momenta and long range interaction in resonance reactions". In: *Physical Review* 72.1 (1947), p. 29.

[6] A. M. Lane, *et al.* "R-Matrix Theory of Nuclear Reactions". In: *Rev. Mod. Phys.* 30 (2 1958), pp. 257–353. DOI: 10.1103/RevModPhys.30.257. URL: https://link.aps.org/doi/10.1103/RevModPhys.30.257.

[7] D. Baye, *et al.* "The R-matrix theory in nuclear and atomic physics". In: *Scholarpedia* 8.1 (2013). revision #129959, p. 12360. DOI: 10.4249/scholarpedia.12360.

[8] H. Sasaki, *et al. 12C+n evaluation work extending to 16 MeV neutron.*

[9] J. Humblet. "K-matrix analysis of resonance nuclear reactions". In: *Physical Review C* 42.4 (1990), p. 1582.

[10] J. R. Dunning, *et al.* "Interaction of Neutrons with Matter". In: *Phys. Rev.* 48 (3 1935), pp. 265–280. DOI: 10.1103/PhysRev.48.265. URL: https://link.aps.org/doi/10.1103/PhysRev.48.265.

[11] S. Agostinelli, *et al.* "Geant4—a simulation toolkit". In: *Nuclear Instruments and Methods in Physics Research Section A: Accelerators, Spectrometers, Detectors and Associated Equipment* 506.3 (2003), pp. 250–303. ISSN: 0168-9002. DOI: https://doi.org/10.1016/S0168-9002(03)01368-8. URL: https://www.sciencedirect.com/science/article/pii/S0168900203013688.

[12] US Department of Energy (USDOE). *A New Era of Discovery: The 2023 Long Range Plan for Nuclear Science.* Tech. rep. US Department of Energy (USDOE), Washington, DC (United States). Office of Science, Sept. 2023. DOI: 10.2172/2280968.

URL: https://www.osti.gov/biblio/2280968.

[13] D. A. Brown, *et al.*
"ENDF/B-VIII.0: The 8th Major Release of the Nuclear Reaction Data Library with CIELO-project Cross Sections, New Standards and Thermal Scattering Data". In: *Nuclear Data Sheets* 148 (2018). Special Issue on Nuclear Reaction Data, pp. 1–142. ISSN: 0090-3752. DOI: https://doi.org/10.1016/j.nds.2018.02.001. URL: https://www.sciencedirect.com/science/article/pii/S0090375218300206.

[14] Joint Evaluated Fission, *et al. JEFF-4.0 Evaluated Data: neutron data*. 2025. DOI: 10.82555/e9ajn-a3p20. URL: https://doi.org/10.82555/e9ajn-a3p20.

[15] O. Iwamoto, *et al.* "Japanese evaluated nuclear data library version 5: JENDL-5". In: *Journal of Nuclear Science and Technology* 60.1 (2023), pp. 1–60. DOI: 10.1080/00223131.2022.2141903. eprint: https://doi.org/10.1080/00223131.2022.2141903. URL: https://doi.org/10.1080/00223131.2022.2141903.

[16] Z. Ge, *et al.* "CENDL-3.2: The new version of Chinese general purpose evaluated nuclear data library". In: *EPJ Web Conf.* 239 (2020), p. 09001. DOI: 10.1051/epjconf/202023909001. URL: https://doi.org/10.1051/epjconf/202023909001.

[17] URL: https://www.nndc.bnl.gov/usndp/.

[18] URL: https://www.nndc.bnl.gov/.

[19] R. C. Runkle, *et al.* "Rattling nucleons: New developments in active interrogation of special nuclear material". In: *Nuclear Instruments and Methods in Physics Research Section A: Accelerators, Spectrometers, Detectors and Associated Equipment* 663.1 (2012), pp. 75–95. ISSN: 0168-9002. DOI: https://doi.org/10.1016/j.nima.2011.09.052. URL: https://www.sciencedirect.com/science/article/pii/S016890021101847X.

[20] B. D. Sowerby, *et al.*
"Recent advances in fast neutron radiography for cargo inspection". In: *Nuclear Instruments and Methods in Physics Research Section A: Accelerators, Spectrometers, Detectors and Associated Equipment* 580.1 (2007). Proceedings of the 10 th International Symposium on Radiation Physics, pp. 799–802. ISSN: 0168-9002. DOI: https://doi.org/10.1016/j.nima.2007.05.195. URL: https://www.sciencedirect.com/science/article/pii/S0168900207010868.

[21] P. A. Hausladen, *et al.* "Portable fast-neutron radiography with the nuclear materials identification system for fissile material transfers". In: *Nuclear Instruments and Methods in Physics Research Section B: Beam Interactions with Materials and Atoms*

261.1 (2007). The Application of Accelerators in Research and Industry, pp. 387–390. ISSN: 0168-583X. DOI: https://doi.org/10.1016/j.nimb.2007.04.206. URL: https://www.sciencedirect.com/science/article/pii/S0168583X07009147.

[22] A. Banu, *et al. MoNA – The first 25 years*. 2025. arXiv: 2502.14612 [nucl-ex]. URL: https://arxiv.org/abs/2502.14612.

[23] B. Luther, *et al.* "MoNA—The Modular Neutron Array". In: *Nuclear Instruments and Methods in Physics Research Section A: Accelerators, Spectrometers, Detectors and Associated Equipment* 505.1 (2003). Proceedings of the tenth Symposium on Radiation Measurements and Applications, pp. 33–35. ISSN: 0168-9002. DOI: https://doi.org/10.1016/S0168-9002(03)01014-3. URL: https://www.sciencedirect.com/science/article/pii/S0168900203010143.

[24] T. Baumann, *et al.* "Construction of a modular large-area neutron detector for the NSCL". in: *Nuclear Instruments and Methods in Physics Research Section A: Accelerators, Spectrometers, Detectors and Associated Equipment* 543.2 (2005), pp. 517–527. ISSN: 0168-9002. DOI: https://doi.org/10.1016/j.nima.2004.12.020. URL: https://www.sciencedirect.com/science/article/pii/S0168900205000379.

[25] W. F. Rogers, *et al.* "Measurements of fast neutron scattering in plastic scintillator with energies from 20 to 200 MeV". in: *Nuclear Instruments and Methods in Physics Research Section A: Accelerators, Spectrometers, Detectors and Associated Equipment* 943 (2019), p. 162436. ISSN: 0168-9002. DOI: https://doi.org/10.1016/j.nima.2019.162436. URL: https://www.sciencedirect.com/science/article/pii/S0168900219310010.

[26] Z. Kohley, *et al.* "Modeling interactions of intermediate-energy neutrons in a plastic scintillator array with Geant4". In: *Nuclear Instruments and Methods in Physics Research Section A: Accelerators, Spectrometers, Detectors and Associated Equipment* 682 (2012), pp. 59–65. ISSN: 0168-9002. DOI: https://doi.org/10.1016/j.nima.2012.04.060. URL: https://www.sciencedirect.com/science/article/pii/S0168900212004329.

[27] A. D. Carlson, *et al.* "Evaluation of the Neutron Data Standards". In: *Nuclear Data Sheets* 148 (2018). Special Issue on Nuclear Reaction Data, pp. 143–188. ISSN: 0090-3752. DOI: https://doi.org/10.1016/j.nds.2018.02.002. URL: https://www.sciencedirect.com/science/article/pii/S0090375218300218.

[28] A. D. Carlson. "The neutron cross section standards, evaluations and applications". In: *Metrologia* 48.6 (2011), S328. DOI: 10.1088/0026-1394/48/6/S09. URL: https://dx.doi.org/10.1088/0026-1394/48/6/S09.

[29] IAEA Neutron Data Standards 2017.

URL: https://www-nds.iaea.org/standards/.

[30] V. V. Zerkin, *et al.* "The experimental nuclear reaction data (EXFOR): Extended computer database and Web retrieval system".
In: *Nuclear Instruments and Methods in Physics Research Section A: Accelerators, Spectrometers, Detectors and Associated Equipment* 888 (2018), pp. 31–43.

[31] J. Meija, *et al.*
"Isotopic compositions of the elements 2013 (IUPAC Technical Report)".
In: *Pure and Applied Chemistry* 88.3 (2016), pp. 293–306.
DOI: doi:10.1515/pac-2015-0503.
URL: https://doi.org/10.1515/pac-2015-0503.

[32] R. M. White, *et al.*
"States in ^{12}B from Measurement and R-Matrix Analysis of $\sigma(\theta)$ for^{11}B(n,n)^{11}B".
in: *Nuclear Physics, Section A* 340 (1980), p. 13.
DOI: 10.1016/0375-9474(80)90320-6.
URL: http://dx.doi.org/10.1016/0375-9474(80)90320-6.

[33] J. D. Brandenberger, *et al.* "NEUTRON CROSS-SECTIONS AT 1.5 MEV".
in: *Bulletin of the American Physical Society*. Vol. 20. 9.
AMER INST PHYSICS CIRCULATION FULFILLMENT DIV, 500 SUNNYSIDE BLVD, WOODBURY ... 1975, pp. 1195–1195.

[34] Tech. rep. 73/2. INFN Reports / Low Energy Physics Series. 1973.

[35] P. Boschung, *et al.* "Scattering of Fast Neutrons by ^{12}C, ^{54}Fe, ^{56}Fe, ^{58}Ni, and^{60}Ni".
In: *Nuclear Physics, Section A* 161 (1971), p. 593.
DOI: 10.1016/0375-9474(71)90388-5.
URL: http://dx.doi.org/10.1016/0375-9474(71)90388-5.

[36] D. Lister, *et al.* "Elastic scattering of neutrons from carbon and oxygen in the energy range 3.0 to 4.7 MeV". in: *Physical Review* 143.3 (1966), p. 745.

[37] G. V. Gorlov, *et al.* "Elastic Scattering of Polarized Neutrons by Be 9, C 12 Co 59, Ni 62, Se 80, Nb 93, Cd 114, In 115, Sn 118, I 127, Pb, and Bi 209 Nuclei".
In: *Soviet Physics Doklady*. Vol. 9. 1965, p. 806.

[38] R. M. Wilenzick, *et al.* "Elastic and inelastic scattering of 6 MeV neutrons".
In: *Nuclear Physics* 62.3 (1965), pp. 511–525.

[39] M. Ageno, *et al.* "On The Scattering Of Fast Neutrons By Protons And Deuterons".
In: *Physical Review* 71 (1947), p. 20. DOI: 10.1103/PhysRev.71.20.
URL: http://dx.doi.org/10.1103/PhysRev.71.20.

[40] ENDF B/VIII.0 - G.M. Hale, P.G. Young, C.Y. Fu.
C-12(N,EL),SIG , MT=2, MF=3. Accessed 2025.

[41] BIPM, *et al. Evaluation of measurement data — Guide to the expression of uncertainty in measurement*.
Joint Committee for Guides in Metrology, JCGM 100:2008. 2008.
DOI: https://doi.org/10.59161/JCGM100-2008E.
URL: https://www.bipm.org/en/committees/jc/jcgm/publications/.

[42] BIPM, *et al. Evaluation of measurement data — Supplement 1 to the "Guide to the expression of uncertainty in measurement" — Propagation of distributions using a Monte Carlo method*. Joint Committee for Guides in Metrology, JCGM 101:2008. 2008. DOI: https://doi.org/10.59161/JCGM101-2008.
URL: https://www.bipm.org/en/committees/jc/jcgm/publications/.

[43] BIPM, *et al.*
Evaluation of measurement data — Supplement 2 to the "Guide to the expression of uncertainty in measurement" — Extension to any number of output quantities.
Joint Committee for Guides in Metrology, JCGM 102:2011. 2011.
DOI: https://doi.org/10.59161/jcgm102-2011.
URL: https://www.bipm.org/en/committees/jc/jcgm/publications/.

[44] V. Ramnath. "Determining the covariance matrix for a nonlinear implicit multivariate measurement equation uncertainty analysis".
In: *Int. J. Metrol. Qual. Eng.* 13 (2022), p. 9. DOI: 10.1051/ijmqe/2022008.
URL: https://doi.org/10.1051/ijmqe/2022008.

[45] Operated by Los Alamos National Security Los Alamos National Laboratory.
Neutron and proton science at LANSCE. URL: https://lansce.lanl.gov/.

[46] Los Alamos National Laboratory. *Los Alamos National Laboratory*.
URL: https://www.lanl.gov/.

[47] P. W. Lisowski, *et al.* "The Los Alamos Neutron Science Center".
In: *Nuclear Instruments and Methods in Physics Research Section A: Accelerators, Spectrometers, Detectors and Associated Equipment* 562.2 (2006). Proceedings of the 7th International Conference on Accelerator Applications, pp. 910–914.
ISSN: 0168-9002. DOI: https://doi.org/10.1016/j.nima.2006.02.178. URL: https://www.sciencedirect.com/science/article/pii/S0168900206003792.

[48] S. F. Nowicki, *et al.*
"The Los Alamos Neutron Science Center Spallation Neutron Sources".
In: *Physics Procedia* 90 (2017). Conference on the Application of Accelerators in Research and Industry, CAARI 2016, 30 October – 4 November 2016, Ft. Worth, TX, USA, pp. 374–380. ISSN: 1875-3892.

DOI: https://doi.org/10.1016/j.phpro.2017.09.035. URL:
https://www.sciencedirect.com/science/article/pii/S1875389217301943.

[49] K. J. Kelly, *et al.* "The Neutron Scattering Cross Section and Angular Distribution Measurement Program at LANL". in: *EPJ Web of Conf.* 284 (2023), p. 01004.
DOI: 10.1051/epjconf/202328401004.
URL: https://doi.org/10.1051/epjconf/202328401004.

[50] P. W. Lisowski, *et al.*
"The Los Alamos National Laboratory Spallation Neutron Sources".
In: *Nuclear Science and Engineering* 106.2 (1990), pp. 208–218.
DOI: 10.13182/NSE90-A27471. eprint: https://doi.org/10.13182/NSE90-A27471.
URL: https://doi.org/10.13182/NSE90-A27471.

[51] Operated by Los Alamos National Security Los Alamos National Laboratory.
Weapons neutron research flight paths.
URL: https://lansce.lanl.gov/facilities/wnr/flight-paths/index.php.

[52] Eljen Technology. *Neutron/Gamma PSD.* URL: https:
//eljentechnology.com/products/liquid-scintillators/ej-301-ej-309.

[53] C. M. Combes, *et al.* "Optical and scintillation properties of pure and Ce3+-doped Cs2LiYCl6 and Li3YCl6:Ce3+ crystals".
In: *Journal of Luminescence* 82.4 (1999), pp. 299–305. ISSN: 0022-2313.
DOI: https://doi.org/10.1016/S0022-2313(99)00047-2. URL:
https://www.sciencedirect.com/science/article/pii/S0022231399000472.

[54] Hamamatsu Photonics. *Hamamatsu Photonics.* URL: http://www.hamamatsu.com/.

[55] CAEN. *SY4527.* 2025. URL: https://www.caen.it/products/sy4527/.

[56] CAEN. *V1730 / V1730s.* 2025. URL: https://www.caen.it/products/v1730/.

[57] Midas. 2023. URL: https://daq00.triumf.ca/MidasWiki/index.php/Main_Page.

[58] R. Brun, *et al. root-project/root: v6.32/06.* Version v6-32-06. Sept. 2024.
URL: https://root.cern/releases/release-63206/#git.

[59] H. Schölermann, *et al.*
"Optimizing the energy resolution of scintillation counters at high energies".
In: *Nuclear Instruments and Methods* 169.1 (1980), pp. 25–31. ISSN: 0029-554X.
DOI: https://doi.org/10.1016/0029-554X(80)90097-X. URL:
https://www.sciencedirect.com/science/article/pii/0029554X8090097X.

[60] A. Enqvist, *et al.* "Neutron light output response and resolution functions in EJ-309

liquid scintillation detectors".
In: *Nuclear Instruments and Methods in Physics Research Section A: Accelerators, Spectrometers, Detectors and Associated Equipment* 715 (2013), pp. 79–86.
ISSN: 0168-9002. DOI: https://doi.org/10.1016/j.nima.2013.03.032. URL: https://www.sciencedirect.com/science/article/pii/S0168900213003203.

[61] H. Wang, *et al.* "Neutron light output function and resolution investigation of the deuterated organic liquid scintillator EJ-315".
In: *Radiation Measurements* 89 (2016), pp. 99–106. ISSN: 1350-4487.
DOI: https://doi.org/10.1016/j.radmeas.2016.03.009. URL: https://www.sciencedirect.com/science/article/pii/S1350448716300798.

[62] R. Brun. *TH2.cxx*. 2024.
URL: https://root.cern.ch/doc/v632/TH2_8cxx_source.html.

[63] IAEA Neutron Data Standards.
252Cf(sf) PFNS from the IRDFF-II library W. Mannhart 1987-1989. 2017.
URL: https://nds.iaea.org/standards/ref-spectra/PFNS-Cf252sf.txt.

[64] W. Mannhart.
"Evaluation of the Cf-252 fission neutron spectrum between 0 MeV and 20 MeV".
in: *Properties of Neutron Sources* (1987), pp. 158–171.

[65] W. Mannhart. *Status of the Cf-252 fission neutron spectrum evaluation with regard to recent experiments*. Tech. rep. 1989.

[66] A. Trkov, *et al.*
"Evaluation of the neutron induced reactions on 235U from 2.25 keV up to 30 MeV".
in: *EPJ Web Conf.* 146 (2017). DOI: 10.1051/epjconf/201714602029.
URL: https://doi.org/10.1051/epjconf/201714602029.

[67] R. Capote, *et al.* "IAEA CIELO Evaluation of Neutron-induced Reactions on 235U and 238U Targets". In: *Nuclear Data Sheets* 148 (2018). Special Issue on Nuclear Reaction Data, pp. 254–292. ISSN: 0090-3752.
DOI: https://doi.org/10.1016/j.nds.2018.02.005. URL: https://www.sciencedirect.com/science/article/pii/S0090375218300243.

[68] J. A. Kulesza, *et al. MCNP® Code Version 6.3.0 Theory & User Manual*.
Tech. rep. LA-UR-22-30006, Rev. 1.
Los Alamos, NM, USA: Los Alamos National Laboratory, 2022.
DOI: 10.2172/1889957. URL: https://www.osti.gov/biblio/1889957.

[69] M. E. Rising, *et al. MCNP® Code Version 6.3.0 Release Notes*.
Tech. rep. LA-UR-22-33103, Rev. 1.
Los Alamos, NM, USA: Los Alamos National Laboratory, 2023.

DOI: 10.2172/1909545. URL: https://www.osti.gov/biblio/1909545.

[70] ENDF B/VIII.0 - C.W.Reich, W. Mannhart, T. Englad.
CF-252(STD,F),COV/DE , MT=18, MF=35. Accessed 2025.

[71] ENDF B/VIII.0 - IAEA CIELO Collaboration.
U-235(STD,F),COV/DE , MT=18, MF=33. Accessed 2025.

[72] ENDF B/VIII.0 - IAEA CIELO Collaboration.
U-235(STD,F),COV/DE , MT=18, MF=3. Accessed 2025.

[73] ENDF B/VIII.0 - G.M. Hale, P.G. Young, C.Y. Fu.
C-12(N,EL),DA , MT=2, MF=4. Accessed 2025.

[74] D. Brown. In: *ENDF-6 formats manual - data formats and procedures for the evaluated nuclear data files ENDF/B-VI, ENDF/B-VII and ENDF/B-VIII* (2023).
DOI: 10.2172/2007538. URL: https://www.osti.gov/biblio/2007538.

[75] S. Cierjacks, *et al.* "High precision time-of-flight measurements of neutron resonance energies in carbon and oxygen between 3 and 30 MeV".
in: *Nuclear Instruments and Methods* 169.1 (1980), pp. 185–198.

[76] K. J. Kelly, *et al.*
"Measurement of the cross section of the $Q = 4.4398$ MeV $^{12}\mathrm{C}(n, n'\gamma)$ reaction from threshold to 16.5 MeV using γ and correlated $n-\gamma$ detection".
In: *Phys. Rev. C* 108 (1 2023), p. 014603. DOI: 10.1103/PhysRevC.108.014603.
URL: https://link.aps.org/doi/10.1103/PhysRevC.108.014603.

[77] K. J. Kelly, *et al.* "Measurement of the $^{28}\mathrm{Si}(n,n'\gamma)$ cross section with n, γ, and correlated n-γ angular distributions". In: *Phys. Rev. C* (2025).
DOI: 10.1103/q8rv-2m1v. URL: https://link.aps.org/doi/10.1103/q8rv-2m1v.

[78] K. J. Kelly, *et al.* "High-precision Measurement of the 16O(n,n'γ) Cross Section using γ-ray Detection in Liquid Scintillators with H2O and BeO Targets".
In: *Nuclear Data Sheets* 202 (2025), pp. 1–11. ISSN: 0090-3752.
DOI: https://doi.org/10.1016/j.nds.2025.04.001. URL:
https://www.sciencedirect.com/science/article/pii/S0090375225000341.